PARTITION DENSITY FUNCTIONAL THEORY FOR SEMI-INFINITE AND PERIODIC SYSTEMS

A Dissertation

Submitted to the Faculty

of

Purdue University

by

Kelsie Niffenegger

In Partial Fulfillment of the

Requirements for the Degree

of

Doctor of Philosophy

December 2018

Purdue University

West Lafayette, Indiana

THE PURDUE UNIVERSITY GRADUATE SCHOOL
STATEMENT OF DISSERTATION APPROVAL

Dr. Adam Wasserman, Chair

Department of Chemistry

Dr. Francis Robicheaux

Department of Physics and Astronomy

Dr. Sherwin Love

Department of Physics and Astronomy

Dr. Daniel Elliott

School of Electrical and Computer Engineering

Approved by:

Dr. John Finley

Head of the Departmental Graduate Program

ACKNOWLEDGMENTS

I would like to thank the past and present members of the Suspenders who I have been able to work with the past few years. I am especially grateful for invaluable help I received from Jonathan Nafziger, Adam Kline, Daniel Jensen, Yanal Oueis, and of course Adam Wasserman.

I also want to thank my friends for all of their encouragement, the great memories, and everything they have done for me throughout the years. I wouldn't have managed grad school without them. My cat, Arya, has also been a constant source of comfort and I am thankful for her patience dealing with my grad school experience.

Finally, I am forever thankful to my parents, brothers, and extended family for all of their love and support.

TABLE OF CONTENTS

Page

LIST OF FIGURES

Figure Page

Figure Page

Figure Page

Figure Page

Figure Page

Figure Page

Figure Page

ABBREVIATIONS

DFT	Density Functional Theory
KS	Kohn-Sham
HK	Hohenberg-Kohn
KS-DFT	Kohn-Sham Density Functional Theory
PPLB	Perdew, Parr, Levy, and Balduz
HOMO	Highest Occupied Molecular Orbital
LUMO	Lowest Unoccupied Molecular Orbital
P-DFT	Partition Density Functional Theory
DFA	Density Functional Approximation
XC	Exchange-Correlation
FDE	Frozen-Density Embedding

ABSTRACT

Niffenegger, Kelsie PhD, Purdue University, December 2018. Partition Density Functional Theory for Semi-Infinite and Periodic Systems. Major Professor: Adam Wasserman.

Partition Density Functional Theory (P-DFT) is a formally exact method to find the ground-state energy and density of molecules via self-consistent calculations on isolated fragments. It is being used to improve the accuracy of Kohn-Sham DFT (KS-DFT) calculations and to lower their computational cost. Here, the method has been extended to be applicable to semi-infinite and periodic systems. This extension involves the development of new algorithms to calculate the *exact* partition potential, a central quantity of P-DFT. A novel feature of these algorithms is that they are applicable to systems of constant chemical potential, and not only to systems of constant electron number. We illustrate our method on one-dimensional model systems designed to mimic metal-atom interfaces and atomic chains. From extensive numerical tests on these model systems, we infer that: 1.) The usual derivative discontinuities of open-system KS-DFT are reduced (but do not disappear completely) when an atom is at a *finite* distance from a metallic reservoir; 2.) In situations where we do not have chemical potential equalization between fragments of a system, a new constraint for P-DFT emerges which relates the fragment chemical potentials and the combined system chemical potential; 3.) P-DFT is an ideal method for studying charge transfer and fragment interactions due to the correct ensemble treatment of fractional electron charges; 4.) Key features of the partition potential at the metal-atom interface are correlated to well-known features of the underlying KS potential; and 5.) When there is chemical potential equalization between an atom and a metal surface it is interacting with, there is strong charge transfer between the metal and atom. In these cases of charge transfer the density response to an infinitesimal change

in the chemical potential is located almost exclusively around the atom. On the other hand, when the fragment chemical potentials do not equalize, the density response only affects the surface Friedel oscillations in the metal.

1. INTRODUCTION

Fifty years after its introduction, the Kohn-Sham (KS) formalism [1] of density functional theory (DFT) [2] has become the most widely used electronic structure method in computational chemistry. Its current applications span through the fields of biology, chemistry, and physics with over 80 software packages available which utilize DFT. The use of DFT has grown almost exponentially since its inception, with nearly 70,000 DFT papers being published in 2017 alone. This monumentous theory earned Walter Kohn, shared with John Pople, the 1998 Nobel Prize in chemistry [3]. As formulated DFT and KS-DFT are exact, but utilizing them for practical calculations requires approximations to the energy functionals. Many of these approximations work well for various systems and types of electron dynamics, however there are still many areas where these approximations fall short. For example: in systems where charge is transferred or shared between the constituents, modern approximations to the energy functionals often fail to accurately reproduce the ground state properties [4]. This is one of many shortcomings that people are trying to overcome in modern approximate DFT calculations.

Partition density functional theory (P-DFT) provides the framework to solve many of these ongoing issues, improve upon the results obtained using approximations in DFT, and potentially reduce computational cost. P-DFT, like DFT, is an exact theory, but to utilize it effectively approximations will be used. In order to create accurate approximations for the density functionals we begin by studying the exact results for simple systems. Work on approximations for P-DFT has been successfully done and implemented for diatomic molecules [5]. These finite systems are defined by their total electron number and exact results could be found through inversions using P-DFT as originally written.

Until now, P-DFT calculations had never been done on infinite or semi-infinite systems, which use the chemical potential instead of the number of electrons to characterize the system. P-DFT uses constraints based on the electron number and thus could not be directly used for these systems. Here we develop new inversion methods which extend the range of P-DFT to include those systems characterized by their chemical potential. Physical examples of these infinite and semi-infinite systems include molecular crystals, atomic chains, and interactions at metal or semiconductor surfaces.

Note: Hartree atomic units are used throughout this work, where $m_e = e = \hbar = 1$. Thus all distances are in bohr (1 a_0 = 0.529 Å) and energies in hartree (1 Ha = 27.2 eV). We use nonrelativistic Schrödinger equations within the Born-Oppenheimer approximation for all material presented.

2. DENSITY FUNCTIONAL THEORY

The first "density-functional" theory was Thomas-Fermi (TF) theory [6, 7] developed in 1926. TF theory did not reference the Schrödinger equation, instead relying solely on the electronic density. TF theory approximates the kinetic energy as that of a uniform electron gas and electron-electron interactions as classical Coulomb repulsion. While this is not an exact method, the idea of ridding oneself of the many-body wavefunction in favor of the electron density is very tantalizing. As systems of interest become larger and more complex, this becomes an enormously powerful computational tool. Instead of calculating and storing a wavefunction that scales exponentially with the number of electrons in the system, one may use the electronic density which always remains a function of one variable (or 3 coordinates).

The story of modern DFT didn't begin until 1964, with the two Hohenberg-Kohn (HK) theorems [2]:

1. There is a unique one-to-one mapping between the ground state density of a system and the external potential of that system (and therefore, its Hamiltonian) up to a constant.

2. The density that minimizes the total energy is the exact ground state density.

This means that a system can be uniquely described by the ground state density with no need for the full many-body wavefunction and could be found through a minimization of the energy as a functional of the density. The energy and other observables may now be written as functionals of the ground state density. Functionals map a function to a number (i.e: an integral) unlike a function, which maps a number to another number.

Unfortunately, on their own the HK theorems do not provide us with enough to actually carry out a DFT calculation. We have no way of calculating this unique

ground state density without the many-body wavefunction, which defeats the purpose of rewriting properties as density functionals. Furthermore, the form of the energy functional is unknown, so given the correct ground state density we still could not calculate the energy or other ground state properties.

2.1 Kohn-Sham Density Functional Theory

In 1965, Kohn and Sham (KS) introduced the first tools to make computing these quantities possible [1]. They developed a self-consistent method for finding the exact ground state electron density produced by a given external potential without the need for the many-body wavefunction. KS also provided one of the first approximations for these unknown energy functionals, which will be discussed in Sec. 2.2.

HK showed a system's energy,

$$E = \langle \Psi | \hat{T} + \hat{V}_{\text{ee}} + \hat{V}_{\text{ext}} | \Psi \rangle \tag{2.1}$$

where Ψ is the many-body wavefunction, $\hat{T}$ is the kinetic energy operator, $\hat{V}_{\text{ee}}$ is the operator for the electron-electron interactions, and $\hat{V}_{\text{ext}}$ is the one-body potential operator, could be rewritten as a functional of the energy:

$$E[n] = F[n] + \int d\mathbf{r} n(\mathbf{r}) v_{\text{ext}}(\mathbf{r}) \tag{2.2}$$

where $F[n]$ is the universal functional and $\int d\mathbf{r} n(\mathbf{r}) v_{\text{ext}}(\mathbf{r})$ is the external potential energy from the interactions between the electrons and nuclei (which are fixed in space). KS took this universal functional, which is the same for every physical system as it does not include the external potential, defined by HK and separated it into components:

$$F[n] = T_{\text{S}}[n] + E_{\text{H}}[n] + E_{\text{X}}[n] + E_{\text{C}}[n]. \tag{2.3}$$

Now, instead of approximating the whole universal functional $F[n]$, we will only need to approximate a piece of it. $T_{\text{S}}[n]$ is the kinetic energy of a system of non-interacting electrons with density $n(\mathbf{r})$, $E_{\text{H}}[n]$ is the hartree energy

$$E_{\text{H}}[n] = \frac{1}{2} \iint d\mathbf{r} d\mathbf{r}' \frac{n(\mathbf{r}) n(\mathbf{r}')}{|\mathbf{r} - \mathbf{r}'|}, \tag{2.4}$$

$E_{\mathrm{X}}[n]$ is the exchange functional

$$E_{\mathrm{X}}[n] = \langle\Phi|\hat{V}_{\mathrm{ee}}|\Phi\rangle - E_{\mathrm{H}}[n], \tag{2.5}$$

and $E_{\mathrm{C}}[n]$ is the correlation functional

$$E_{\mathrm{C}}[n] = \langle\Phi|\hat{T} + \hat{V}_{\mathrm{ee}}|\Phi\rangle - T_{\mathrm{S}}[n] - E_{\mathrm{H}}[n] - E_{\mathrm{X}}[n] \tag{2.6}$$

where Φ is the KS wavefunction. The correlation term corrects for all of the many-body interactions left out of the calculation, which makes it the hardest to approximate. Using the form in Eq. 2.3 for the universal functional, subject to the condition

$$\int d\mathbf{r}\delta n(\mathbf{r}) = 0, \tag{2.7}$$

the equation

$$\int d\mathbf{r}\delta n(\mathbf{r})\left[\frac{\delta F[n]}{\delta n(\mathbf{r})} + v_{\mathrm{ext}}(\mathbf{r})\right] = 0 \tag{2.8}$$

is the same result you would obtain from the variational method of HK if you applied it to a system of non-interacting electrons in the potential

$$v_{\mathrm{S}}(\mathbf{r}) = v_{\mathrm{H}}[n](\mathbf{r}) + v_{\mathrm{XC}}[n](\mathbf{r}) + v_{\mathrm{ext}}(\mathbf{r}). \tag{2.9}$$

This quantity $v_{\mathrm{S}}(\mathbf{r})$ in Eq. 2.9 is the KS potential. Here $v_{\mathrm{XC}}(\mathbf{r})$ is the exchange-correlation potential defined by the functional derivative

$$v_{\mathrm{XC}}(\mathbf{r}) = \frac{\delta E_{\mathrm{XC}}[n]}{\delta n(\mathbf{r})} \tag{2.10}$$

where we have combined the exchange $E_{\mathrm{X}}[n]$ and correlation $E_{\mathrm{C}}[n]$ terms into one exchange-correlation (XC) functional $E_{\mathrm{XC}}[n]$.

Now we examine a fictitious system of non-interacting electrons that yields the same density as a given system of interacting electrons. This fictitious system is referred to as the KS system. These non-interacting electrons are in the KS potential and the resulting KS wavefunction Φ will be a single Slater determinant constructed of orbitals which are solutions to the single-particle Schrödinger equation

$$\Big[-\frac{1}{2}\nabla^2 + v_{\mathrm{S}}(\mathbf{r})\Big]\phi_i(\mathbf{r}) = \epsilon_i\phi_i(\mathbf{r}) \tag{2.11}$$

with density then defined as

$$n(\mathbf{r}) = \sum_{i=1}^{N} |\phi_i(\mathbf{r})|^2. \tag{2.12}$$

These equations may then be solved self-consistently to find the ground-state density of the system. Begin with a guess for the initial density $n(\mathbf{r})$ and construct the associated KS potential from Eq. 2.9. Then, using Eqs. 2.11 & 2.12, find a new $n(\mathbf{r})$. This resulting density goes back in as the initial guess and one continues with this prescription until self consistency is reached.

The energy of the full interacting system is then defined by Eq. 2.2 using the density calculated from the self-consistent KS equations. It is important to note that KS-DFT as formulated is an exact theory and is not an approximation in any way. If the exact XC functional $E_{\mathrm{XC}}[n]$ were known, then this procedure would exactly reproduce the ground-state properties of the interacting system. In practice, approximations of $E_{\mathrm{XC}}[n]$ are used, as the form of the XC functional is not known. Thus, using this approximated XC functional leads to approximate DFT calculations that do not necessarily give the exact solution.

2.2 Density Functional Approximations

These density-functional approximations (DFAs) began with KS when they gave us the first modern XC functional, the local density approximation (LDA) [1]. LDA assumes that the XC energy has the same dependence on the electronic density as a uniform electron gas

$$E_{\mathrm{XC}}^{\mathrm{LDA}}[n] = \int n(\mathbf{r}) \epsilon_{\mathrm{XC}}(n(\mathbf{r})) d\mathbf{r} \tag{2.13}$$

where ϵ_{XC} is the XC energy per particle of a homogeneous electron gas of density $n(\mathbf{r})$. Eventually more complex approximations began to appear, including generalized gradient approximations (GGAs) [8] which utilize the electronic density and the gradient of the density to make a less local approximation. The most commonly utilized GGA is the PBE functional introduced by Perdew, Burke, and Ernzerhof [9]. The increasing complexity of these functionals has been described as a "Jacob's Ladder" of functional

sophistication by Perdew, et al. [10]. Instead of the biblical ladder to heaven [11], we have been climbing a ladder of functional complexity towards chemical accuracy. The rung above GGAs are meta-GGAs, which add the laplacian of the density to the mix [12]. These meta-GGAs may also include (or replace the laplacian with) the kinetic energy density. In the 1990's, hybrid functionals were introduced [13] which replaced some of the GGA exchange with Hartree-Fock exchange. The most commonly used hybrid functional is the B3LYP hybrid [14]. It is also the most commonly used density functional in chemistry today, whereas in the materials realm, PBE still reigns as the most popular [15].

Even though the number of functionals and complexity of said functionals has increased over the years, DFAs still fall short in a couple of important areas. Some of these problems arise due to a lack of van der Waals interactions, which none of the popular functionals (LDA, PBE, & B3LYP) have. Other issues, like static correlation and delocalization errors are due to the improper treatment of fractional spins and fractional charges respectively [4, 16, 17]. DFT as originally formulated was defined only for integer particle number. In order to use densities which integrate to a non-integer number of electrons, one must use an ensemble generalization of DFT as shown by Perdew, Parr, Levy, and Balduz (PPLB) [18], which is discussed further in Appendix A. Modern functionals do not use the ensemble definitions of PPLB and fail to produce the proper behavior of the energy as a function of particle number. The energy of an open system, as a function of the continuous variable N (time-averaged electron number), should be a series of straight line segments, with possible derivative discontinuities at integer N as shown in Fig. A.1 in Appendix A.

This improper treatment of fractional charges and lack of derivative discontinuity in modern XC functionals is the root cause of many errors in DFAs [4, 16, 17, 19–21]. The delocalization error leads to unphysical charge transfer, overestimation of binding energies in charge transfer complexes, and overestimation of responses to an electric field in molecules and materials. It can also lead to underestimation of barriers in chemical reactions, charge transfer excitation energies, energies of dissociating molec-

ular ions, and band gaps of materials. The static correlation error accounts for DFA calculation's failure to describe degenerate states which are common in transition metal systems, chemical bond breaking, and strongly correlated materials [4].

The underestimation of the band gap presented by many groups is not solely due to the failure of the approximate functionals, but due to misconceptions about results from the KS calculations. The fundamental gap is $I - A$, where I is the ionization potential and A is the electron affinity. The KS gap, the difference between the KS HOMO and LUMO energies, is not equal to this value even with exact energy functionals [18, 22]. The orbital energies from a KS calculation are those of a system of non-interacting electrons and are fundamentally different than the gap found from the interacting system. The difference between the KS gap and the fundamental gap is equal to the size of the discontinuity in the derivative of the energy [22]. It is possible to calculate the fundamental gap using DFT [23], but to find it from the KS gap, the derivative discontinuity must be included [24]. This derivative discontinuity is an important aspect for recreating many physical properties of a system but it is not present in approximate XC functionals [20, 25]. Most modern DFAs even fail to recreate the linear behavior of the energy between integer particle number. Approximate functionals that perform well on these types of calculations often do so because of error cancellations or through empirical fitting. Parameter fitting is not an ideal method for constructing functionals as they often fail to fulfill the requirements of the exact functional and thus do not provide general or robust methods which perform well for wide varieties of systems [26]. There has been a shift away from developing functionals that are physically rigorous in which they try to match the constraints of the exact XC functional. Instead there has been a large focus on matching energies of known results for specific systems, which often results in inaccurate densities and thus are moving further away from the exact functional [21, 27].

3. PARTITION DENSITY FUNCTIONAL THEORY

Our solution to many of the problems plaguing DFAs is a density subsystem method, Partition Density Functional Theory (P-DFT) [28, 29]. P-DFT divides a system into non-interacting fragments and calculates system properties in the presence of an added embedding potential which recreates the full interacting system. The approach is analogous to the KS method of modeling interacting electrons by using a system of non-interacting electrons. In KS-DFT the non-interacting electrons are likened to the interacting system through the KS potential $v_{\mathrm{S}}(\mathbf{r})$ while in P-DFT the non-interacting fragments are linked through an embedding potential called the partition potential $v_p(\mathbf{r})$ [30]. Here we focus on the ground state with no effects from the electron spin. For time dependent versions of P-DFT see Ref. [31–33] and for the inclusion of spin indices see Ref. [29, 34].

3.1 Method

The first step in P-DFT is to divide the system into N_f non-interacting fragments. Any choice of fragmentation is permissible as long as the fragment potentials sum to the total external potential

$$v_{\mathrm{ext}}(\mathbf{r}) = \sum_{\alpha=1}^{N_f} v_\alpha(\mathbf{r}). \tag{3.1}$$

Once the set of fragment potentials $\{v_\alpha\}$ is chosen, one may find the correct set of fragment densities for this system $\{n_\alpha\}$. These fragment densities will satisfy the conditions that the sum $n_f(\mathbf{r}) = \sum_\alpha n_\alpha(\mathbf{r})$ is equivalent to the full interacting system's density

$$n(\mathbf{r}) = n_f(\mathbf{r}) = \sum_{\alpha=1}^{N_f} n_\alpha(\mathbf{r}) \tag{3.2}$$

and that the total fragment density integrates to the number of electrons N in the full interacting system

$$N = \int d\mathbf{r} n_f(\mathbf{r}) = \sum_{\alpha=1}^{N_f} N_\alpha \tag{3.3}$$

where N_α is the occupation number of fragment α. P-DFT does not constrain these N_α to be integer numbers, thus an ensemble, as described by PPLB, is used to calculate fragment properties. Fragment densities are calculated as an ensemble of two states with integer occupation:

$$n_\alpha(\mathbf{r}) = w_\alpha n_{p_\alpha+1}(\mathbf{r}) + (1 - w_\alpha) n_{p_\alpha}(\mathbf{r}) \tag{3.4}$$

where p_α is the lower bounding integer of N_α, $0 \leq w_\alpha < 1$, and $N_\alpha = p_\alpha + w_\alpha$. The true ground state fragment densities are those which minimize the sum of fragment energies

$$E_f = \sum_{\alpha=1}^{N_f} E_\alpha[n_\alpha] \tag{3.5}$$

where each fragment energy E_α uses the same ensemble definition as Eq. 3.4

$$E_\alpha[n_\alpha] = w_\alpha E_\alpha[n_{p_\alpha+1}] + (1 - w_\alpha) E_\alpha[n_{p_\alpha}]. \tag{3.6}$$

The set of fragment densities may be found through a minimization of E_α with the constraints given in Eqs. 3.2 & 3.3. By introducing two Lagrange multipliers: the full system's chemical potential, μ, and the partition potential, $v_p(\mathbf{r})$, this constrained minimization can be written as an unconstrained minimization of

$$G[\{n_\alpha\}] = E_f[\{n_\alpha\}] + \int d\mathbf{r} v_p(\mathbf{r})(n_f(\mathbf{r}) - n(\mathbf{r})) - \mu\Big(\int d\mathbf{r} n_f(\mathbf{r}) - N\Big). \tag{3.7}$$

Here, $v_p(\mathbf{r})$ is a global quantity, meaning it is the same for all fragments. Generally in P-DFT calculations, a KS system is used for each fragment. The densities $n_{p_\alpha}(\mathbf{r})$ and $n_{p_\alpha+1}(\mathbf{r})$ are calculated with the orbitals from the fragment KS equations

$$\Big\{ -\frac{1}{2}\nabla^2 + v_\alpha^{eff}[n_{p_\alpha}](\mathbf{r}) + v_p(\mathbf{r}) \Big\} \phi_{i,p_\alpha}(\mathbf{r}) = \epsilon_{i,p_\alpha} \phi_{i,p_\alpha}(\mathbf{r}) \tag{3.8}$$

where

$$v_\alpha^{eff}[n_{p_\alpha}](\mathbf{r}) = v_{\mathrm{H}}[n_{p_\alpha}](\mathbf{r}) + v_{\mathrm{XC}}[n_{p_\alpha}](\mathbf{r}) + v_\alpha(\mathbf{r}) \tag{3.9}$$

and then

$$n_{p_\alpha}(\mathbf{r}) = \sum_{i=1}^{p_\alpha} |\phi_{i,p_\alpha}(\mathbf{r})|^2. \tag{3.10}$$

The eigenvalues from Eq. 3.8 are not directly summed to find the fragment energies as they include contributions from $v_p(\mathbf{r})$. Instead $E_\alpha[n_{p_\alpha}] = \sum_{i=1}^{p_\alpha} \epsilon_{i,p_\alpha} - \int d\mathbf{r} n_{p_\alpha}(\mathbf{r}) v_p(\mathbf{r})$ which subtracts off the partition energy. Solving these equations leads to an exact set of fragment densities $\{n_\alpha\}$ (with the optimized fragment occupations) and the partition potential $v_p(\mathbf{r})$. Since $v_p(\mathbf{r})$ is a global quantity it is unique, up to a constant, for this external potential and choice of fragmentation [35].

To better illustrate these quantities we present the results from a simple example. The full derivation and analysis of these results are shown in Ref. [36] and a slightly more complicated example is shown in Ref. [37]. The system external potential consists of two delta wells in one dimension

$$v_{ext}(x) = -\delta(x-1) - \delta(x+1) \tag{3.11}$$

and will be populated with two non-interacting electrons. Partitioning this system into two fragments with one well per fragment such that $v_1(x) = -\delta(x+1)$ and $v_2(x) = -\delta(x-1)$ will result in identical fragment occupations $N_{1,2} = 1$. The full molecular density $n(x)$, along with the fragment densities $n_\alpha(x)$ found using P-DFT, are shown in Fig. 3.1. Each fragment density $n_\alpha(x)$ is calculated only in the presence of $v_\alpha(x)$ and $v_p(x)$ and when all $n_\alpha(x)$ are summed they produce the full system density $n(x)$.

The exact, unique partition potential for this system, shown in Fig. 3.2, has singularities at the locations of the delta wells in $v_{ext}(x)$ and a smooth well in between the fragments. This well helps to draw the fragment densities towards each other and recreate $n(x)$.

The effects of $v_p(x)$ can be seen in Fig. 3.3 by comparing the fragment density $n_1(x)$, which is in the presence of $v_\alpha(x)$ and $v_p(x)$, to the isolated density $n_1^0(x)$, which is only in the presence of $v_\alpha(x)$.

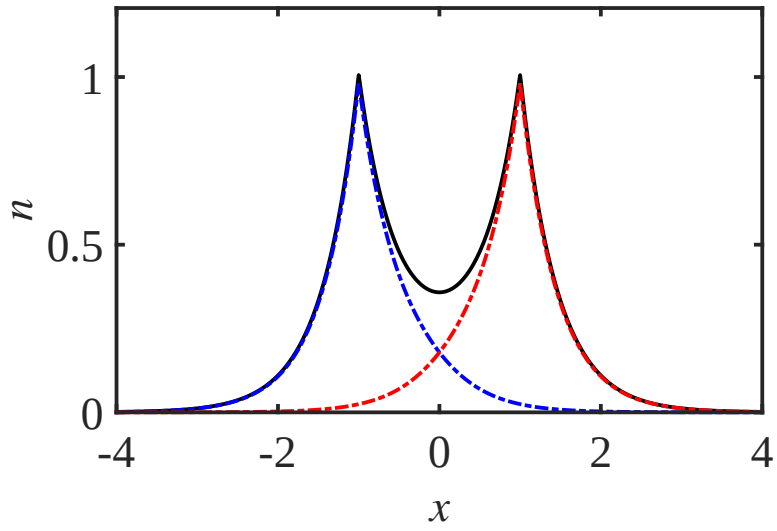

Figure 3.1. The full molecular density $n(x)$ (black line) and the fragment densities $n_\alpha(x)$ from the P-DFT calculation of the simple two well system. These fragment densities $n_1(x)$ (blue dash-dot line) and $n_2(x)$ (red dash-dot line) are calculated separately but sum to the full molecular density due to the addition of the partition potential shown in Fig. 3.2.

The idea of splitting up a larger system into fragments in DFT calculations is not a new one. P-DFT is one of a few fragment density based embedding methods applied within DFT. However, P-DFT is the most generalized version of these embedding methods [38].

3.2 Comparison of Embedding Methods

The common features of density based embedding methods are the partitioning of the system into smaller non-interacting pieces, rewriting the total energy functional in terms of the set of fragment densities, and the application of some embedding potential to these fragments (in our case v_p) that encodes the missing interactions between fragments. These fragment based methods are well suited for linear scaling and parallelization. There are many recent reviews on the various embedding methods

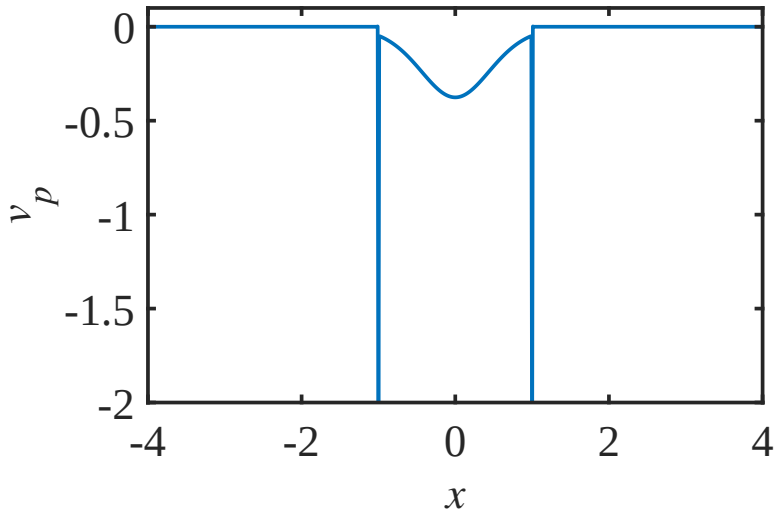

Figure 3.2. The exact partition potential $v_p(x)$ which is applied to both fragments and uniquely corresponds to this specific system and choice of fragmentation. There are singularities in $v_p(x)$ at the location of the delta wells in the external potential and a smooth well in between the fragments.

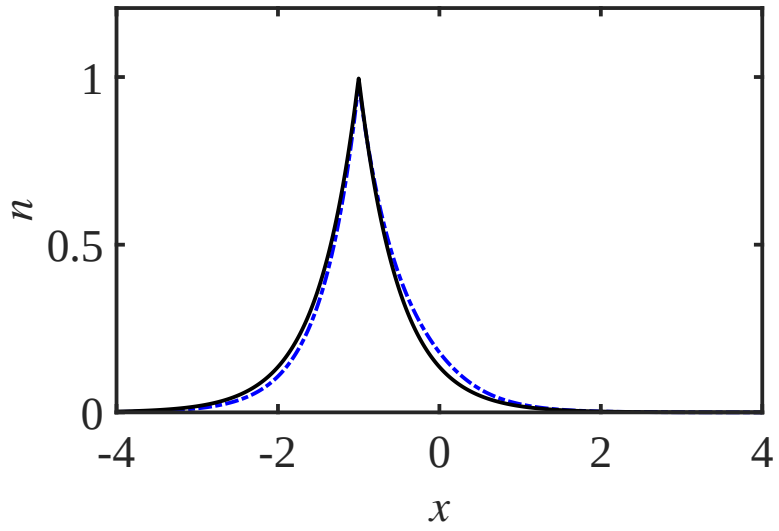

Figure 3.3. The left side fragment density $n_1(x)$ (blue dash-dot line) compared to the density from an isolated delta potential well $n_1^0(x)$ (black line) demonstrates the effects of the partition potential shown in Fig. 3.2.

[39–41], including detailed comparisons to P-DFT [21,29], so we will focus on the most important similarities and differences between the techniques.

In 1991 Cortona introduced a fragment based method, referred to as Subsystem DFT (S-DFT), which minimized the total energy with respect to each of the fragment densities while updating all fragment densities simultaneously until reaching self consistency [42]. S-DFT forces the fragments to have integer numbers of electrons, which is often done because it allows for use with correlated wavefunction methods [29,38]. However, this constraint may result in fragment densities which are not localized to their fragment. In the original formulation of S-DFT each fragment is allowed to have a different embedding potential, meaning that the embedding potentials in S-DFT were not unique. There could be an infinite set of fragment densities and embedding potentials that yield the same results. The uniqueness of the embedding potential was eventually realized in S-DFT when Carter et al., inspired by P-DFT, used a global embedding potential which is the same for all fragments [38].

In 1993 Frozen-Density Embedding (FDE) was developed by Wesolowski and Warshel [43]. They partition systems into two non-interacting fragments: an active fragment and the environment. The density of the environment is frozen and used to create an embedding potential for the active fragment. The density of the active fragment is calculated in the presence of this embedding potential. This method can become a self-consistent method by having freeze-thaw cycles which alternate the active fragment and frozen fragment. FDE and S-DFT are equivalent when this freeze-thaw cycle is implemented.

Govind et al. developed a method which combined these ideas with the concept that subsystems could be treated with different levels of theory [44]. This process of embedding higher accuracy calculations into a DFT calculation is often referred to as Embedding DFT and may be used in S-DFT and P-DFT.

P-DFT differs from S-DFT and FDE in that it minimizes the sum of fragment energies instead of the total energy. By minimizing fragment energies we remove

the extra step of combining fragment densities and calculating the total energy as a functional of n_f.

One of the most important distinctions between P-DFT and other density-based embedding methods is that we allow for non-integer occupation numbers and properly treat possible fractional charges through the ensemble definitions introduced by PPLB when calculating fragment properties [37, 45]. By using an ensemble we only evaluate energy functionals at integer occupation numbers, never using a density that integrates to a fractional particle number in the functional. Most approximate density functionals work well for localized densities having an integer charge, but fail when using fractional pieces [29]. Other subsystem methods have been working on allowing fragments with fractional charge [46]. However, instead of using the correct ensemble definition from PPLB, generally they fractionally occupy the HOMO from a KS calculation. Thus they use a density which integrates to a non-integer number of electrons to evaluate the energy functionals.

As P-DFT allows for non-integer N_α, when we optimize the occupation number we always obtain the most localized fragment densities. Due to this we are able to see the correct charge transfer behavior [37] and our resulting fragment properties and partition potentials are chemically meaningful [47, 48]. P-DFT's proper treatment of fractional charges corrects many of the self-interaction and delocalization errors in DFAs mentioned in Sec. 2.2, even when using the same XC functionals [5, 21, 25, 45].

3.3 Approximations to the Partition Potential

The formulation for P-DFT in Sec. 3.1 is exact and no approximations are made, but like the original prescription for DFT, approximations are required for practical calculations. We are working on multiple fronts towards accurately approximating the partition potential $v_p(\mathbf{r})$ for different types of systems.

The exact v_p in small finite systems has been studied from inversions on chains of atoms with non-interacting electrons [28, 49], diatomic systems [29, 30, 50], and

most recently, water dimers [51]. From these inversions methods to do approximate P-DFT calculations have been developed and implemented in systems of diatomic molecules [29, 52] and work has been done towards making approximations to v_p itself in diatomic molecules with covalent bonds [53,54]. Using these approximations, errors caused by improper treatment of fractional occupations and spins were greatly reduced in dissociation curves of diatomic molecules [5, 29].

Here we extend this study of v_p to include infinite and semi-infinite systems, those whose energy and density are characterized by the system chemical potential instead of the total number of electrons. We exactly study simple systems which mimic a metal-atom or metal-molecule interface (a semi-infinite system) and molecular crystals or periodic atomic chains (an infinite system). We are particularly interested in cases where there is charge transfer or where electrons are not fully localized to one part of a system (regions of large density overlap). In these cases the fragments often have fractional occupations. We find and study the *exact* v_p for these extended systems towards one day creating more approximations to the partition potential. As the exact v_p is found through an inversion from the full system density, we must be able to produce accurate densities before attempting to find v_p. Once accurate densities are found, we use an inversion method based on the system type to find the exact v_p corresponding to that density and the choice of fragmentation.

In all of the following calculations, we study 1-D systems populated by non-interacting, spin-less electrons.

4. INVERSION METHODS

By inverting from the exact total system, or reference, density $n_{ref}(x)$, we are able to find the exact partition potential $v_p(x)$. All inversions are done on a real space grid to avoid problems and inaccuracies which can arise when using basis sets [29, 55].

The two types of systems we have, finite and semi-infinite, require different inversion methods. Although they are different, they follow the same basic outline. After calculating the reference density $n_{ref}(x)$, the external potential is split into a set of fragment potentials $\{v_\alpha\}$. We make an initial guess for the partition potential $v_p^0(x)$ and the fragment occupations N_α^0. Using $v_p^0(x)$ we calculate the corresponding set of fragment densities $\{n_\alpha\}$ and the fragment energies E_α. With these we make a new guess for the partition potential $v_p^1(x)$ and fragment occupations N_α^1. This process continues until our constraints are satisfied and we reach convergence.

4.1 Fixed N_α Inversions

Finite system's properties are characterized by the total number of electrons in the system. Inversions on these systems utilize the minimization procedure laid out in Sec. 3.1. The sum of fragment energies is minimized under the constraints that 1.) The sum of fragment densities equals the reference density, and 2.) The fragment occupations add up to the number of electrons in the reference system. Through the addition of two Lagrange multipliers, μ and $v_p(x)$, this can be done as an unconstrained minimization of Eq. 3.7. This method of inverting has been done before to study the exact partition potential of finite systems [50].

Our simplest inversion method holds the fragment occupations at fixed values which are chosen before the inversion begins. Fragment occupations are chosen such

that they sum to the total system electron number, thus we may drop the last term in Eq. 3.7 and simply minimize:

$$G[n_\alpha] = E_f[n_\alpha] + \int dx v_p(x)(n_f(x) - n_{ref}(x)) \tag{4.1}$$

The minimization of G is done by using the gradient and hessian in an interior reflective Newton method which converges when $n_f(x) = n_{ref}(x)$ and the fragment energies are minimized.

The process of this inversion is outlined in Fig. 4.1. The system is defined by choosing the external potential and the total number of electrons in it. These are used to find the reference density which will be used in the convergence checks. Next, the system is partitioned by choosing the fragment potentials and fragment occupations. Once these are done the actual inversion begins which is an iterative process. In the first step of the iteration we pick an initial guess for $v_p(x)$, which is usually chosen to be zero at all points. At this step and all subsequent steps we then calculate the fragment properties, $n_\alpha(x)$ and E_α, using the current guess of $v_p(x)$. Summing these properties gives us the total fragment energy E_f, which we are trying to minimize, and the total fragment density $n_f(x)$. If this $n_f(x)$ is equal to the reference density and these values minimize G in Eq. 4.1, then we have converged and the inversion is complete. If these are not true, then the guess for the partition potential is updated using the gradient and hessian of G and the next step of the iteration begins.

In some systems the correct fragment occupations will be known, there is no need to optimize N_α, and this method gives the exact P-DFT results. For example, partitioning a homonuclear diatomic system with two electrons into atomic fragments would result in fragment occupations $N_\alpha = 1$. In these cases this inversion method produces the correct well-localized fragment densities with no need to optimize N_α. For more complex systems it is not as straightforward to know or guess the correct occupations, especially when they are non-integer values. In these cases the same procedure may be done, but could result in non-localized fragment densities and an embedding potential that is not the true partition potential. Results from this fixed N_α inversion method are shown in Secs. 5.2, 6.1, and 6.2.

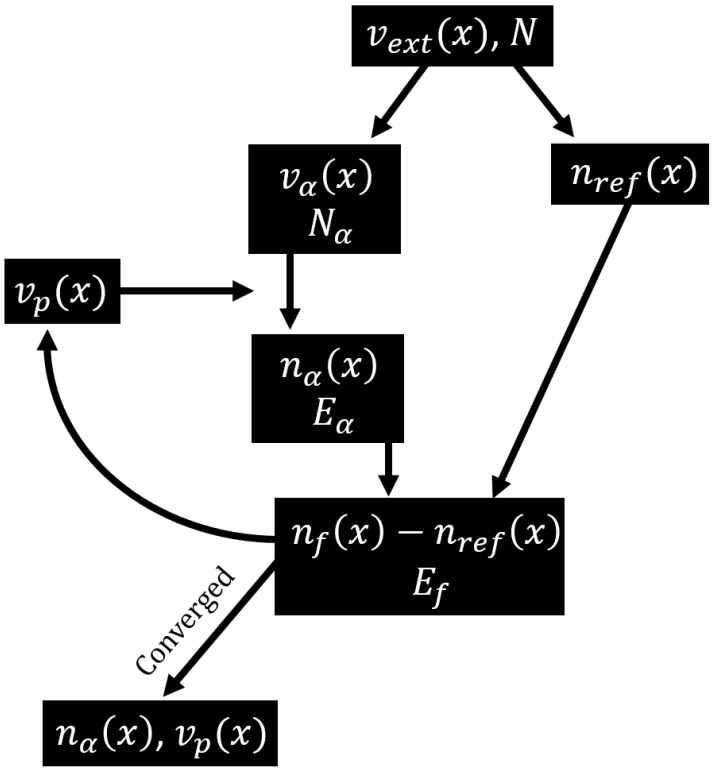

Figure 4.1. A simple flowchart of the fixed N_α inversion method. The reference density $n_{ref}(x)$ is calculated from the total system properties $v_{ext}(x)$ and N. The system is then partitioned by choosing the fragment potentials $v_\alpha(x)$ and occupations N_α. An initial guess of $v_p(x) = 0$ is used for the first iteration. The fragment properties are calculated and summed, $n_f(x)$ and E_f. If these values minimize G (Eq. 4.1) it has converged and the $v_p(x)$ and fragment properties are saved. If it has not converged, then the guess for $v_p(x)$ is updated and the process continues.

4.2 Semi-Infinite System Inversion

In the original formulation of P-DFT, the solution is found by the constrained minimization of the sum of fragment energies laid out in Sec. 3.1. For an infinite or semi-infinite system where the density is non-zero as $x \to \pm\infty$, there is a continuum of states and thus an infinite energy. In this case a constrained minimization of the total energy as shown in 3.1 cannot be used to find the solution.

The two constraints in P-DFT calculations are 1.) The fragment densities sum to the full system density and 2.) The sum of fragment occupations is equal to the number of electrons in the total system. For an infinite system with infinitely many electrons, the second constraint is always satisfied and thus not useful for ensuring the correct solution for the partition potential and fragment densities. To find exact results for the metal-atom system we study, a new chemical potential constrained P-DFT inversion method was developed. As far as we know, no previous work has been done on inversions of this type for studying interfaces. We present our new inversion method as applied to our metal-atom interface.

It has been shown that the electronegativity equalization principle for Atoms in Molecules is equivalent to their chemical potential equalization [35, 45]. For a system with charge transfer or an electron being shared between fragments, the μ_α of the fragments equalize to the total system μ. In cases where our atomic fragment, having a finite number of electrons, has an integer occupation number, N_{atom}, the μ_α do not necessarily equalize between the metal and atom fragments [49]. Instead the atomic fragment eigenvalues ε_{HOMO} and ε_{LUMO} will encompass the full system μ [56]

$$\varepsilon_{HOMO} \leq \mu \leq \varepsilon_{LUMO}. \tag{4.2}$$

This relation is satisfied for both fractional and integer occupation numbers (when the μ_α equalize and when they do not). The constrained energy minimization normally done in P-DFT is now replaced by a search for the v_p which satisfies the constraint of Eq. 4.2 along with the constraint that the fragment densities sum to the reference density. Thus there is either chemical potential equalization between fragments, in the case of fractional N_{atom}, or the system chemical potential falls between the HOMO and LUMO eigenvalues of the atomic fragment, for integer N_{atom}.

With these new constraints we follow an inversion method similar to that of the previous section. A simple outline is shown in Fig. 4.2. An iterative gradient descent method will find $v_p(x)$ along with the corresponding $n_\alpha(x)$ for a given μ. These $n_\alpha(x)$ are those which sum to the total density $n_{ref}(x)$ and either equalize our fragment μ_α or satisfy the convergence condition for integer N_{atom} in Eq. 4.2.

We begin the inversion by making an initial guess for N_{atom}. A good initial value for the fragment occupation of the atom is critical to quickly getting accurate results in our iterative scheme. To do this we calculate the density of the full system for a chosen μ. This is our reference density, $n_{ref}(x)$, which is used throughout our inversion. The isolated metal density $n^0_{metal}(x)$ is the density corresponding to $v(x) = v_{metal}(x)$ which has no contributions from $v_p(x)$ and has the same μ as the full system. The density for the isolated atom, $n^0_{atom}(x)$, is only in the presence of $v(x) = v_{atom}(x)$ with no contributions from $v_p(x)$. These isolated densities and the eigenvalues of the isolated atomic fragment are found. We split the atomic density into the core region $n_{core}(x)$ and the valence region, $n_{valence}(x)$, which is the density of the HOMO. The number of states included in the core region, N_{core}, is equal to the number of eigenvalues of the isolated atom which are below the μ of the system. In cases where μ is below the lowest atomic eigenvalue, the core density is zero. Before finding N_{atom}, we find the fractional piece of the occupation number, ω. For the correct fragment densities

$$\int dx n_{ref}(x) - n_{metal}(x) - n_{core}(x) - \omega n_{valence}(x) = 0. \tag{4.3}$$

We may replace the fragment densities in the equation with the isolated fragment densities ($n_{metal}(x) \to n^0_{metal}(x)$, etc) to get a reasonable initial approximation for the fractional part of the occupation number, ω^0

$$\omega^0 = \int dx [n_{ref}(x) - n^0_{metal}(x) - n^0_{core}(x)]/n^0_{valence}(x) \tag{4.4}$$

Adding this to the integer number of electrons in the core region gives us our initial guess for the occupation number,

$$N^0_{atom} = N_{core} + \omega^0. \tag{4.5}$$

At the ith step of our iteration we input our guess for N^i_{atom} and $v^i_p(x)$. For the 1st iteration we use $N^1_{atom} = N^0_{atom}$ found from Eq. 4.5 and $v^1_p(x) = 0$. Although we will be using the notation $v^i_p(x)$ and $v_p^{i+1/2}(x)$ for simplicity, these are not the correct partition potentials until the inversion is complete. These are global potentials which

are intermediate steps to getting the final $v_p(x)$. At each iteration i, using $v_p^i(x)$ as the initial guess, we find the global potential which, for fixed N_{atom}^i, minimizes the difference between $n_{ref}(x)$ and $n_f^i(x) = \sum_\alpha = n_\alpha^i(x)$ to numerical precision. The potential that results from this minimization is $v_p^{i+1/2}(x)$. The 1/2 is due to this being a halfway point between $v_p^i(x)$ and $v_p^{i+1}(x)$. We will change $v_p^{i+1/2}(x)$ before beginning the next step of the iteration. Using $v_p^{i+1/2}(x)$, μ, and N_{atom}^i we find the fragment densities $n_\alpha^i(x)$. From these densities we calculate the fragment responses $\chi_\alpha^i(x, x')$ with respect to small changes in the potential:

$$\chi_\alpha^i(x, x') = \frac{dn_\alpha^i(x)}{dv_{eff,\alpha}^i(x')} \tag{4.6}$$

where $v_{eff,\alpha}^i(x') = v_\alpha(x') + v_p^{i+1/2}(x')$.

We find the fragment chemical potentials μ_α^i which are necessary for the convergence check. The metal fragment chemical potential μ_{metal}^i is equal to the reference system chemical potential μ at each step of the inversion. $\mu_{metal}^i = \mu$ for all i. The atomic fragment chemical potential is the atom's HOMO eigenvalue, which includes the energy contributions from $v_p^{i+1/2}(x)$. For our inversion to end, one of the two convergence criteria must be met: 1.) The difference between μ_α^i must be below numerical precision or 2.) N_{atom}^i is an integer value and $\varepsilon_{HOMO}^i < \mu < \varepsilon_{LUMO}^i$. If we have converged, then the final results are: $v_p(x) = v_p^{i+1/2}(x)$, $n_{atom}(x) = n_{atom}^i(x)$, $N_{atom} = N_{atom}^i$, and $\mu_{atom} = \mu_{atom}^i$.

If neither 1 nor 2 are met, we continue with our gradient descent method by varying N_{atom}^i and $v_p^{i+1/2}(x)$ using the responses from Eq. 4.6 and the difference between the μ_α^i. We find how $v_p^{i+1/2}(x)$ and μ_{atom} respond to small changes in N_{atom}^i [57] by solving:

$$f^i(x) = \int dx' [\chi_{metal}^i(x, x') + \chi_{atom}^i(x, x')] \frac{dv_p^{i+1/2}(x)}{dN_{atom}^i} \tag{4.7}$$

where $f^i(x)$ is the Fukui function, which in this case is simply the density of the atomic fragment HOMO [58, 59]. From here we may find the response of μ_{atom} to changes in N_{atom}

$$\frac{d\mu_{atom}^i}{dN_{atom}^i} = \int dx f^i(x) \frac{dv_p^{i+1/2}(x)}{dN_{atom}^i}. \tag{4.8}$$

From Eqs. 4.8 and 4.7 along with the difference between the μ^i_α, we get the changes:

$$dN^i_{atom} = \frac{\mu^i_{metal} - \mu^i_{atom}}{\frac{d\mu^i_{atom}}{dN^i_{atom}}} \tag{4.9}$$

and then the corresponding change in $v_p^{i+1/2}(x)$

$$dv_p^{i+1/2}(x) = \frac{dv_p^{i+1/2}(x)}{dN^i_{atom}} dN^i_{atom} \tag{4.10}$$

These are used to find the guess for the next iteration: $N^{i+1}_{atom} = N^i_{atom} + dN^i_{atom}$ and $v_p^{i+1}(x) = v_p^{i+1/2}(x) + dv_p^{i+1/2}(x)$. We begin the iterative process again until convergence is reached. A simple illustration outlining the iterative inversion is shown in Fig. 4.2 and results from this method are shown in Sec. 5.3.

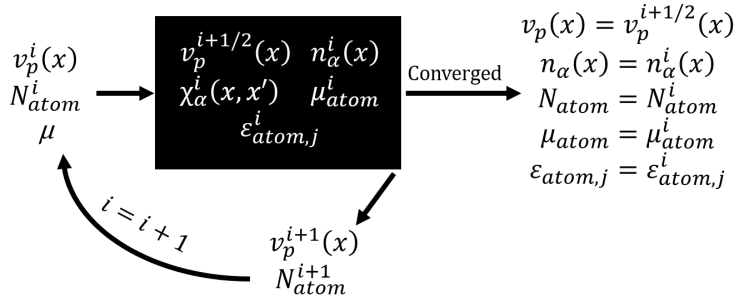

Figure 4.2. A simple flowchart of the mixed system inversion. At the ith step the current guess for $v_p(x)$ and N_{atom} along with the system μ are inputs to the minimization and gradient calculations (shown as a black box) producing the quantities in the black box. If the convergence checks are satisfied by these, they are the final results. If it is not converged, the gradients of the functions are calculated and used to update the guesses, $v_p(x)$ and N_{atom}. This process continues until convergence is reached.

4.3 N_α Optimization

The fragment occupation numbers could be optimized by minimizing Eq. 3.7, but it is computationally quicker to use a method more analogous to Sec. 4.2. Instead

of minimizing G, we solve for the values of $v_p(x)$ which satisfy the constraint that $n_f(x) = n_{ref}(x)$ and the values of N_α which satisfy the constraint

$$\mu_{\alpha,min} \leq \mu \leq \mu_{\alpha,max} \tag{4.11}$$

where $\mu_{\alpha,min(max)}$ is the minimum(maximum) of the fragment chemical potentials. Here we are directly solving for the points where the gradient and hessian of G are zero instead of minimizing G. The effect and results are the same.

We utilize the fsolve routine in MATLAB which uses a trust-region dogleg method to solve sets of nonlinear equations. Solving:

$$(n_f(x) - n_{ref}(x)) + \sum_\alpha (\mu_\alpha - \mu) = 0 \tag{4.12}$$

and

$$\sum_\alpha \chi_\alpha(x, x') + \sum_\alpha f_\alpha(x) = 0, \tag{4.13}$$

where $\chi_\alpha(x, x')$ are the responses of the fragment densities $n_\alpha(x)$ with respect to changes in $v_p(x')$ and $f_\alpha(x)$ is the Fukui function, leads to the correct $v_p(x)$ and N_α, except for those cases in which a value of N_α is an integer.

When there is a fractional component to all N_α the μ_α equalize to each other and to the system μ. For most cases where there is an integer N_α there is not equalization of the fragment chemical potentials, but they behave as in Eq. 4.11. If our fsolve routine fails to converge it means that not all N_α have fractional occupations. We then take the final N_α and adjust them so that one or more are integer values while ensuring that the N_α still sum to N. With these N_α we use the fixed N_α inversion and check that the resulting fragment chemical potentials obey the constraint of Eq. 4.11. A simple flowchart of this routine is shown in Fig. 4.3 and results of this inversion method are shown in Sec. 6.2.

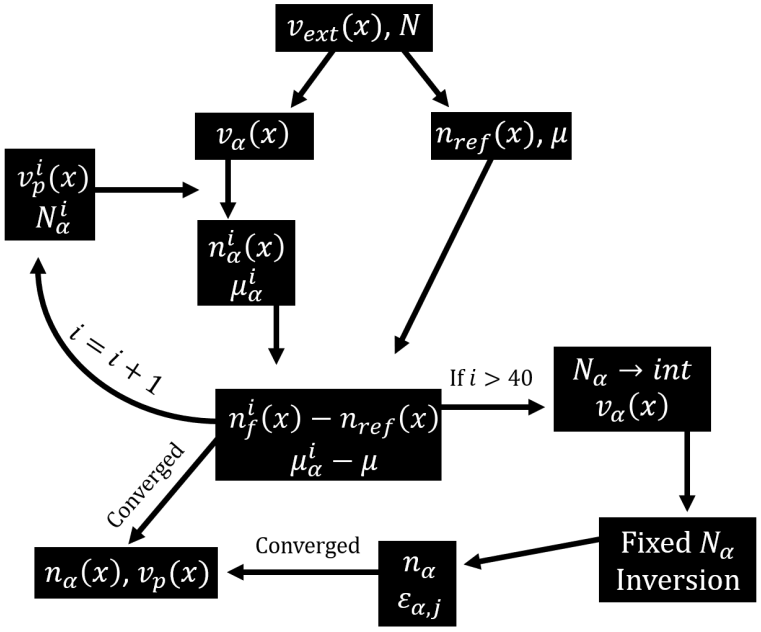

Figure 4.3. A simple outline of the N_α optimizing inversion. The reference density $n_{ref}(x)$ and μ are calculated from the total system properties $v_{ext}(x)$ and N. The system is then partitioned into its fragment potentials $v_\alpha(x)$. Initial guesses of N_α^0 and $v_p^0(x) = 0$ are used for the first iteration. The fragment properties are calculated for the ith iteration $n_\alpha^i(x)$ and μ_α^i. If these values fulfill the constraints it has converged and we get our final answers. If it has not converged yet, we go to the next iteration updating $v_p(x)$ and N_α and the process continues. If it does not converge after 40 iterations, the N_α are fixed to integer values. These are used in the fixed N_α inversion from Sec. 4.1. If these fulfill the chemical potential constraints, we have reached convergence and these are the final results.

5. SEMI-INFINITE SYSTEM

DFT has been an important part of studying material properties and interactions since its development. The first computational prediction of a superconducting material was made in 1984 using DFT [60]. As DFAs become more robust, they still struggle when dealing with charge transfer or sharing of electrons. In many areas of physics and chemistry there is a large interest in studying charge transfer at metal or semiconductor surfaces in association with catalysis, photovoltaics, thin films, and adsorption processes. Experiments to study these charge transfer processes are often expensive and challenging and the results are commonly presented in conjunction with a DFT calculation [61, 62]. DFAs can struggle to replicate the results. This is often due to the improper treatment of fractional charge during charge transfer processes, which causes errors in energy level and band alignment. Work is being done to make new approximate functionals towards recreating the experimental observations [63–67]. Many of these functional approximations use empirical fitting instead of creating more robust functionals that resemble the exact XC functional. With P-DFT there is not necessarily a need for more complex approximate functionals to accurately study charge transfer.

Work has been done by other groups towards using another subsystem method, FDE, to study charge transfer [68–70]. Specifically, there has been a focus on bulk materials and surfaces [71, 72]. When the density overlap between subsystems is small, these methods perform better than standard KS-DFT calculations [72]. However, when there is partial charge transfer or covalent characteristics to the interactions between subsystems, FDE fails. The larger the density overlap, the poorer the performance of FDE. This is mainly due to their restriction that fragments must have integer occupation numbers, which, in these cases of partial charge transfer or electron sharing, causes non-localized fragment densities. These systems with partial charge

transfer and strong fragment interactions are the hardest to study quantitatively and are the most important in studying the reactions at surfaces [61, 62, 65, 69, 73]. Due to the well localized fragment densities P-DFT produces, along with the ensemble treatment of fragment properties, P-DFT is well suited for studying charge transfer even with simple functionals [5, 37].

It is known that for an open system interacting with a distant reservoir the total energy as a function of electron number is a series of straight line segments with cusps at integer values of N, which results in discontinuities in μ as a function of N [18]. At finite temperatures these discontinuities are smoothed and the behavior of E becomes rounded. It has also been supposed, but until now not shown, that this smoothing could also occur due to finite separations between the system and reservoir instead of at finite temperatures [22]. Our metal-atom interface can mimic an open system (the atom) interacting with a reservoir (the metal) discussed in PPLB. Using P-DFT, which allows fragments to have fractional charges, we are able to accurately describe the charge transfer and thus show the smoothing of μ vs N at finite separations.

Inverting these systems also allows us to study features of the partition potential towards one day developing approximations to v_p. The partition potentials that result from the semi-infinite system share properties that are common to v_p's seen in systems of diatomic molecules that have been previously studied. In our simple system, we also see similarities between features in v_p to features of the exact KS-potential for heteronuclear systems. Using non-interacting electrons allows us to find exact results while still seeing realistic behavior for the charge transfer between the systems.

5.1 Analytic Density Calculation

To study the density of this system, we start with the simplest representation of an atom and metallic reservoir which may be solved exactly. The reservoir is represented

by a step potential which interacts with our atomic potential, a delta well. The total external potential is then:

$$v_{ext}(x) = -V_0\Theta(x+d) - Z\delta(x) \tag{5.1}$$

where V_0 is the height of the potential step, d is the separation between the surface and the atom, and Z is the strength of the delta potential. This system is populated with non-interacting electrons up to a chosen energy, or Fermi level E_F as shown in Fig. 5.1.

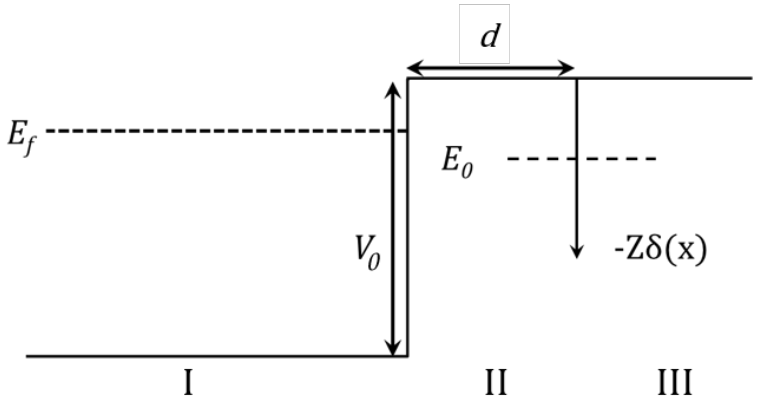

Figure 5.1. A simple illustration of the potential in Eq. 5.1. The surface of the reservoir is a step potential of height V_0 separated a distance d from the atomic potential. The atom is modeled as a delta well of strength Z centered at $x = 0$. This system has three main regions of interest: I.) Inside the reservoir, II.) The interface between the atom and the surface, and III.) The region beyond the center of the delta well. We populate this system with non-interacting electrons up to a chosen Fermi level, E_F. The Fermi level is varied in relation to the isolated bound state energy of the delta potential, E_0.

The density will be a piecewise function:

$$n(x) = \begin{cases} n_I(x) & x < -d \\ n_{II}(x) & -d < x < 0 \\ n_{III}(x) & x \geq 0 \end{cases} \tag{5.2}$$

Each region's density:

$$n_I(x) = \frac{k_F}{\pi} + \frac{1}{\pi}\int_0^{k_F} \frac{1}{\tilde{c}}\{\tilde{a}\cos[2k(x+d)] - \tilde{b}\sin[2k(x+d)]\}dk \tag{5.3}$$

$$n_{II}(x) = \int_0^{k_F} \Big(\frac{z}{k'}\Big)^2 \tilde{d}\Big(1+\frac{\tilde{a}}{\tilde{c}}\Big)\Big\{e^{2k'x} + \Big(\frac{k'}{z}-1\Big)^2 e^{-2k'x} + 2\Big(\frac{k'}{z}-1\Big)\Big\}dk \tag{5.4}$$

$$n_{III}(x) = \int_0^{k_F} \tilde{d}\Big(1+\frac{\tilde{a}}{\tilde{c}}\Big)e^{-2k'x}dk \tag{5.5}$$

Here, $k = \sqrt{2E}$, $k' = \sqrt{2V-k^2}$, $k_F = \sqrt{2E_F}$, and

$$\begin{aligned}
\tilde{a} &= (k'-z)^2(k^2-k'^2)e^{2k'd} + 2z(k'-z)(k^2+k'^2) + z^2(k^2-k'^2)e^{-2k'd} \\
\tilde{b} &= 2kk'[(k'-z)^2e^{2k'd} - z^2e^{-k'd}] \\
\tilde{c} &= (k'-z)^2(k^2+k'^2)e^{2k'd} + 2(k'-z)z(k^2-k'^2) + z^2(k^2+k'^2)e^{-2k'd} \\
\tilde{d} &= \frac{k'^2}{\pi z^2}\frac{1}{[e^{-k'd} + (\frac{k'}{z}-1)e^{k'd}]^2}.
\end{aligned}$$

While these expressions are complex, the general behavior of each region can be seen. Region I is characterized by oscillations about the constant value $\frac{k_F}{\pi}$. The density in region II will exponentially decrease away from the surface and exponentially increase as in approaches the delta well. In region III the density exponentially decays as $x \to \infty$. Numerical integration of these expressions yields the total density which we study for varying values of E_F and d.

At large separations, as we vary the Fermi level above and below E_0, the density and occupation number of the atom N_{atom} jumps abruptly as shown in Fig. 5.2. When $E_F < E_0$, $N_{atom} = 0$ and there is no density around the delta well. As we increase to $E_F \geq E_0$, we suddenly see electron density around the atom and $N_{atom} = 1$.

Integrating the density in region III and doubling, as shown in Fig. 5.3, yields a reasonable approximation for the occupation number on our atom N_{atom}. At large d, this produces very accurate results as the density centered at the atomic potential is almost exactly symmetric about the delta well. For very small separations ($d < 3$), the distortions to the atomic density as it increasingly interacts with the surface become too large for this to be as accurate of an approximation for N_{atom}. Due to

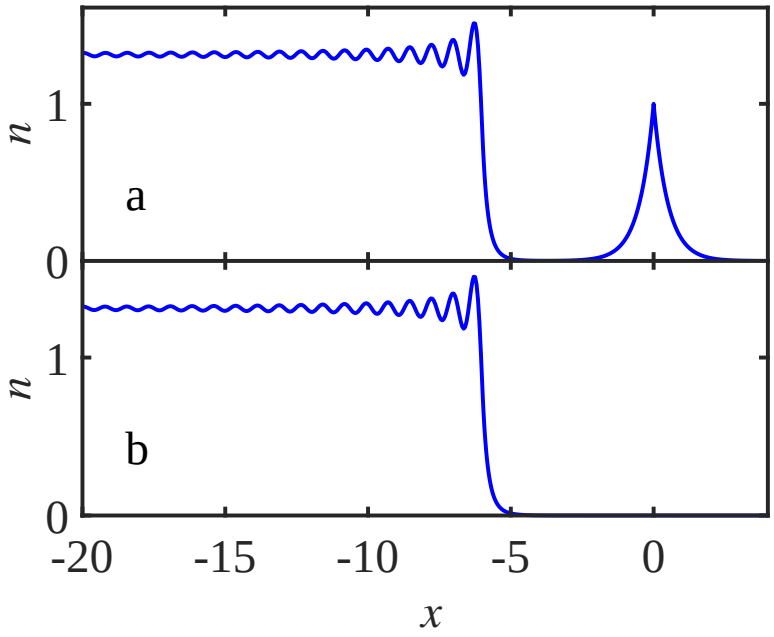

Figure 5.2. The analytic density from Eq. 5.2 produced by the external potential in Eq. 5.1 when $d = 6$, in the cases where a) $E_F > E_0$ and b) $E_F < E_0$.

peaked nature of the density produced by a delta well, the approximation of N_{atom} works well for $d \geq 3$. As d decreases below this, the density around the atom deforms and begins to overlap with the reservoir density and the approximation becomes less accurate. Smoothing of N_{atom} vs μ, shown in Fig. 5.4, is still seen before this point. At large separations we see the expected jump at integer N_{atom}, but as we approach the surface this jump smooths and we see sharing of the charge between fragments resulting in a fractional occupation on the atom. Some of this behavior found by our simple approximation to N_{atom} has been shown in calculations of real metal surfaces interacting with molecules [65, 74].

Inverting this density exactly to find the partition potential was not feasible as we could not analytically find the fragment densities that would result from the addition of v_p. Numerical calculations of the fragment densities on a spatial grid would not be able to exactly reproduce this reference density due to approximations that would be required when modeling the delta well in the potential. However, this analytic

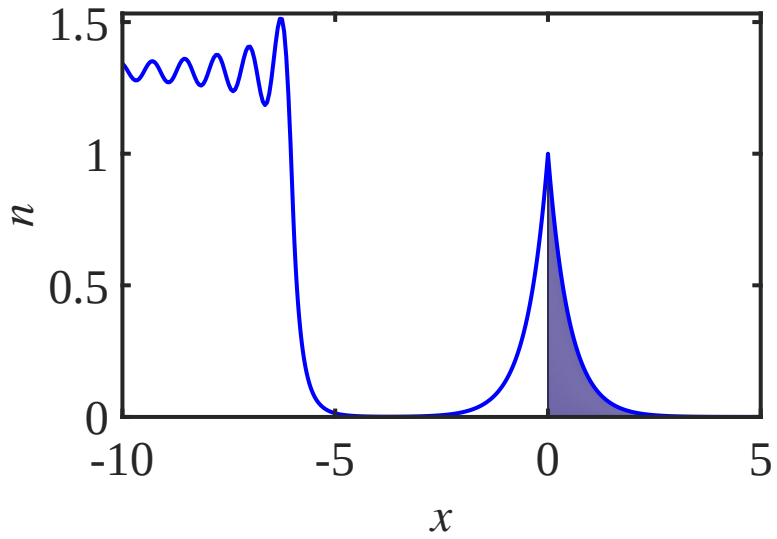

Figure 5.3. The density localized about the delta well is approximately symmetric. By taking twice the integral of the density in Region III (shaded region), we may approximate the atomic occupation number N_{atom}.

solution of the density for the semi-infinite system was a good reference for checking the behavior of the numerical densities found in the following sections.

5.2 Finite Metal Surface

As mentioned in Sec. 3.3 and 4.2, the biggest hurdle in inverting these (semi)infinite systems is the need to reformulate P-DFT into a chemical potential constrained method. The main region of interest, where the largest density deformation occurs, is at the interface between the metal and atom. Therefore, working with a finite version of the system was a useful starting point for this study before the new inversion method from Sec. 4.2 was fully developed.

Simulations are done on a finite 1-D spatial grid, which means the delta well representing the atom would need to be approximated, causing inaccuracies even with a very small spatial step size. To mitigate this, the atomic potential is switched

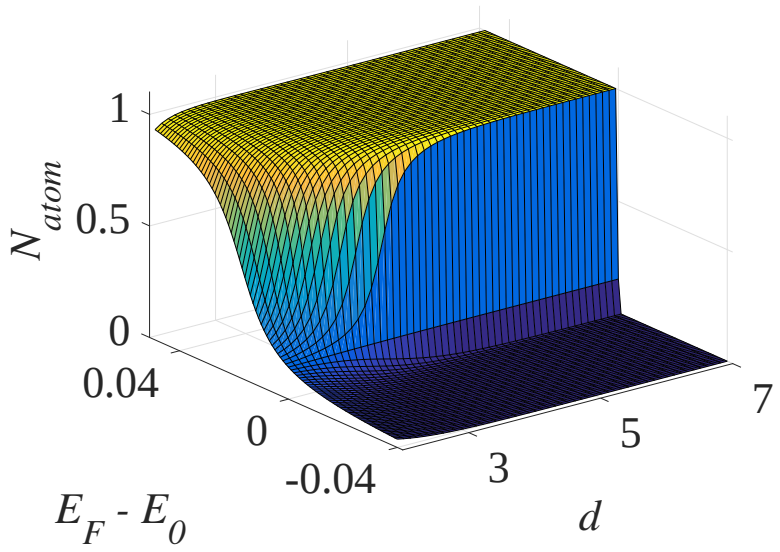

Figure 5.4. The estimated occupation number of the atom N_{atom} given by the analytic solution as the separation between the surface and atom, d, and the chosen Fermi level E_F are varied. The chemical potential of this system is equal to the Fermi level energy $\mu = E_F$. At large separations, N_{atom} vs μ behaves as expected for an atom interacting with a reservoir infinitely far away as discussed in PPLB [18] and Appendix A. As the separation decreases, the step-like behavior smooths out.

from a delta well to a Pöschl-Teller potential, which is commonly used to represent the nuclear potential of atoms. The external potential for this finite system is now:

$$v_{ext}(x) = -V_0\Theta[x + (d + L)] + V_0\Theta[x + d] - Z\cosh^{-2}(x) \tag{5.6}$$

where V_0 is the strength of the potential step, d is the separation between the surface and the center of the atomic potential, L is the total length of the potential well for our metal, and Z is the strength of the atomic potential. For the finite system we choose $Z = 1$ which produces the same isolated bound state energy E_0 as the delta well of strength $Z = 1$ used in the previous section.

5.2.1 Fragment Calculations

The Hamiltonian of our system of non-interacting electrons

$$H = -\frac{1}{2}\frac{d^2}{dx^2} + v(x), \tag{5.7}$$

where $v(x)$ is either $v_{ext}(x)$ or $v_\alpha(x) + v_p(x)$ is written as a matrix using fourth-order finite differences for the second derivative. Diagonalizing produces the eigenstates and eigenvalues of the full system or fragments. When calculating the reference density we chose the following system properties: $L = 25$, $d = 5$, $V_0 = 3.66$, and $N = 42$. The reference density is found using Eq. 5.6 in our matrix version of Eq. 5.7. We sum the square of the contributing eigenstates

$$n_{ref}(x) = \sum_{i=1}^{N} |\phi_i|^2 \tag{5.8}$$

to get the reference density of the system.

The fragment properties are found by inverting the reference density. Using the fixed N_α inversion described in Sec. 4.1 we find fragment densities and the embedding potential that corresponds to the chosen N_α. This embedding potential is not necessarily v_p, as the fragment occupations may not be optimized to the values that fully minimize the energy and we might not get the well-localized densities that are characteristic of P-DFT calculations. Examples of this are shown in Figs. 5.5 and 5.7. The chosen occupation numbers are not optimized and we either see the metal fragment's density delocalize to the atomic region when N_{atom} is too small or the atom fragment's density delocalizes to the metallic region when N_{atom} is too large.

5.3 Infinite Metal Surface

To properly study systems characterized by the chemical potential μ instead of by the total number of electrons N, we use a model of an infinite metal surface. The previous section was a useful starting point to show the behavior of v_p at the interface between a metal and atom. To truly have a semi-infinite system, the metal

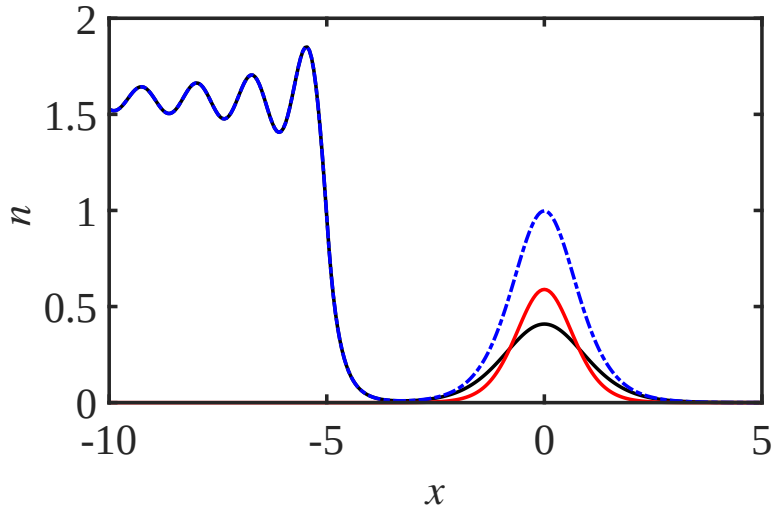

Figure 5.5. The reference density (blue dashed line) and fragment densities n_{atom} (red line) and n_{metal} (black line) for a finite fixed N_α system with $N_{atom} = 1$ and $N_{metal} = 41$. The occupation number of the atom is too low causing the fragment density of the metal to delocalize.

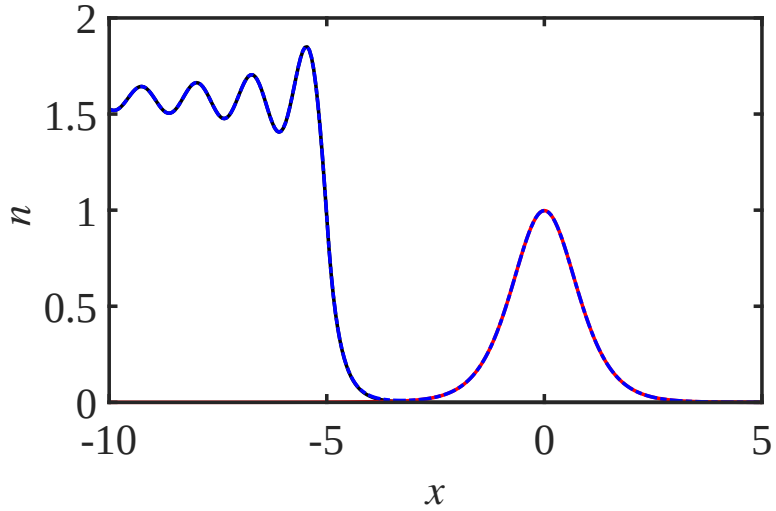

Figure 5.6. The reference density (blue dashed line) and fragment densities n_{atom} (red line) and n_{metal} (black line) for a finite fixed N_α system with $N_{atom} = 2$ and $N_{metal} = 40$. The occupation number of the atom is close to the optimized value and thus the fragment densities are localized to their region.

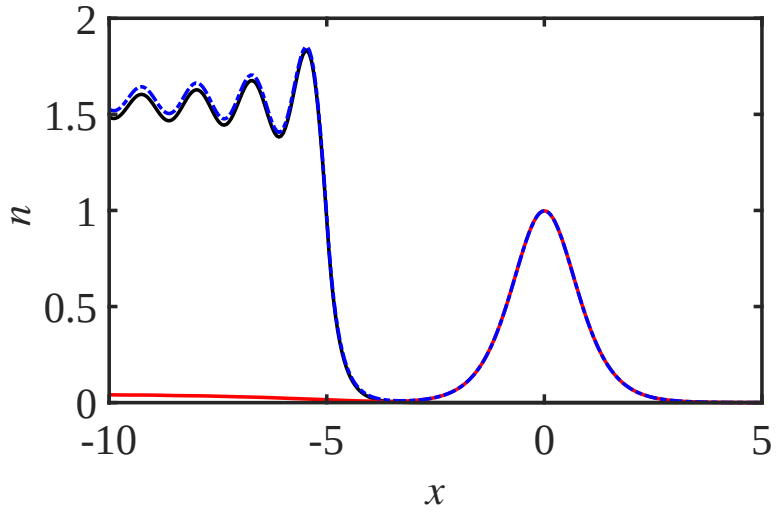

Figure 5.7. The reference density (blue dashed line) and fragment densities n_{atom} (red line) and n_{metal} (black line) for a finite fixed N_α system with $N_{atom} = 3$ and $N_{metal} = 39$. The occupation number of the atom is too high causing the fragment density of the atom to delocalize into the metallic region.

must extend from the surface to infinity. Our original method of diagonalizing the matrix Hamiltonian is no longer a viable option, thus we use different methods for the density calculations and inversion.

To increase accuracy when using a finite spatial grid and finite differences we replace the Heaviside step function with a logistic function such that

$$v_{metal}(x) = -\frac{V_0}{1 + e^{s(x-d)}}. \tag{5.9}$$

The atom is still represented by a Pöschl-Teller potential but with an additional parameter β which helps control the width of the well and the number of bound states on the atom:

$$v_{atom}(x) = -Z \cosh^{-2}(\beta x). \tag{5.10}$$

All semi-infinite results use the parameters $V_0 = 3.5$, $s = 5$, $Z = 2$, and $\beta = 0.5$. The atomic potential, with this choice of Z and β, has three bound states when isolated [75]. The fragment potentials and external potential for $d = 5$ can be seen in Fig. 5.9.

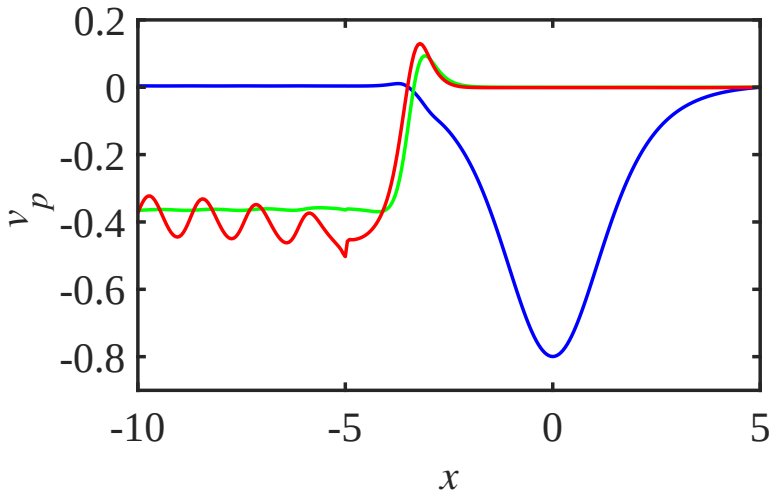

Figure 5.8. The embedding potentials "v_p's" which produce the fragment densities for the fixed N_α systems shown in Figs. 5.5 (blue line), 5.6 (green line), and 5.7 (red line). In the case where N_{atom} is too small, we get a large well in the atomic region that has a similar shape as the atom fragment potential. This feature acts to delocalize the metal fragment density towards the atom, making up for the density deficit by the atom. When N_{atom} is too large, there is a step which is reminiscent of the metal fragment potential which acts to draw the atom fragment density towards the metallic region. This makes up for the missing density and occupation of the metal fragment.

5.3.1 Density Calculations

We employ two different methods for our density calculations due to the various system types we have: (semi)infinite and finite. The full system (semi-infinite) and the metal fragment (infinite) are characterized by the chemical potential of the system, μ. The atomic fragment (finite) is characterized by its occupation number, N_{atom}. For the atomic fragment, a bound state method to calculate eigenvectors and eigenvalues of the system is all that is needed. For all densities using v_{metal}, there is a continuum of states so an eigenvalue solver is not an ideal method to calculate the densities. For these (semi)infinite systems, a Green's function method is employed instead.

All calculations are done on a spatial grid with equal spacing, dx, between points. The system is set up such that the wavefunctions ψ are defined at the values x_1, x_2,

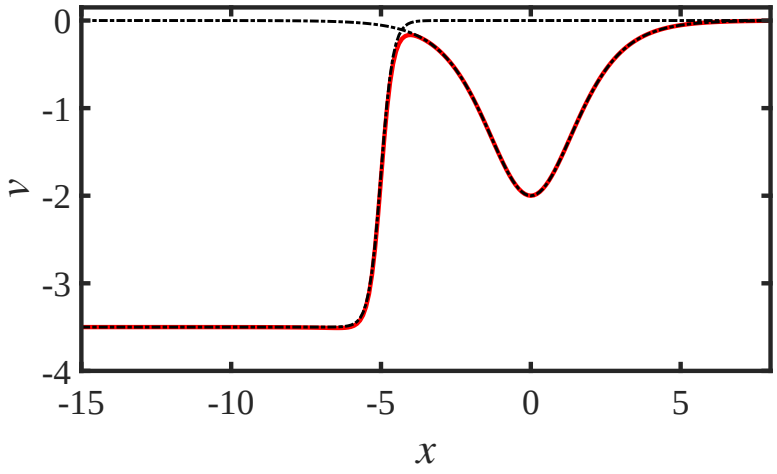

Figure 5.9. The fragment potentials given in Eqs. 5.9 and 5.10 (dash-dot black lines) along with the total external potential (red line) for the semi-infinite system when $d = 5$.

etc. while the spatial derivatives of each wavefunction ψ' are defined at $x_{\frac{1}{2}}$, $x_{\frac{1}{2}+1}$, etc. which are values between the wavefunction points:

$$x_{\frac{1}{2}} = x_1 - \frac{dx}{2},\ x_{\frac{1}{2}+1} = x_2 - \frac{dx}{2},\ .... \tag{5.11}$$

Wavefunctions for both the finite and (semi)infinite systems are found using a shooting method. By shooting from the left and the right at an energy, E, one wavefunction will satisfy the left boundary condition, ψ_L, while the other satisfies the right boundary condition, ψ_R.

Our shooting method combines the Schrödinger equation

$$2(E - v_i)\psi_i + \frac{d}{dx}\psi'_i = 0, \tag{5.12}$$

a finite difference definition of the derivative

$$\frac{\psi_{i+1} - \psi_i}{dx} - \psi'_{i+\frac{1}{2}} = 0, \tag{5.13}$$

and boundary conditions for the left-hand side and right-hand side of the system

$$\begin{aligned} \psi_1 &= 1; \qquad \psi'_{\frac{1}{2}} = (1 - e^{ik_L dx})/dx \\ \psi_{end} &= 1; \qquad \psi'_{end+\frac{1}{2}} = (e^{ik_R dx} - 1)/dx \end{aligned} \tag{5.14}$$

into one matrix equation. Here the k_L and k_R are defined as:

$$k_{L(R)} = \cos^{-1}(1 - (E - v_{L(R)})dx^2)/dx \tag{5.15}$$

where v_L is the potential at the left boundary and similarly v_R is the potential at the right boundary. This equation for k comes from knowing $\psi'_{i-\frac{1}{2}} \approx ik\psi_i$, so we can make the informed guess that $\psi_{i+1} = e^{ikdx}\psi_i$. Using this to define the wavefunction's derivatives as a finite difference:

$$\begin{aligned} \psi'_{i+\frac{1}{2}}dx &= (e^{ikdx} - 1)\psi_i \\ \psi'_{i-\frac{1}{2}}dx &= (1 - e^{-ikdx})\psi_i \end{aligned} \tag{5.16}$$

We combine these to define the derivative in 5.12. Solving for k, we arrive at Eq. 5.15. When used, we choose the k_L or k_R which has a negative imaginary part.

Infinite System

The density calculations for the (semi)infinite systems use a Green's function method inspired by Ref. [76]. A simple derivation of this method is shown in Appendix B. The density of the system is an integral in the complex energy plane:

$$n(x) = \frac{1}{2\pi i}\int_{C_\mu} G_E(x,\xi)dE. \tag{5.17}$$

Here, $G_E(x,\xi)$ is the Green's function at energy E using the representation

$$G_E(x,\xi) = \frac{\psi_L(x_<)\psi_R(x_>)}{W(\psi_R,\psi_L)} \tag{5.18}$$

where $x_< = min(x,\xi)$ and $x_> = max(x,\xi)$, $\psi_L(x)$ and $\psi_R(x)$ are solutions to the Schrödinger equation at energy E satisfying either the boundary conditions on the left or right, respectively, and $W(\psi_R,\psi_L)$ is the Wronskian

$$W(\psi_R,\psi_L) = \psi_L(x)\psi'_R(x) - \psi'_L(x)\psi_R(x). \tag{5.19}$$

The integral in Eq. 5.17 is evaluated over C_μ, a contour in the complex energy plane containing all possible occupied states, as shown in Fig. 5.10. This integral extends

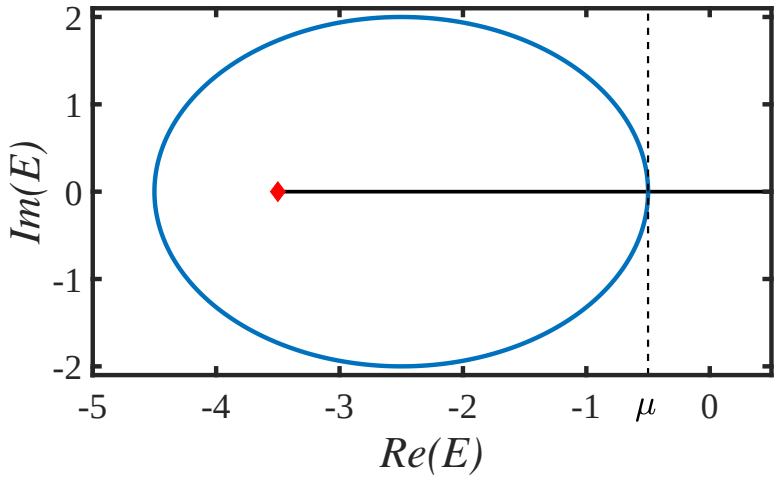

Figure 5.10. The complex contour C_μ (solid blue line) defined in Eq. 5.17 extends one Hartree below the lowest value of our external potential (red diamond) up to the chosen value of μ. In this example $\mu = -0.5$. The black line is the possible energies of our semi-infinite system.

below the minimum of the external potential up to the chemical potential of the system.

The reference density is found using this method on the total external potential. A few examples of n_{ref} at $d = 15$ for μ which result in integer occupations on the atomic fragment are shown in Fig. 5.11. The lowest μ has no occupation on the atom ($N_{atom} = 0$) and there is only density in the metal region. As μ increases, the density in the atomic region jumps up through integer values of N_{atom} at this large separation. The metallic density has increasing oscillations as it nears the surface and then smoothly drops off as it passes through the step. The amplitudes of these oscillations near the surface decrease as we increase μ and as the surface moves closer to the atomic density.

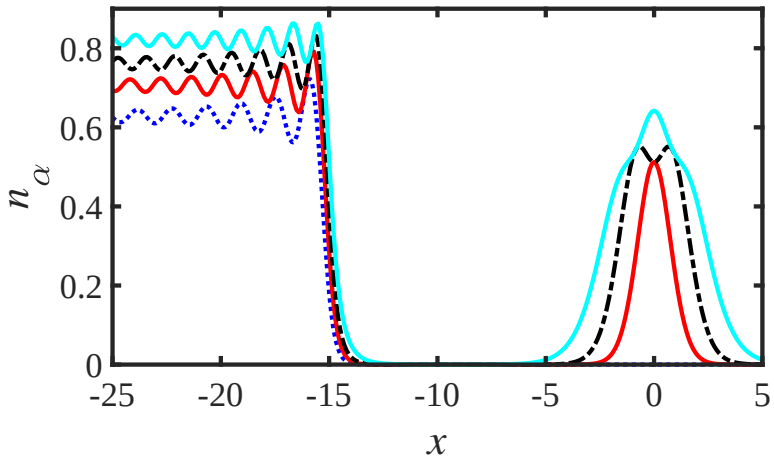

Figure 5.11. Reference densities for choices of μ which correspond to the occupations $N_{atom} = 0$ (dotted blue line), $N_{atom} = 1$ (red line), $N_{atom} = 2$ (dash-dot black line), and $N_{atom} = 3$ (cyan line) at $d = 15$.

Finite System

The finite system (atomic fragment) has a finite number of states. Here the system is defined by N not μ and the densities are not found using the Green's function method from the previous section. Instead we find the solutions from our shooting method where the Wronskian $W(\psi_R, \psi_L)$ is zero, as this occurs at energies corresponding to a bound state. To ensure we find all of the bound state eigenvalues and eigenvectors, we begin by determining the maximum number of bound states possible. We find the solutions to the Schrödinger equation which satisfy the left and right hand side boundary conditions, ψ_L and ψ_R respectively, using the shooting method described in Section 5.3.1 at an energy $E = 0$. The number of nodes in the orbitals is equal to the maximum number of bound states in the system. This is then the maximum number of occupied states for our system. We find the corresponding eigenvalues and eigenvectors by searching for energies where the Wronskian is zero.

Since our simulation doesn't force the wavefunction to go to zero at the boundaries, we must make sure to include those values beyond the boundary in our integration. We thus begin by finding the normalization factor at the right boundary

$$k_R = \frac{\cos^{-1}[1 - (E - v_R)dx^2]}{dx}, \tag{5.20}$$

making sure to take the k_R where the imaginary component is positive. Using this we calculate

$$m_R = e^{ik_R dx} \tag{5.21}$$

and

$$C_R = \frac{dx\psi_{end}^2 m_R^2}{1 - m_R^2}. \tag{5.22}$$

We do the same at the left boundary using ψ_1 instead of ψ_{end} to find k_L, m_L, and C_L. The whole normalization factor is then

$$C = \sum_i (\psi_i^2)dx + C_R + C_L. \tag{5.23}$$

After normalizing, the density is calculated as an ensemble, using any fractional occupation numbers as described in Eq. 3.4.

5.3.2 Fragment Properties and Partition Potentials

After finding n_{ref} we use the inversion method from Sec. 4.2 to calculate fragment properties and v_p.

At large separations the system behaves in a discontinuous manner. As we increase μ the atomic density jumps abruptly through integer occupations, only producing values of 0, 1, 2, and 3 for N_{atom}. In Fig.'s 5.12-5.14 we show examples of fragment densities at $d = 15$ for $N_{atom} = 0$, 1, 2, and 3. In each case, the metallic fragment density increases and the oscillations change in the same manner as the reference density, but n_{atom} does not increase smoothly with the changing μ. This follows the expected behavior of an atom interacting with a reservoir at large or infinite separations [18].

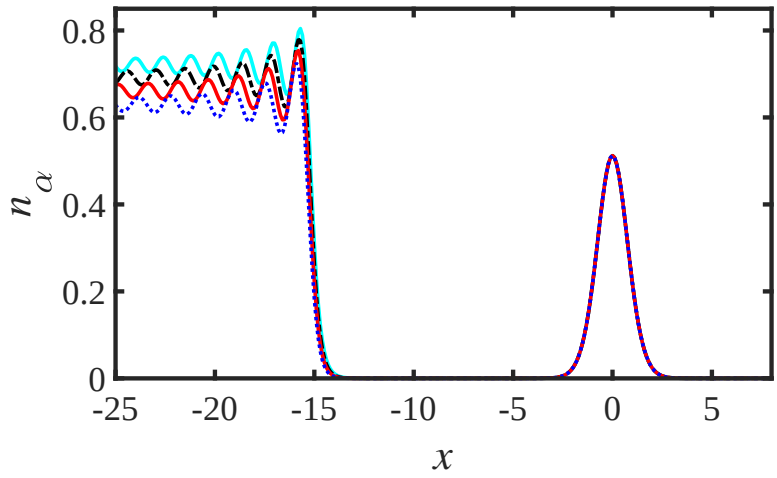

Figure 5.12. Shown are fragment densities for $d = 15$ at multiple values of μ which result in the same occupation number $N_{atom} = 1$. The curves of n_{metal} and n_{atom} are plotted separately but in the same color for each of the chemical potentials $\mu = -1.55$ (dotted blue line), $\mu = -1.35$ (red line), $\mu = -1.15$ (dashed black line), and $\mu = -0.95$ (cyan line).

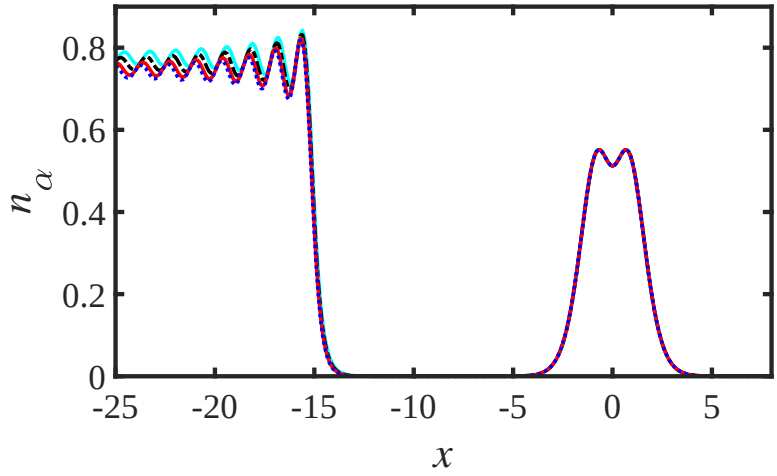

Figure 5.13. Fragment densities when $d = 15$ for μ which produce $N_{atom} = 2$. The curves of n_{metal} and n_{atom} are plotted separately but in the same color for each of the chemical potentials $\mu = -0.8$ (dotted blue line), $\mu = -0.75$ (red line), $\mu = -0.65$ (dashed black line), and $\mu = -0.55$ (cyan line).

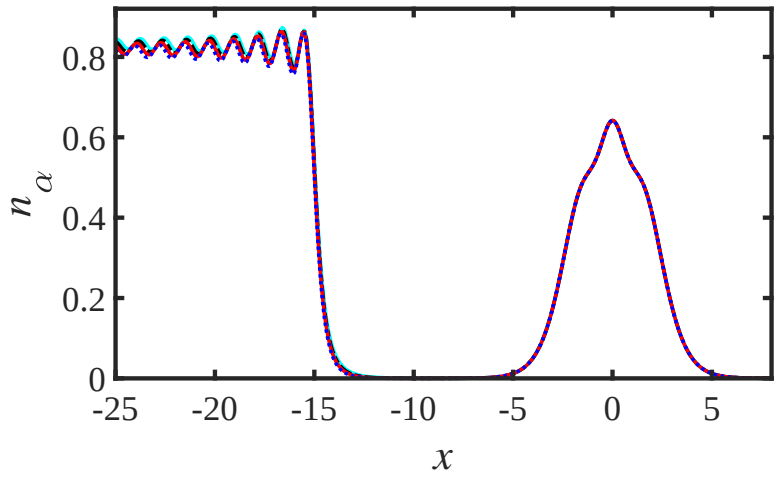

Figure 5.14. The n_α at separation $d = 15$ for values of μ which result in occupations of $N_{atom} = 3$. The curves of n_{metal} and n_{atom} are plotted separately but in the same color for each of the chemical potentials $\mu = -0.25$ (dotted blue line), $\mu = -0.2$ (red line), $\mu = -0.15$ (dashed black line), and $\mu = -0.1$ (cyan line).

When d is large, the two systems are not interacting strongly and thus do not differ drastically from their isolated densities. In these cases the partition potential only plays a small role in correcting fragment densities such that they sum to n_{ref}. In Fig.'s 5.15-5.17 we see the partition potentials which produce the fragment densities in Fig.'s 5.12-5.14. The magnitude of v_p is very small compared to the v_α. In all cases we see a small step down from the metal to the atom with a slight well between the fragments. This is what shifts the densities towards each other, most notably at the surface of the metal density. As μ continues to increase and the fragment densities get closer, we see the emergence of a slight barrier before this step (Fig. 5.17) which begins to slow and prevent the metal density from continuing to shift towards the atom, as it has occupied all possible bound states.

As we decrease the separation to $d = 5$ the behavior begins to change. In Fig. 5.18 we have fragment densities for μ which give values of N_{atom} between zero and one. In this case we still get an abrupt jump from zero to one and there is very little density overlap between fragments. Increasing μ through values where N_{atom}

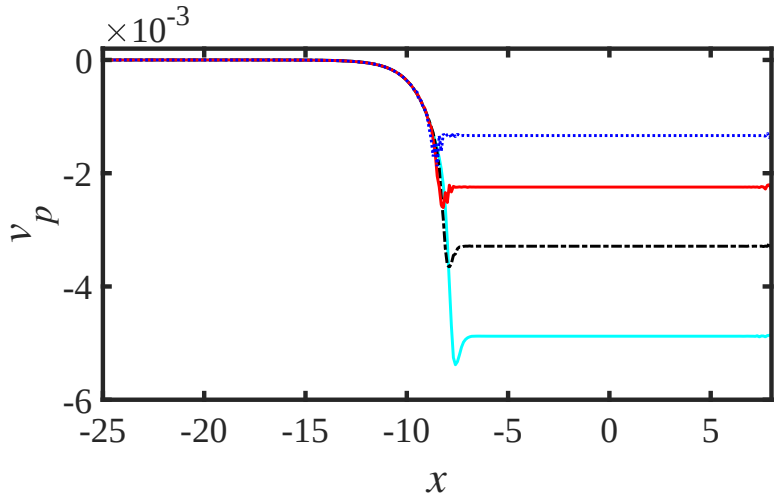

Figure 5.15. The partition potentials which produced the fragment densities in Fig. 5.12 where $d = 15$ and $N_{atom} = 1$. The color of each v_p is the same as that of the corresponding n_α for the chemical potentials: $\mu = -1.55$ (dotted blue line), $\mu = -1.35$ (red line), $\mu = -1.15$ (dashed black line), and $\mu = -0.95$ (cyan line)..

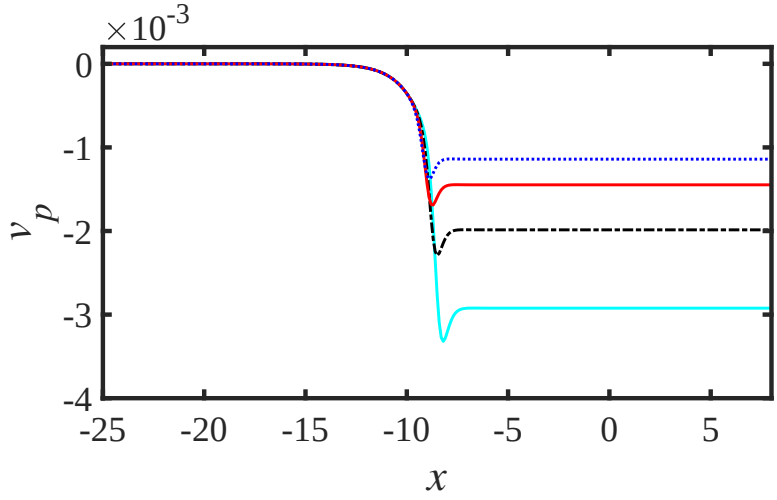

Figure 5.16. Partition potentials which produced the fragment densities in Fig. 5.13 where $d = 15$ and $N_{atom} = 2$. The color of each v_p is the same as that of the corresponding n_α for the chemical potentials: $\mu = -0.8$ (dotted blue line), $\mu = -0.75$ (red line), $\mu = -0.65$ (dashed black line), and $\mu = -0.55$ (cyan line).

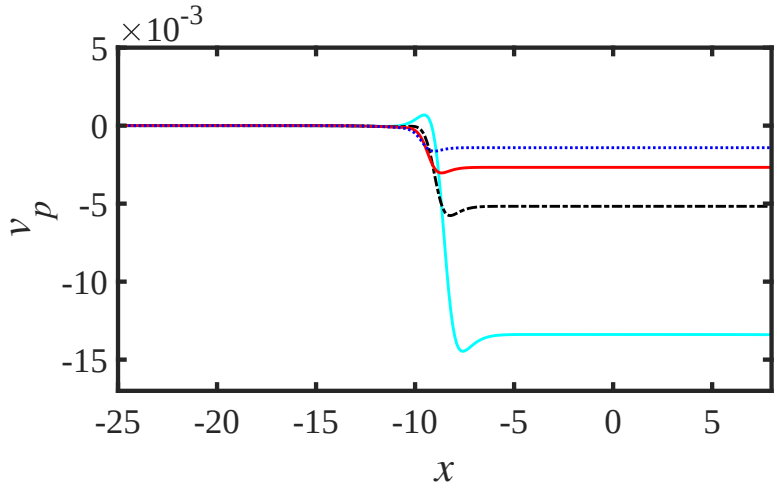

Figure 5.17. The v_p's which produced the fragment densities in Fig. 5.14 where $d = 15$ and $N_{atom} = 3$. The color of each v_p is the same as that of the corresponding n_α for the chemical potentials: $\mu = -0.25$ (dotted blue line), $\mu = -0.2$ (red line), $\mu = -0.15$ (dashed black line), and $\mu = -0.1$ (cyan line).

is between one and two, we see the transition of the density is a bit smoother, as in Fig. 5.19. There is still a large jump from just above one to just below two, but the final transition to the integer is smoother. We also begin to see more density overlap between fragments as n_{atom} starts to shift towards the metal surface. Fig. 5.20 shows the fragment densities for μ producing values of N_{atom} between two and three. Now there is a very smooth transition between the integer occupations, more density overlap, and a noticeable shift of n_{atom} towards the metal.

This changing behavior is also demonstrated in the v_p's which produce these fragment densities. In the lower μ states where $N_{atom} = 0$, as in Fig. 5.21, the partition potential's sole purpose is to shift the metal surface density towards the atom. Once the atom gains an electron however, v_p must also work to properly localize the atomic fragment density to its region. To do this, the well in v_p must decrease and shift back towards the metal. A slight barrier between the atom center and the well also helps to maintain our well-localized fragment densities. In Fig. 5.22 we increase N_{atom} through the next integer and see these same basic features, but more begin to emerge

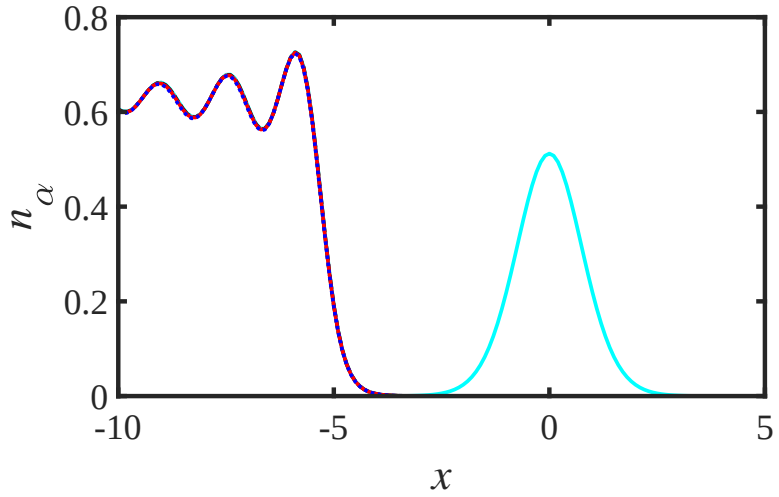

Figure 5.18. Shown are fragment densities for $d = 5$ at μ which result in values of N_{atom} between zero and one. The curves of n_{metal} and n_{atom} are plotted separately but in the same color for each of the chemical potentials $\mu = -1.575$ (dotted blue line), $\mu = -1.565$ (red line), $\mu = -1.56$ (dashed black line), and $\mu = -1.55$ (cyan line).

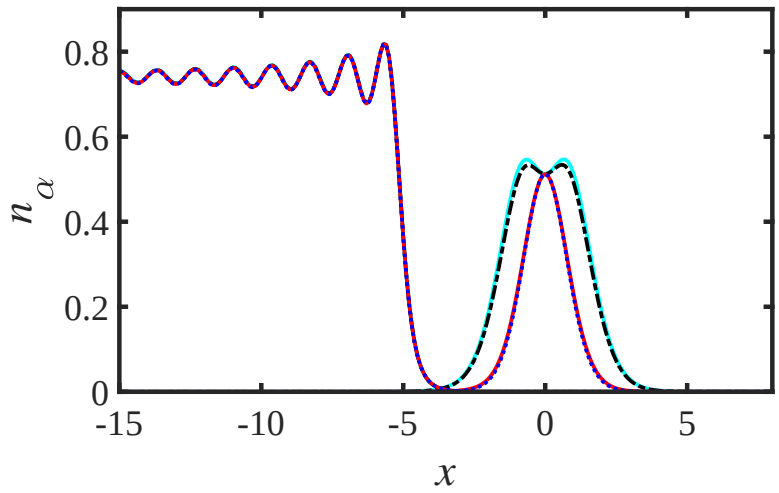

Figure 5.19. Fragment densities when $d = 5$ for μ which produce values of N_{atom} between one and two. The curves of n_{metal} and n_{atom} are plotted separately but in the same color for each of the chemical potentials $\mu = -0.81$ (dotted blue line), $\mu = -0.805$ (red line), $\mu = -0.8$ (dashed black line), and $\mu = -0.795$ (cyan line).

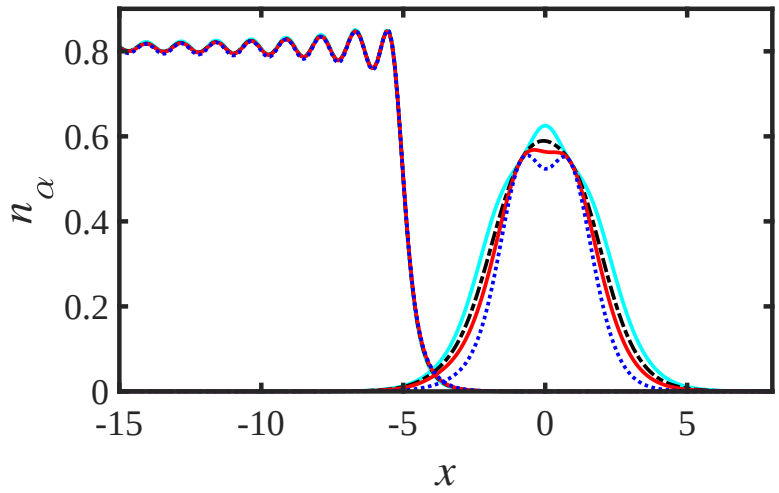

Figure 5.20. The n_α at separation $d = 5$ for values of μ which result in occupations N_{atom} between two and three. The curves of n_{metal} and n_{atom} are plotted separately but in the same color for each of the chemical potentials $\mu = -0.31$ (dotted blue line), $\mu = -0.29$ (red line), $\mu = -0.285$ (dashed black line), and $\mu = -0.27$ (cyan line).

as well. As the atomic fragment occupation starts the transition from one integer to the next, a large barrier appears in v_p on its right which shifts the fragment density towards the metal, but disappears as N_{atom} continues the transition. While finishing the transition, the fragment densities are beginning to overlap and oscillations appear in v_p in the metal region. Shown in Fig. 5.23 are the v_p's as the occupation increases through two to three. All of the previous features remain, even the barrier on the right of the atom as the transition begins. In the atomic region new pieces of v_p emerge: an asymmetric well which shifts n_{atom} towards the metal surface and a peak whose center shifts towards the metal as μ increases. This peak increases the spread of n_{atom} and helps further increase the density overlap of the fragments. Once N_{atom} reaches three, large barriers appear on either side of the well in v_p. At this point the bound states of the atom are fully occupied and electrons can no longer be transferred to the atom. These barriers in the partition potential enforce that restriction on n_{atom}.

As we further decrease the separation to $d = 3$, the fragment density overlap occurs at lower energies and occupation numbers, making the transition between

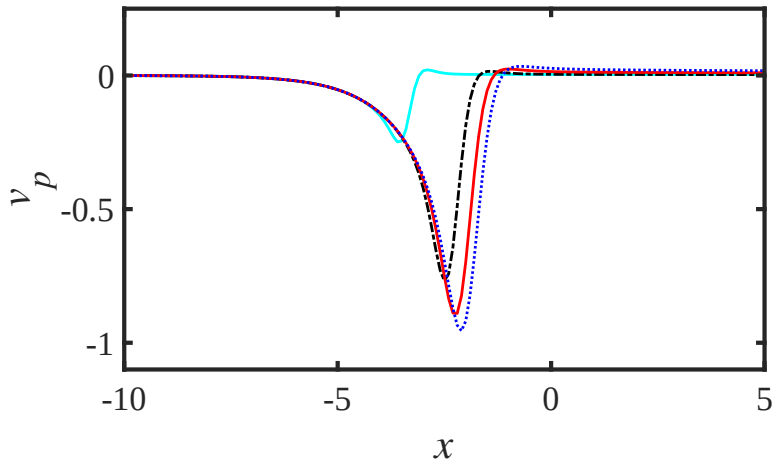

Figure 5.21. The partition potentials which produced the fragment densities in Fig. 5.18 where $d = 5$ and N_{atom} is between zero and one. The color of each v_p is the same as that of the corresponding n_α for the chemical potentials: $\mu = -1.575$ (dotted blue line), $\mu = -1.565$ (red line), $\mu = -1.56$ (dashed black line), and $\mu = -1.55$ (cyan line).

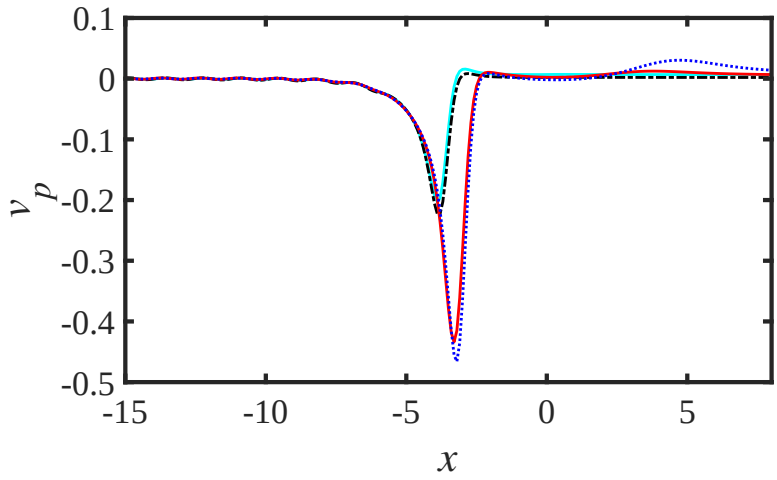

Figure 5.22. Partition potentials which produced the fragment densities in Fig. 5.19 where $d = 5$ and N_{atom} is between one and two. The color of each v_p is the same as that of the corresponding n_α for the chemical potentials: $\mu = -0.81$ (dotted blue line), $\mu = -0.805$ (red line), $\mu = -0.8$ (dashed black line), and $\mu = -0.795$ (cyan line).

integers even smoother. In Fig. 5.24 we see the fragment densities for values of μ producing occupations N_{atom} between zero and one. The transition up to one is

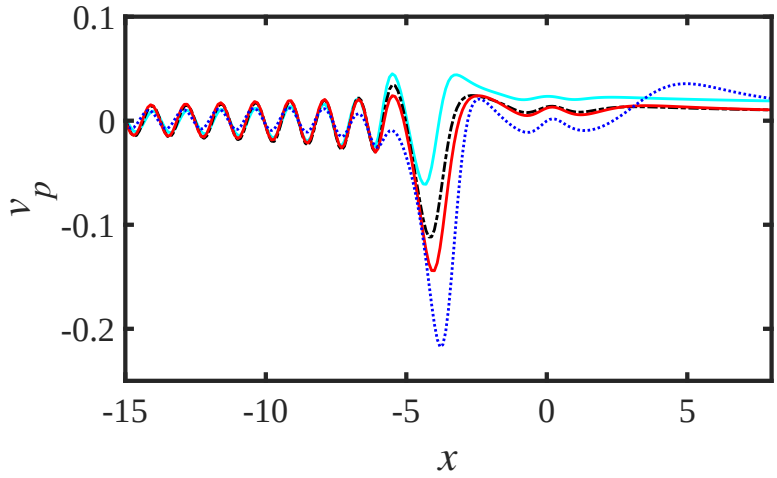

Figure 5.23. The v_p's which produced the fragment densities in Fig. 5.20 where $d = 5$ and N_{atom} is between two and three. The color of each v_p is the same as that of the corresponding n_α for the chemical potentials: $\mu = -0.31$ (dotted blue line), $\mu = -0.29$ (red line), $\mu = -0.285$ (dashed black line), and $\mu = -0.27$ (cyan line).

not abrupt like the previous cases, instead slowly and consistently increasing as we change μ. At higher μ, which produce N_{atom} between one and two, we see the fragment densities (Fig. 5.25) smoothly transitioning between the single peaked behavior of $N_{atom} = 1$ to the double peaks of $N_{atom} = 2$. These atomic fragment densities n_{atom} are very asymmetric with a portion of the bulk density shifted towards the metal surface, while still remaining centered at $x = 0$. At the integer $N_{atom} = 2$, the peak in n_{atom} that is closer to the metal is taller than the right peak, but during the change from $N_{atom} = 1$ to $N_{atom} = 2$ the opposite is true. In Fig. 5.26 we continue increasing μ such that N_{atom} is between two and three. Here there is substantial fragment density overlap which has a much stronger effect on the metal fragment density than at the lower energies. As the oscillations in the density approach the surface they no longer continuously increase as before. Instead they increase until the fragment densities overlap, then the oscillations decrease due to that overlap which corresponds to sharing of electrons between fragments. The atomic fragment densities continue to smoothly transition between the integer values of N_{atom}, from the double peaked

behavior of $N_{atom} = 2$ to the addition of a larger peak in the center when $N_{atom} = 3$. The asymmetry at these occupations is more pronounced due to the electron sharing and subsequent density overlap. As N_{atom} approaches three, n_{atom} increases in width, with a larger spread going away from the metal surface.

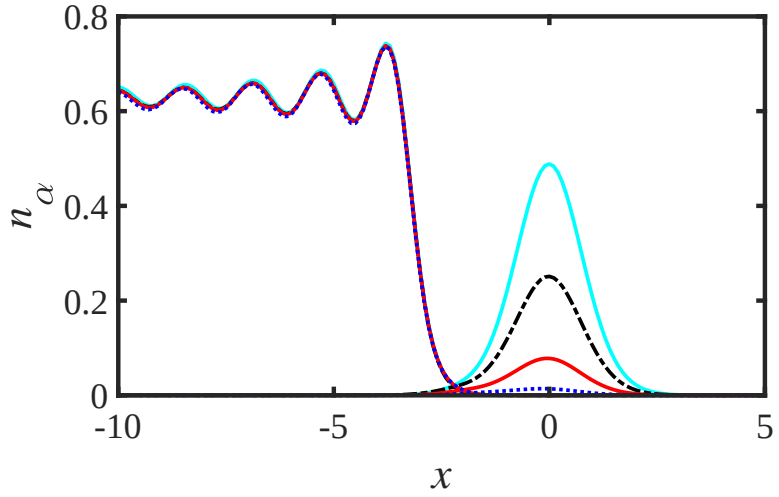

Figure 5.24. Shown are fragment densities for $d = 3$ at μ which result in values of N_{atom} between zero and one. The curves of n_{metal} and n_{atom} are plotted separately but in the same color for each of the chemical potentials $\mu = -1.585$ (dotted blue line), $\mu = -1.565$ (red line), $\mu = -1.56$ (dashed black line), and $\mu = -1.535$ (cyan line).

The partition potentials which produce these fragment densities have increasingly complex features as we increase μ. At the lower energies when N_{atom} goes from zero to one, the v_p's shown in Fig. 5.27 have the characteristic wells that we see in all of our v_p's which draw the fragment densities towards each other. As the occupation increases towards one the step up in v_p increases as well to equalize the fragment chemical potentials, but then drops as it reaches the integer value where the μ_α do not equalize. Between the well and step features we also have a barrier which increases in height as our occupation increases. This prevents the atomic fragment density from spreading too wide while the μ_α equalization occurs. Unlike the large separations, we also begin to get oscillations in the metal region at these very low occupation numbers. These oscillations are the result of the density overlap which occurs at very low μ

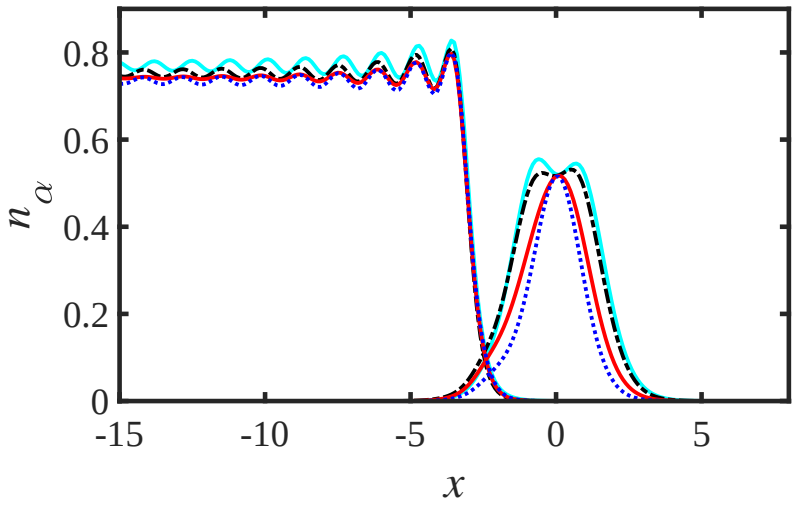

Figure 5.25. Fragment densities when $d = 3$ for μ which produce values of N_{atom} between one and two. The curves of n_{metal} and n_{atom} are plotted separately but in the same color for each of the chemical potentials $\mu = -0.845$ (dotted blue line), $\mu = -0.795$ (red line), $\mu = -0.72$ (dashed black line), and $\mu = -0.595$ (cyan line).

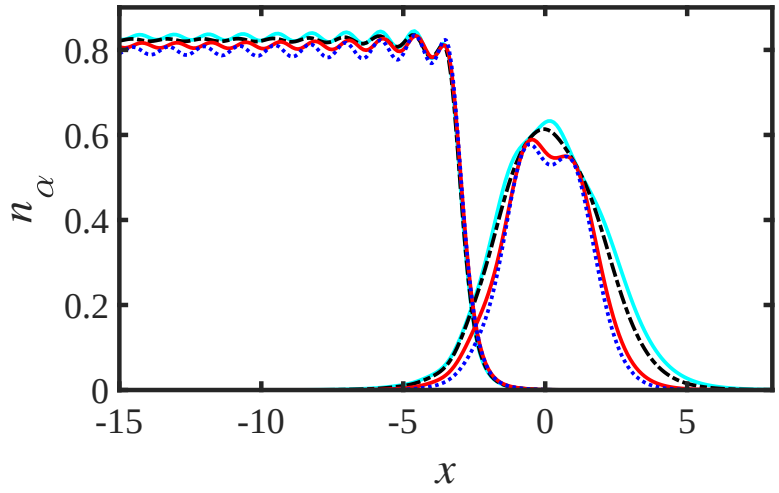

Figure 5.26. The n_α at separation $d = 3$ for values of μ which result in occupations N_{atom} between two and three. The curves of n_{metal} and n_{atom} are plotted separately but in the same color for each of the chemical potentials $\mu = -0.375$ (dotted blue line), $\mu = -0.275$ (red line), $\mu = -0.175$ (dashed black line), and $\mu = -0.12$ (cyan line).

when the metal surface and atom separation is small, $d = 3$. At $d = 5$ we did not begin to see these features until N_{atom} increased towards two (Fig. 5.22). In Fig. 5.28 the μ is increased to values where N_{atom} is between one and two. The oscillations in the metallic region increase dramatically as the density overlap increases. The behavior of the well, barrier, and step that we saw as N_{atom} approached one is also present in this transition towards the integer $N_{atom} = 2$, however these steps do not remain flat as they did in the lower occupations. The v_p steps up, but then decreases as it continues to the right, with a small well just left of the center of the atom. In the region where N_{atom} is between two and three, the partition potential looks very complicated, but actually still follows the same type of behavior as the other v_p's. Fig. 5.29 shows the partition potentials which produce the fragment densities from Fig. 5.26. There is a large amount of density overlap between fragments and v_p must keep the fragment densities well localized, which is one of the defining characteristics of P-DFT. As we saw in previous cases of large density overlap, the oscillations in the metallic region near the surface increases with the overlap. Here there is extensive density overlap, thus we see the largest oscillations yet. These oscillations begin to merge with the well in v_p between the fragments. For the atomic fragment densities in Fig. 5.26 which still had the double peaked behavior (the lowest two values of μ), the well in v_p still extends lower than any other features in v_p. When we increase μ, the well in v_p is still present, but is no longer the deepest well in v_p. In these partition potentials we still have the step in v_p up or down from the metal to atom region, but, as in the case of $N_{atom} = 1 - 2$, we have other features added to that region along with a non-constant behavior to the right of the step. In addition to the well just to the left of the center of the atomic potential, we have a wider well to the right with a peak in between which is not centered on the atom. This combination of wells and peaks are what increase the spread of n_{atom} as the atom strongly interacts with the metal surface in the reference system. The asymmetry of n_{atom} is reflected in the different well depths and widths between the left and right side of the peak. At the far right side of v_p for the lowest two μ, there is a barrier or step up such that our n_{atom}

doesn't spread too far from the metal as it begins to occupy the third orbital. At the higher μ, n_{ref} spreads further to the right, and as such, v_p drops off as in Fig. 5.28 instead of stepping up. This is more pronounced at these very small separations, but was also seen when $d = 5$ in Fig. 5.23. This well and lowering step are the cause of the asymmetric spreading of the atomic fragment density. The increased peak height on the left side of n_{atom} is produced by the well in the step, and the lowering causes the entire right hand side of n_{atom} to spread out and away from the metal.

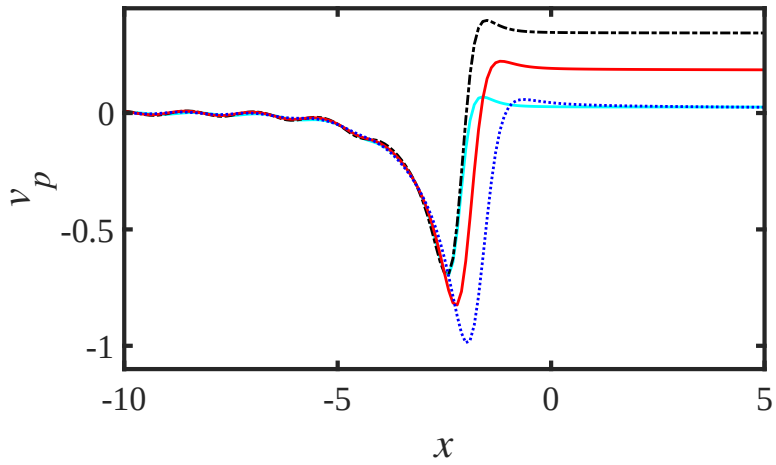

Figure 5.27. The partition potentials which produced the fragment densities in Fig. 5.24 where $d = 3$ and N_{atom} is between zero and one. The color of each v_p is the same as that of the corresponding n_α for the chemical potentials: $\mu = -1.585$ (dotted blue line), $\mu = -1.565$ (red line), $\mu = -1.56$ (dashed black line), and $\mu = -1.535$ (cyan line).

Even in this case where the partition potential has a large number of features, we still see the same types of behavior as the simpler v_p's. There is a well between the metal and atom drawing the densities together which makes up for the lack of interaction between fragments. The step from the metal up or down towards the atom optimizes the occupation number of the atom by either equalizing the μ_α or, at integer N_{atom}, reflecting the differences between μ_α while ensuring the constraint in Eq. 4.2 is met. As density overlap increases, growing oscillations occur near the metal surface which causes the decline of oscillations in n_{metal} as it approaches the

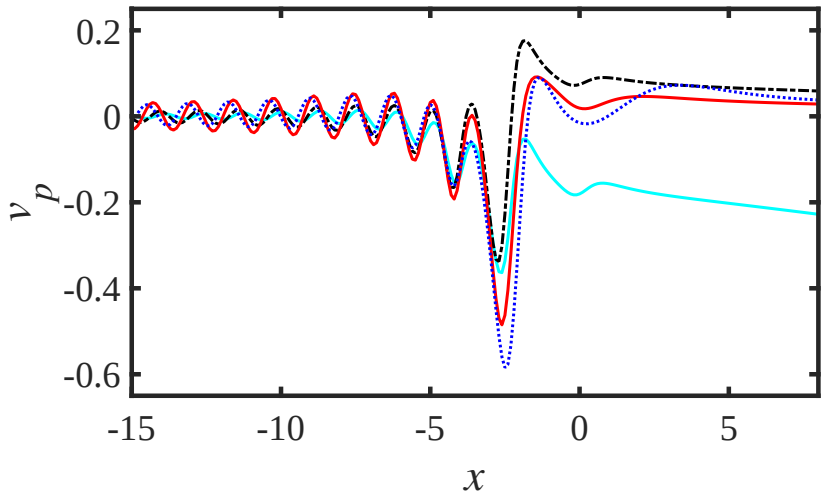

Figure 5.28. Partition potentials which produced the fragment densities in Fig. 5.25 where $d = 3$ and N_{atom} is between one and two. The color of each v_p is the same as that of the corresponding n_α for the chemical potentials: $\mu = -0.845$ (dotted blue line), $\mu = -0.795$ (red line), $\mu = -0.72$ (dashed black line), and $\mu = -0.595$ (cyan line).

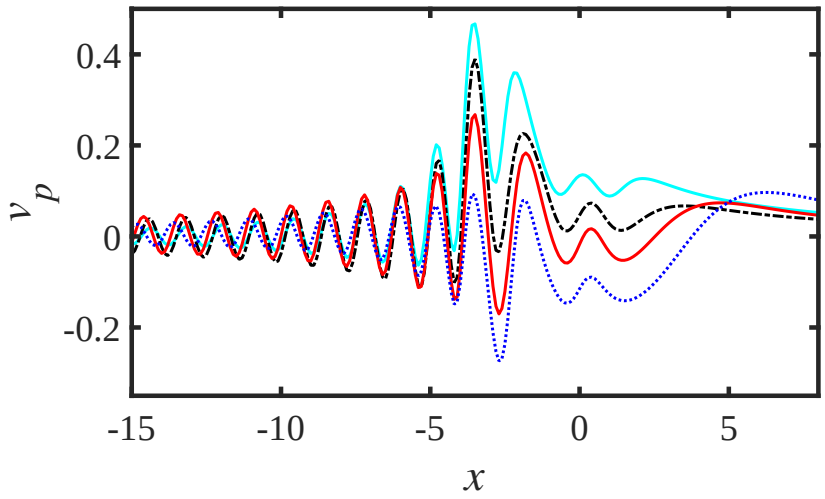

Figure 5.29. The v_p's which produced the fragment densities in Fig. 5.26 where $d = 3$ and N_{atom} is between two and three. The color of each v_p is the same as that of the corresponding n_α for the chemical potentials: $\mu = -0.375$ (dotted blue line), $\mu = -0.275$ (red line), $\mu = -0.175$ (dashed black line), and $\mu = -0.12$ (cyan line).

surface. The peaks of the oscillations in v_p are located at the peaks of the oscillations in n_{metal}, resulting in their decreased amplitude. There are also varying combinations of different sized peaks and wells which all work to spread n_{atom} away from the center of the atom while keeping it well localized.

5.4 Smoothing of μ vs N

The ensemble definition of properties used in P-DFT is what allows for fractional fragment occupation numbers. This leads to well localized fragment densities and allows us study charge transfer in systems. It is known that for an atom allowed to exchange electrons with a distant reservoir the behavior of μ vs N is a series of flat lines which step up discontinuously at integer N [18]. It has been hoped that by decreasing the separation to finite distances, this step-like function would smooth out and potentially get rid of any discontinuous behavior in μ vs N such that μ is well defined for all values of N. It is known that for finite temperatures the cusps at integer N become rounded, but it has also been supposed that the same behavior occurs with finite distances at $0K$ [22]. With P-DFT we have finally been able to study the behavior as d decreases and have shown this smoothing that had been hoped for. In Fig. 5.30 we show how N vs μ behaves when we are at large separations $d = 15$, which behaves like $d \to \infty$, and the finite separations $d = 5$ and $d = 3$. When $d = 15$ we get the steps expected of a system at large or infinite separations. At these separations μ is not well defined at each integer value of N_{atom}, as many μ produce the same N_{atom}. Decreasing to $d = 5$, we still see the steps at low occupation numbers where there is not substantial density overlap. As μ increases, and thus N_{atom} increases, we get overlapping fragment densities. The steps begin to smooth and the regions where μ is not well defined shrink. At very small separations $d = 3$, this smoothing occurs at the very low μ and becomes even less step-like as μ increases. Here, it looks like we may have eliminated the regions where μ is not well defined at integer N_{atom}. In Fig. 5.31 we see this is not the case. The shaded regions

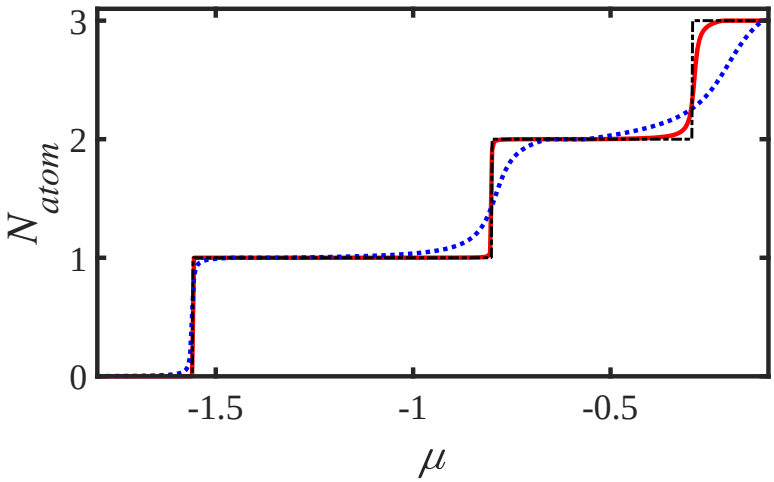

Figure 5.30. The atomic fragment occupation number N_{atom} as a function of the system μ for $d = 3$ (dotted blue line), $d = 5$ (solid red line), and $d = 15$ (dash-dot black line).

show that the integer N_{atom} region shrinks as d decreases, but does not disappear completely. Even at smaller separations like $d = 2$ we still get regions where μ is not well defined.

This lack of full smoothing is partially explained by looking at the atomic fragment eigenvalues, as the chemical potential of the atom is simply the HOMO eigenvalue. In Fig. 5.32 we see the lowest three atomic fragment eigenvalues for $d = 3$. The eigenvalues have shifted towards each other but there is still a jump from the first to the second at $N = 2$ and from the second to the third at $N = 3$. These jumps result in regions where μ_{atom} is not able to equalize to the system μ which occurs in the regions of integer N_{atom} seen in Fig. 5.31. At separations below $d = 3$, these jumps decrease but still remain, as do the regions of integer N_{atom}. This deformation of the energy levels as they attempt to align with the Fermi level, or chemical potential, has been demonstrated in other calculations of realistic metal-molecule interfaces. When the energy levels of the molecule align with the Fermi level it is an indication of strong charge transfer between the systems [65, 73]. Our system has chemical potential equalization when the atom has a non-integer charge, which is a region of

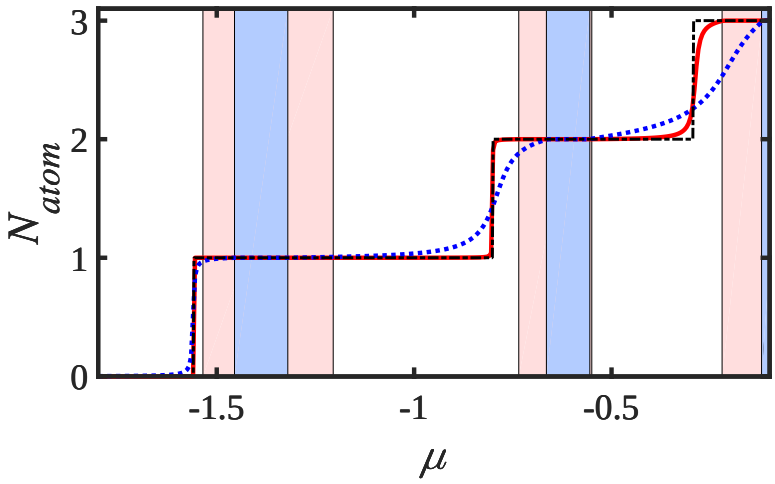

Figure 5.31. The atomic fragment occupation number N_{atom} as a function of the system μ for $d = 3$ (dotted blue line), $d = 5$ (solid red line), and $d = 15$ (dash-dot black line). The shaded areas show the regions where N_{atom} is an integer for $d = 5$ (light red) and $d = 3$ (blue). The step-like behavior smooths as the separation decreases and as N_{atom} increases due to the increased density overlap between fragments.

strong charge transfer. Those realistic system calculations also demonstrated that in the cases where the energy levels do not align, there is not significant charge transfer, as seen in our case of integer N_{atom}.

5.5 Features of v_p and Analogy to v_s

As mentioned in Sec. 3, P-DFT's method of using non-interacting fragments is somewhat analogous to KS-DFT's method of using non-interacting electrons. In KS-DFT the missing interactions are encoded in v_s, while in P-DFT the interactions are recreated through v_p. Therefore, it is not surprising that we see some of the same features in v_p as seen in the exact v_s for similar systems.

When there are singularities in the external potential, there is a singularity in v_s at the location of each singularity in v_{ext} [22]. In v_p we also see these singularities appear, which result in cusps in the fragment densities at the location of these singularities

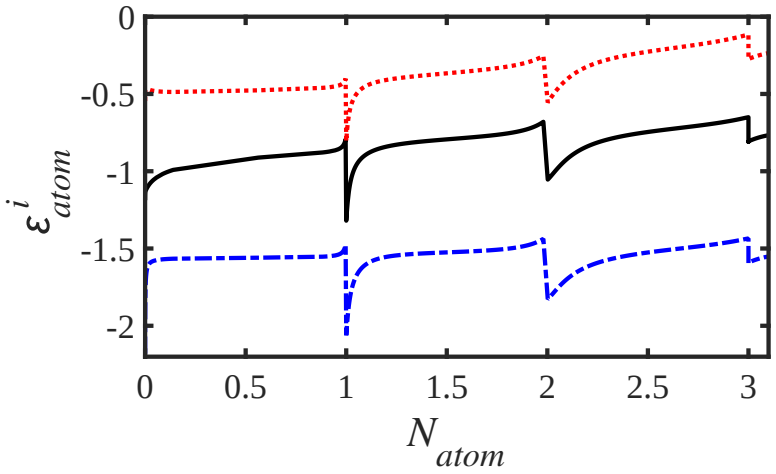

Figure 5.32. The atomic fragment eigenvalues ε^i_{atom} as the fragment occupation N_{atom} increases for $d = 3$.

[29]. For heteronuclear diatomic systems of up to two electrons, it has been shown that at finite separations a step appears in the exact v_s along with a barrier on the edge of the higher step [22, 77–79]. In our metal-atom system at finite separations, we also see these types of step and barrier features, which can easily be seen in Fig. 5.27. The well between fragments that is seen in most of our partition potentials [29], is not present in these v_s's. Instead, a barrier appears between the two nuclei [22, 77–79]. Since v_s encodes the missing electron-electron interactions, which will be repulsive, and our v_p has the missing interactions from the other fragment potentials, which will generally be an attractive interaction, this difference in features would be the natural result.

6. PERIODIC SYSTEMS

Until now P-DFT had only been done on finite systems and the question of how it should be handled for infinite or periodic systems had not been studied. Many interface and adsorption calculations using DFT methods are done with a relatively thin surface interacting with atoms or molecules in a finite space having periodic boundary conditions [80]. Studies of bulk materials and molecular chains also exploit the periodic nature of the system and use plane wave basis sets. These periodic systems benefit from the use of embedding methods [71, 72, 81–83], thus we wish to extend the scope of P-DFT to also include periodic or infinite systems.

One of the exciting aspects of using P-DFT on these periodic systems is that the fragment densities are always well localized. Other embedding methods have been used to study periodic systems but do not always result in localized densities. Therefore these approaches cannot give the same insight into charge transfer between fragments as P-DFT.

By inverting the density of atomic chains we study the behavior of the exact partition potential. The v_p gives clues as to how fragments interact with each other in the full system and, due to the well-localized fragment densities characteristic of all P-DFT calculations, also shows how electrons are shared or arranged among the fragments.

The partition potential has some interesting features that change as the fragment occupation number increases. At lower values of N_α, v_p has wells in between fragments. If we increase N_α such that all bound states of the fragments are fully occupied, this well between fragments becomes a barrier. There is a smooth transition between these well and barrier features. One might think that the well shrinks until there is a flat line and then grow into a barrier, but this is not the case. Instead, the well begins to shrink as a peak begins to emerge at the center of the well. As the

well continues to shrink, this peak grows until it replaces the well completely with a barrier. We also observe that the features of v_p (locations of wells, barriers, etc.) do not change as we vary the separation between fragments in the system, only the size of the features.

We model unit cells of an infinite, periodic atomic chain on a finite, 1-D spatial grid with uniform spacing dx. Each unit cell therefore has a finite number of wells and fragments, N_f. We choose each fragment such that it contains only one well and all wells are evenly spaced a distance d apart. The simulation box has periodic boundary conditions which wrap-around and enforce that all values at $x = 0$ equal those at $x = a$, where $a = N_f * d$. Thus our spatial grid extends from $x_{min} = 0$ to $x_{max} = a - dx$.

Two different types of potential wells will be used for our periodic systems, either delta wells or Pöschl-Teller potentials. Fragment α's potential is of the form:

$$v_\alpha(x) = -Z_\alpha \delta(x - x_{well,\alpha}) \tag{6.1}$$

or

$$v_\alpha(x) = -Z_\alpha \cosh^{-2}(\beta_\alpha[x - x_{well,\alpha}]) \tag{6.2}$$

where Z_α is the depth of that fragment's well, β_α is the parameter controlling the width of the well for fragment α, and $x_{well,\alpha} = (2\alpha - 1)\frac{d}{2}$. The way we are modeling our system, the full external potential is not simply the sum of v_α. To satisfy the wrap-around boundary conditions v_{ext} must include the fragment potentials of the neighboring cells. We define a new potential v_α^P which is the periodic version of v_α

$$v_\alpha^P(x) = v_\alpha(x) + v_\alpha(x - a) + v_\alpha(x + a), \tag{6.3}$$

and this will define the external potential

$$v_{ext}(x) = \sum_{\alpha=1}^{N_f} v_\alpha^P(x). \tag{6.4}$$

6.1 Periodic Fragment Potentials

We begin with a straightforward density calculation and inversion of a periodic chain of identical δ wells with the form from Eq. 6.1 where $Z_\alpha = 1$, $d = 2$, and $N_f = 10$. The orbitals and energy eigenvalues are found by diagonalizing a matrix Hamiltonian:

$$\frac{1}{dx^2}\begin{bmatrix} \frac{5}{4} & -\frac{2}{3} & -\frac{1}{24} & 0 & 0 & -\frac{1}{24} & -\frac{2}{3} \\ -\frac{2}{3} & \frac{5}{4} & -\frac{2}{3} & -\frac{1}{24} & 0 & 0 & -\frac{1}{24} \\ -\frac{1}{24} & -\frac{2}{3} & \frac{5}{4} & -\frac{2}{3} & -\frac{1}{24} & 0 & 0 \\ 0 & -\frac{1}{24} & -\frac{2}{3} & \frac{5}{4} & -\frac{2}{3} & -\frac{1}{24} & 0 \\ 0 & 0 & -\frac{1}{24} & -\frac{2}{3} & \frac{5}{4} & -\frac{2}{3} & -\frac{1}{24} \\ -\frac{1}{24} & 0 & 0 & -\frac{1}{24} & -\frac{2}{3} & \frac{5}{4} & -\frac{2}{3} \\ -\frac{2}{3} & -\frac{1}{24} & 0 & 0 & -\frac{1}{24} & -\frac{2}{3} & \frac{5}{4} \end{bmatrix} + v_{ext}(x) \tag{6.5}$$

where the corner elements enforce the periodic boundary conditions and the kinetic energy is written using second derivative finite difference coefficients with fourth-order accuracy.

When $N = 10$ the reference density is the sum of the lowest 10 squared orbitals

$$n_{ref}(x) = \sum_{i=1}^{10} |\phi_i(x)|^2 \tag{6.6}$$

which is shown in Fig. 6.1 along with the external potential. With the reference density in hand an inversion may be done to find v_p and the fragment properties. Since the wells are identical and evenly spaced, the fragment occupations are the same $N_\alpha = \frac{N}{N_f}$ and the fixed N_α inversion from Sec. 4.1 can be used. For the system with periodic fragment potentials the fragment densities are calculated in the same manner as n_{ref}. We diagonalize the matrix Hamiltonian from Eq. 6.5 but replace $v_{ext}(x)$ with $v_\alpha^P(x) + v_p(x)$. Notice here that the periodic version of the fragment potential v_α^P is used. This means that fragments can interact with the neighboring versions of their fragment potential if the unit cell is not large enough. There is technically not one well per fragment, but a periodic chain of wells with spacing a.

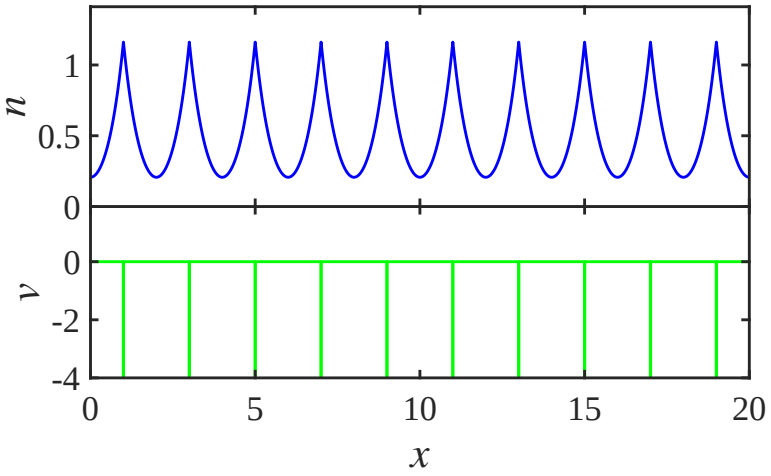

Figure 6.1. The external potential (bottom plot) for a periodic chain of 10 δ wells with $Z = 1$, $d = 2$, and $N = 10$ along with the reference density produced (top plot).

Therefore if a is too small, the fragment densities are not well-localized as they extend into the neighboring unit cells and are thus wrapped-around into their own unit cell. If the unit cell is large enough, these interactions are not strong enough to affect the results (especially with the sharply peaked densities produced by δ wells).

6.1.1 Partition Potentials and Fragment Properties

Even though these are not fully isolated fragment potentials, using δ wells within a large unit cell can very accurately reproduce the results one would get from one well per fragment. Our unit cell containing 10 identical δ wells is large enough to get close to the isolated fragment potential results. In Fig. 6.2 we show fragment densities for this chain of 10 wells when $N = 5$, such that $N_\alpha = 0.5$ and the lowest orbital in each fragment is halfway occupied. Due to the fact that the fragments are identical we only show 4 out of the 10 fragment densities. The fragment densities have a wider spread than the isolated density from a single δ well n_α^0 as seen in Fig. 6.3. The n_α also get small cusps at the center of the neighboring fragment potentials. This spreading and these cusp-like features are from the effects of the partition potential

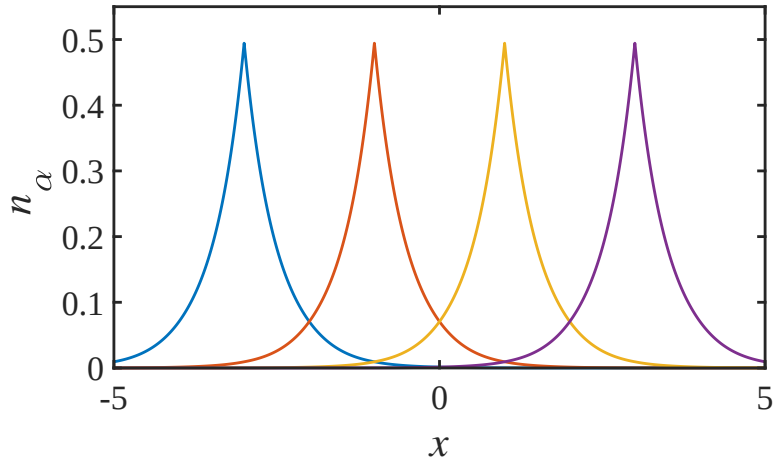

Figure 6.2. Fragment densities for a periodic system of delta wells with $N_\alpha = 0.5$, $d = 2$, and $Z = 1$. The unit cell contains 10 identical δ wells but we only show fragment properties for the 4 center wells, as the fragment densities are the same for each fragment (shifted by a multiple of d).

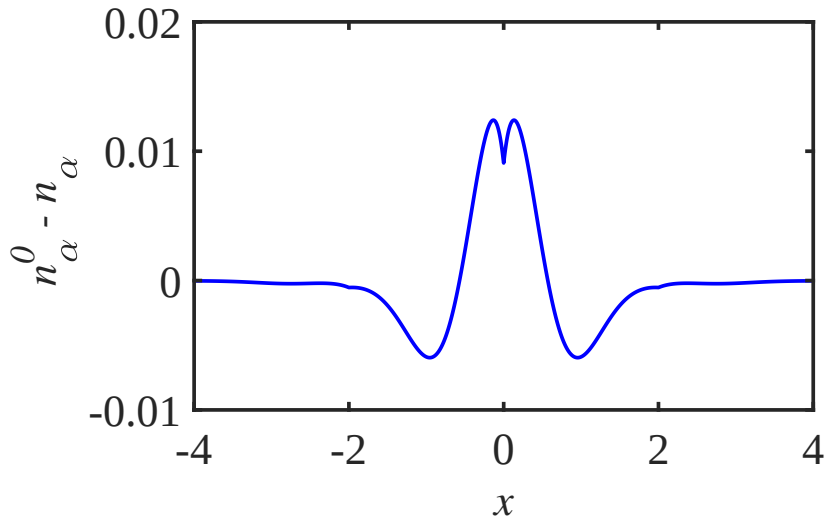

Figure 6.3. The difference between the density from an isolated delta well n^0_α and one of the fragment densities n_α shown in Fig. 6.2 where $N_\alpha = 0.5$. This shows the cusp-like features produced by the delta wells in v_p which are centered at the fragment potential and the neighboring singularities.

in Fig. 6.4. The v_p has singularities at the locations of the δ wells in the external potential which produce the cusps in n_α. There are also wells in v_p between fragments that are a common feature in all of our systems which cause the spreading of n_α.

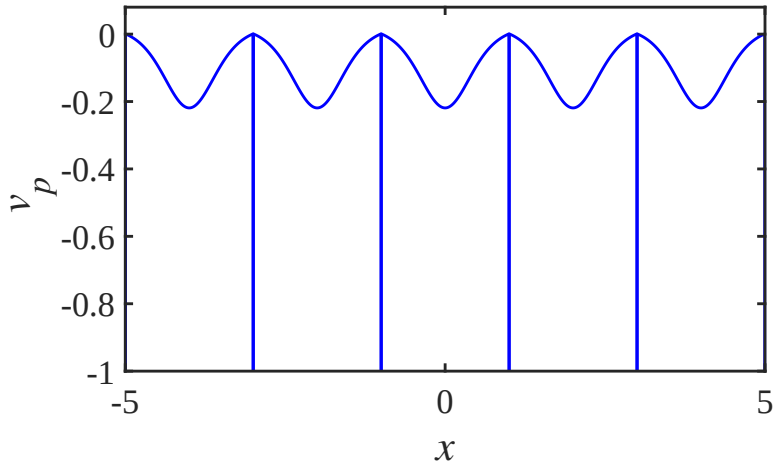

Figure 6.4. The partition potential for the periodic system of delta wells shown in Fig. 6.2 where $N_\alpha = 0.5$. Here v_p has singularities at the location of each delta well in the external potential with wells in between each fragment. The wells between fragments cause the fragment densities to have an increased spread, while still remaining well localized to the fragment center. Due to the fractional charge of each fragment there is a larger overlap of fragment densities.

If we increase the number of electrons until each fragment has a fully occupied ground state, $N = 10$ and $N_\alpha = 1$, the behavior of the fragment properties and v_p change. The fragment densities for the 4 centermost wells is shown in Fig. 6.5. The fragment densities are more sharply peaked than those in Fig. 6.2 and they do not have the spreading or large overlap of fragment densities as seen when $N_\alpha = 0.5$. This is more apparent when comparing n_α to n_α^0 (Fig. 6.6). Not only is n_α more peaked in this case than when $N_\alpha = 0.5$, but it has a sharper peak and smaller width than even the isolated fragment density. This difference in fragment properties also corresponds to a large change in the features of the partition potential. In Fig. 6.7 we still see the singularities in v_p at the locations of the δ wells in v_{ext}, but where there were once wells between fragments, we now have barriers. When $N_\alpha = 1$, the bound state

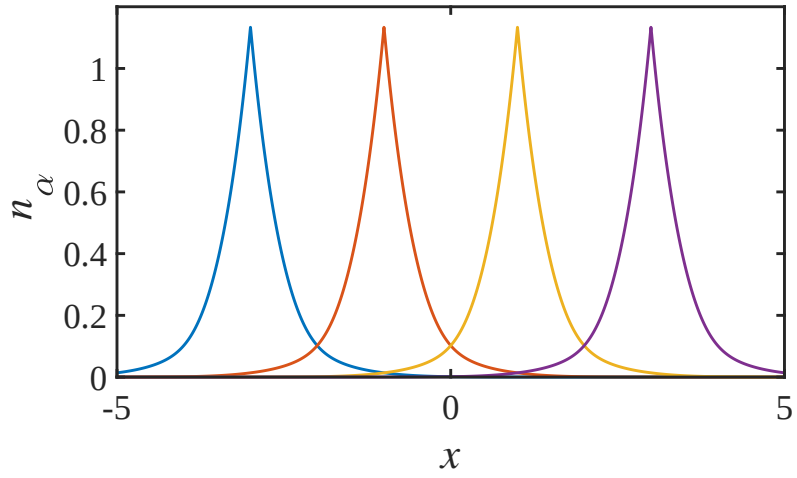

Figure 6.5. Fragment densities for a periodic system of delta wells with $N_\alpha = 1$, $d = 2$, and $Z = 1$. The unit cell contains 10 identical δ wells but we only show fragment properties for the 4 center wells, as the fragment densities are the same for each fragment (shifted by a multiple of d).

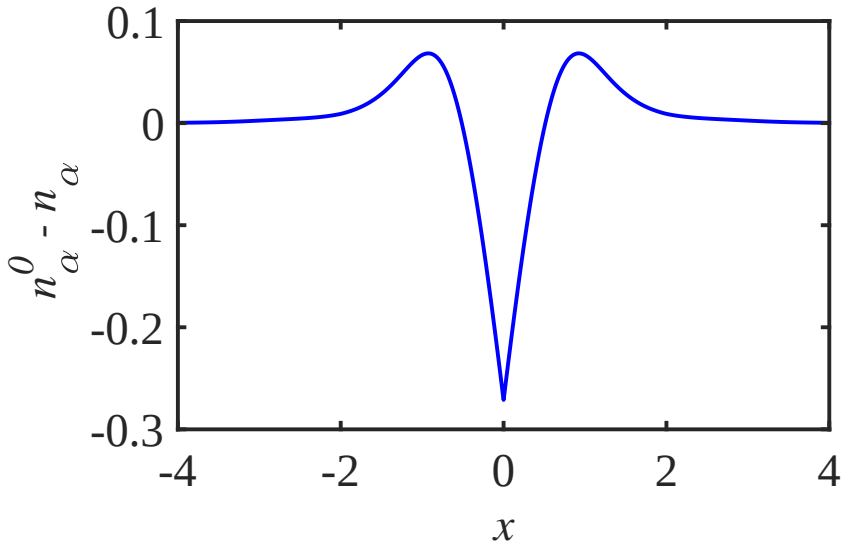

Figure 6.6. The difference between the density from an isolated delta well n^0_α and the fragment density n_α shown in Fig. 6.5 where $N_\alpha = 1$. The fragment density becomes even more peaked and compact than the isolated density.

orbitals of each fragment are fully occupied. Thus, we do not get the density overlap that is present when fragments have fractional occupations or have states which are not fully occupied. Since electrons cannot be shared or spread between fragments anymore, we get a very thin and localized fragment density. The large barriers in v_p cause this increased isolation and allow for us to recreate the reference density from Fig. 6.1.

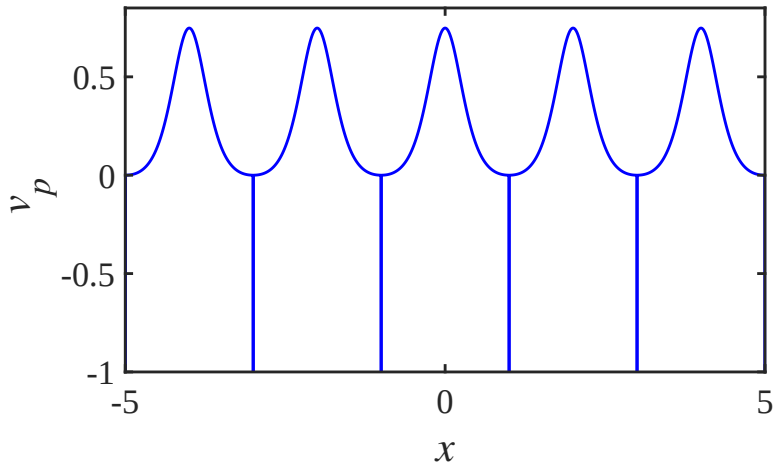

Figure 6.7. The partition potential for the periodic system of delta wells shown in Fig. 6.5 where $N_\alpha = 1$. Here v_p has singularities at the location of each delta well in the external potential with barriers between each fragment. The barriers in v_p cause fragment densities to be more strongly peaked compared to the isolated densities, seen in Fig. 6.6. Each fragment potential only has one bound state which is filled when $N_\alpha = 1$ thus we do not see the large density overlap as in Fig. 6.4.

6.1.2 Flaws in the Method

When there is an odd number of identical wells in the unit cell, summing the squared orbitals produced by the eigenvalue solver does not always give the correct reference density. For example, in a unit cell composed of three δ wells the reference densities calculated when $1 < N < 3$ are incorrect and do not have the correct periodicity. In the region where $N \leq 1$ only the first molecular orbital is used to

calculate n_{ref}. This orbital is symmetric about the center of the unit cell and is periodic not just over the unit cell a, but also between each well center d as shown in Fig. 6.8 and will produce the correct n_{ref}.

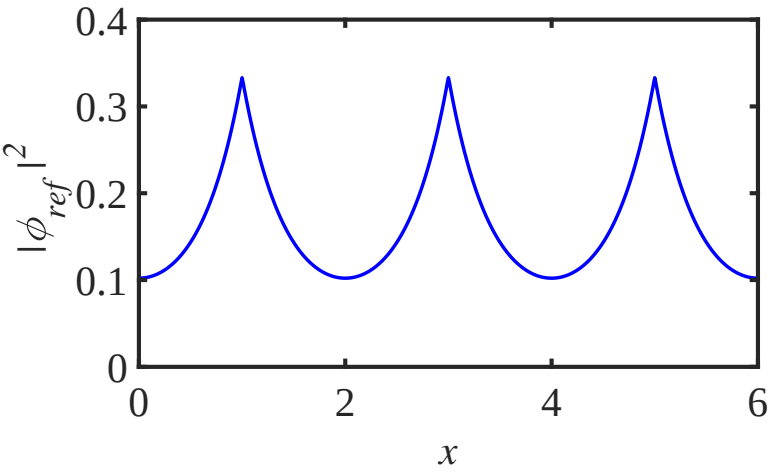

Figure 6.8. The square of the first orbital $|\phi_{ref,1}|^2$ for a unit cell containing three delta wells. This is equal to the reference density when $N = 1$.

As electrons are added and higher orbitals used, one must be careful how they use the results of the eigenvalue solver. The second orbital produced is antisymmetric about the center of the unit cell, thus it gives no contribution to the density of the center well. A reference density calculated using only the first two orbitals is shown in Fig. 6.9. This density is too large in the regions around the left and right wells and too small at the center. The third orbital is symmetric about the center and is much larger in the region of the center well than the outer wells. When you fully occupy the three lowest orbitals $N = 3$ you produce the correct reference density shown in Fig. 6.10.

This issue arises because the second and third states are supposed to be degenerate and have the same eigenvalue. Errors in energy eigenvalues from the numerical diagonalization are on the order 10^{-11}, thus these degenerate states do not appear to be so. The correct orbital for the second and third occupied state should be a

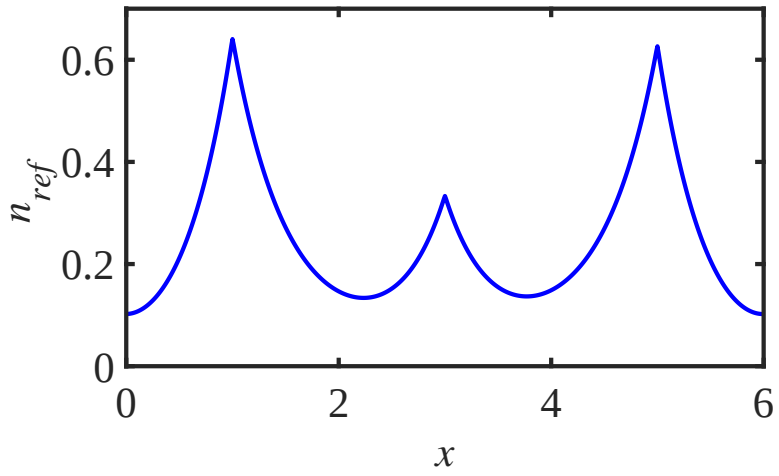

Figure 6.9. The reference density for a unit cell containing three delta wells where $N_\alpha = 0.5$. Here the first and second orbitals produced by the eigenvalue solver are used.

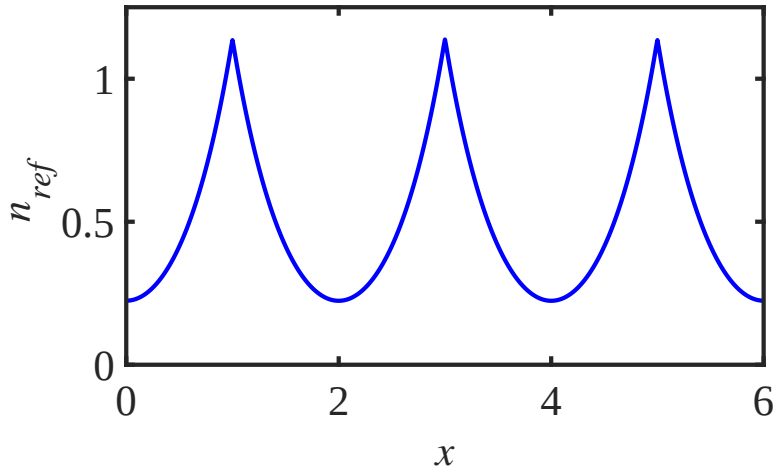

Figure 6.10. The reference density for a unit cell containing three delta wells where $N_\alpha = 1$.

superposition of the second and third eigenstates, ϕ_2 and ϕ_3, that are produced by the numerical solver

$$\phi_{2,3} = \frac{1}{\sqrt{2}}(\phi_2 + \phi_3). \tag{6.7}$$

In Fig. 6.11 the square of the second and third orbitals from the solver are shown along with the square of the superposition $\phi_{2,3}$. Using this new orbital for our calculation

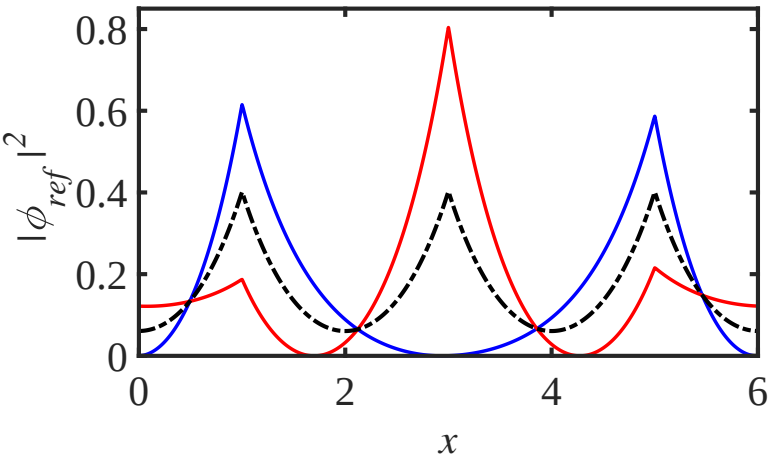

Figure 6.11. The square of the second orbital $|\phi_{ref,2}|^2$ (blue line) and third orbital $|\phi_{ref,3}|^2$ (red line) found by the eigenvalue solver for a unit cell containing three delta wells. These states are degenerate thus the superposition $|\phi_{ref,23}|^2$ (dash-dot black line) of the two states from Eq. 6.7 must be used in place of the second and third orbital when calculating the reference density.

of n_{ref} corrects the errors and produces the correct density.

Ideally a numerical method would not require manually correcting these inaccuracies or simulating such large systems to get the desired results. In theory an inversion on a unit cell which contains only one well (and thus one fragment) should be able to correctly reproduce all of the properties of a periodic chain of identical wells. That is not possible with the method outlined in this section so we develop a better numerical method for these periodic systems.

6.2 Single Well Fragments

In the previous section there was not truly one well per fragment. The periodic fragment potential v_α^P was used for each fragment, which includes effects of v_α from the neighboring unit cells as well as the original unit cell. Thus the calculations had to be done on a much larger spatial grid to minimize delocalizing effects from the neighboring cells. Problems also arose with the numerical diagonalization of the

Hamiltonian matrix for calculating reference densities due to the degenerate states inherent in the system. To correct these we modify our numerical methods by using Bloch functions to calculate n_{ref}, doing fragment calculations on a large finite spatial grid without periodic boundary conditions, and modifying the inversion method.

6.2.1 Reference Density Calculation

The total number of electrons in each unit cell N is chosen, where N is not restricted to integer values. This may seem unphysical, however it is valid since we are simulating only one unit cell from an infinite system. Therefore each unit cell does not need to have integer N for the total infinite system to have an integer number of electrons. Since there is perfect periodicity in our system, we may utilize Bloch functions to get the density of the reference system. The eigenstates are

$$\psi_{j,k}(x) = e^{ikx} u_{j,k}(x) \tag{6.8}$$

where j is the band index, k is the wave number, and $u_{j,k}(x)$ has the periodicity of our unit cell. Our Schrödinger equation may be transformed such that the Hamiltonian has to act only on $u_{j,k}$

$$\begin{aligned} \hat{H}\psi_{j,k}(x) &= \left[-\frac{1}{2}\frac{\partial^2}{\partial_x^2} + v_{\text{ext}}(x) \right] e^{ikx} u_{j,k}(x) \\ &= e^{ikx} \left[\frac{k^2 - \frac{\partial^2}{\partial_x^2}}{2} - ik\frac{\partial}{\partial_x} + v_{\text{ext}}(x) \right] u_{j,k}(x) \\ &= e^{ikx} \hat{H}' u_{j,k}(x) \end{aligned} \tag{6.9}$$

By making k a discrete variable on a k-mesh, we may write $\hat{H}'$ as a matrix (similar to Eq. 6.5) and diagonalize to produce the $u_{j,k}$. With the lattice constant a, the reciprocal lattice constant $b = \frac{2\pi}{a}$ defines the first Brillouin zone G extending from $-b/2$ to $b/2$. Due to the symmetry $E_j(k) = E_j(-k)$ our k-mesh only needs to extend over the region from 0 to $b/2$. We then simply add a factor of two in the total density

calculation. The density at an integer value of electrons, p, is then the integral over the values of k

$$n_p(x) = 2\sum_{j=1}^{p}\int_G dk\Omega_j(k)|\psi_{j,k}(x)|^2 \tag{6.10}$$

where $\Omega_j(k)$ is the density of states. Since we may have non integer values of N, we use the ensemble definition in Eq. 3.4 for the reference density:

$$n_{ref}(x) = wn_{p+1}(x) + (1-w)n_p(x) \tag{6.11}$$

where p is the integer part of N and w is the fractional piece ($N = p + w$).

6.2.2 Fragment Properties and Partition Potentials

If fragment calculations were done on the unit cell with the wrap-around boundary conditions we would get effects from the fragment potential in the neighboring unit cells. To get the v_p that corresponds to our chosen partitioning of only one well per fragment, calculations are done on a finite non-periodic system. This system is much larger than the unit cell and extends the simulation size by a number of domains, N_{dom}, on either side of the original unit cell. This extended system goes from $x_{e,min} = x_{min} - N_{dom} * a$ to $x_{e,max} = x_{max} + N_{dom} * a$.

Depending on the system, we use either the inversion from Sec. 4.1 (for systems of identical wells) or Sec. 4.3 (for systems with different wells). When doing the inversion the initial guess for N_α is usually chosen to be $N_\alpha = \frac{N}{N_f}$. For identical wells, this initial guess is the correct fragment occupation and we use the fixed N_α inversion method. In the systems with different wells, sometimes it is advantageous to use a different initial guess due to the differing well strengths. As electrons will favor the stronger potential well, choosing an initial N_α that reflects this may speed up the inversion process.

In the inversion, we will be calculating fragment properties and comparing the resulting fragment densities to the reference density. As n_{ref} is found over the periodic unit cell and the fragment properties are found over a finite extended system,

transformations will have to be done between the two systems. During each step of the minimization, the partition potential is defined over the length of unit cell. To use it in fragment density calculations we must extend it over the length of the extended fragment system. As v_p must be a periodic function with the periodicity of the unit cell, we construct a new function v_p^E by simply repeating the partition potential N_{dom} times on either side of the original unit cell.

The fragment Hamiltonian using this extended partition potential

$$\hat{H} = -\frac{1}{2}\frac{\partial^2}{\partial_x^2} + v_\alpha(x) + v_p^E(x) \tag{6.12}$$

is written as a matrix using finite differences for the second derivative and then diagonalized to get the orbitals, $\psi_{n,\alpha}(x)$, and corresponding energy levels, $\varepsilon_{n,\alpha}$, of each fragment. All of the fragment densities, energies, chemical potentials, and responses to changes in the potential are calculated using this extended system. To use the spatially dependent properties in the inversions we must transform them to the periodic unit cell. Similar to Eq. 6.3 we make periodic versions of our fragment properties. The densities used in the minimization are periodic versions of the fragment densities

$$n_\alpha^P(x) = n_\alpha(x) + n_\alpha(x-a) + n_\alpha(x+a) \tag{6.13}$$

where we only need to include one unit cell on either side due to the well-localized nature of our fragment densities. The periodic version of the responses χ_α^P are defined in the same manner. These periodic fragment functions are used to find the partition potential at each iteration

Identical Wells

Using this single well fragment method of inverting we are able to do an exact inversion of a chain of identical wells with only a single fragment in the unit cell. In this section we calculated results using a chain of multiple identical wells in the unit cell to provide a better view of the features of the partition potential in the region between fragments. For a periodic system of identical Pöschl-Teller potentials (Eq.

6.2) with $Z_\alpha = 2$ and $\beta_\alpha = 1$ we study the effects of varying occupation numbers and separations on the fragment properties and partition potential.

In Fig. 6.12 we show the density of one fragment for the system of identical wells with separation $d = 2$ for occupation numbers in the range from one to two. The initial increase from $N_\alpha = 1$ to $N_\alpha = 1.2$ causes the fragment density to increase in width, but also slightly decrease in height as it begins to fill the second lowest orbital. Once it has started the transition and begun to include the second orbital, the density continuously increases in height and width as we increase the occupation number of the fragment.

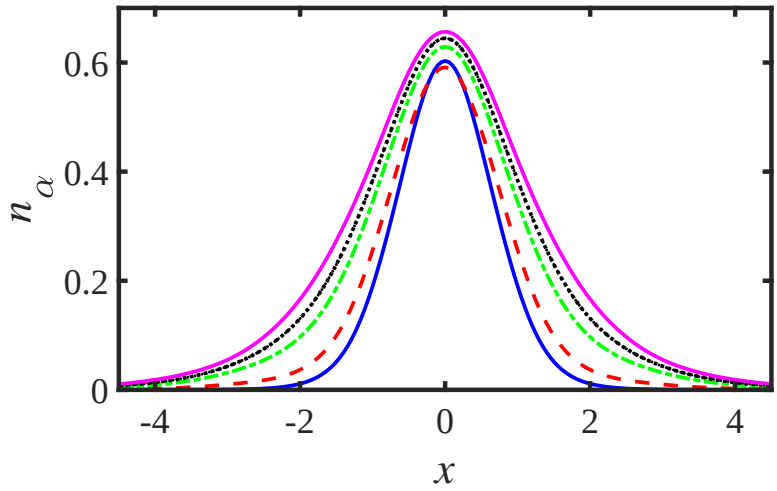

Figure 6.12. The fragment density n_α of one fragment as we vary the occupation number for a system of identical wells with $d = 2$, $Z = 2$, $\beta = 1$. Each fragment has the same occupation number $N_\alpha = 1$ (blue line), $N_\alpha = 1.2$ (dashed red line), $N_\alpha = 1.6$ (dash-dot green line), $N_\alpha = 1.8$ (dotted black line), and $N_\alpha = 2$ (magenta line).

We can see in Fig. 6.13 that as we increase the occupation number towards two, the fragment density becomes wider when compared to the isolated density. When the bound states are not completely filled we can get sharing of electrons and density overlap between fragments. Once we reach $N_\alpha = 2$ all states are fully occupied and the fragment density becomes more localized as compared to the isolated density.

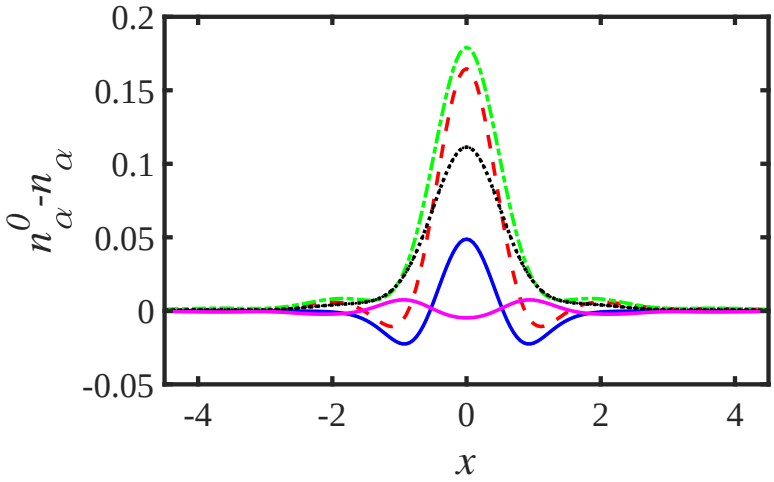

Figure 6.13. The difference between the fragment densities shown in Fig. 6.12 and the isolated density n_α^0 for a fragment with the same occupation number. The fragment densities are from a system of identical wells with $d = 2$, $Z = 2$, $\beta = 1$. The different occupation numbers shown are $N_\alpha = 1$ (blue line), $N_\alpha = 1.2$ (dashed red line), $N_\alpha = 1.6$ (dash-dot green line), $N_\alpha = 1.8$ (dotted black line), and $N_\alpha = 2$ (magenta line).

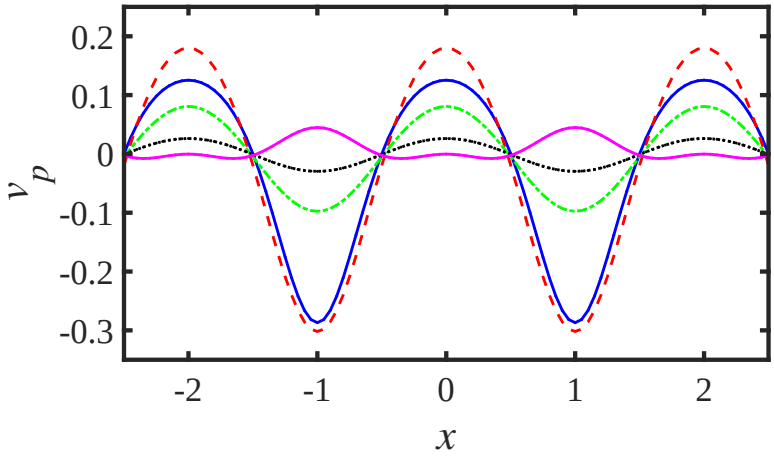

Figure 6.14. The partition potentials v_p which produce the fragment densities in Fig. 6.12 for $N_\alpha = 1$ (blue line), $N_\alpha = 1.2$ (dashed red line), $N_\alpha = 1.6$ (dash-dot green line), $N_\alpha = 1.8$ (dotted black line), and $N_\alpha = 2$ (magenta line). Here $d = 2$ and one fragment is centered at $x = 0$.

The partition potentials which create these fragment densities are shown in Fig. 6.14. For most of the values of N_α, we see a well between fragments with a peak centered at the fragment potential. As we increase the occupation number from 1.8 to 2, the well between fragments in the partition potential transitions to a barrier. One might think that during this change there is a point where v_p is flat between fragments as it switches. Fig. 6.15 shows that this is not the case. Looking at a very small range of N_α between 1.905 and 1.906 we see how the transition begins. The wells do not shrink in size until they flatten and then grow to become barriers. Instead, a peak begins to emerge at the center of the well. The well feature shrinks as the peak continues to grow until eventually overtaking the well and we are only left with a barrier between fragments. This shift in the features of v_p happens as we approach the highest bound state and works to reduce the density overlap between fragments.

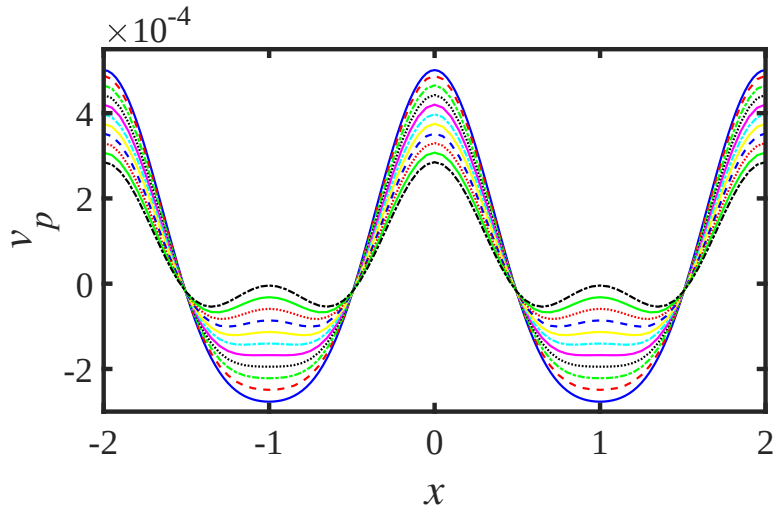

Figure 6.15. The transition of the partition potential from wells to barriers between fragments as the fragment occupation number increases through the values: $N_\alpha = 1.905$ (blue line), $N_\alpha = 1.9051$ (dashed red line), $N_\alpha = 1.9052$ (dash-dot green line), $N_\alpha = 1.9053$ (dotted black line), $N_\alpha = 1.9054$ (magenta line), $N_\alpha = 1.9055$ (dash-dot cyan line), $N_\alpha = 1.9056$ (yellow line), $N_\alpha = 1.9057$ (dashed blue line), $N_\alpha = 1.9058$ (dotted red line), $N_\alpha = 1.9059$ (green line), $N_\alpha = 1.906$ (dash-dot black line).

Changing the separation between fragments also has an effect on the fragment properties and partition potential. Looking first at the case of $N_\alpha = 2$ in Fig. 6.16 we see that the fragment densities do not differ very much as we vary the separation d between 1 and 4. The small changes become more apparent when looking at the

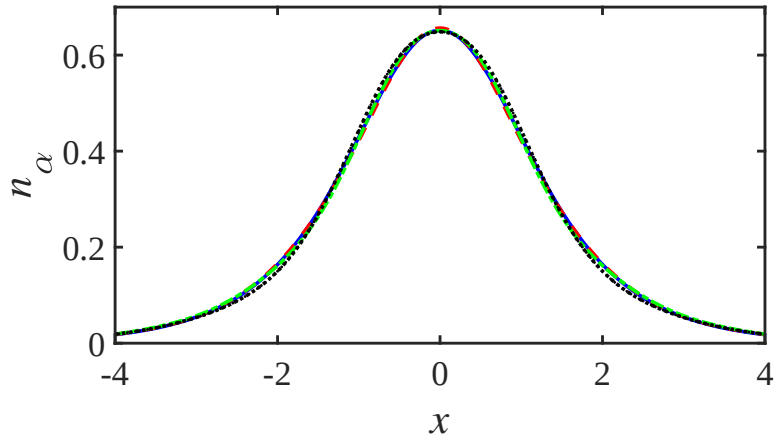

Figure 6.16. The fragment density n_α of one fragment as we increase the separation for a system of identical wells with $N_\alpha = 2$, $Z = 2$, $\beta = 1$. The separations $d = 1$ (blue line), $d = 2$ (dashed red line), $d = 3$ (dash-dot green line), and $d = 4$ (dotted black line). Each fragment only has two bound states, which are filled, thus there is not a large variation between fragment densities as the separation changes.

difference between n_α and n_α^0 in Fig. 6.17. At smaller separations the well spreads further towards the neighboring fragments than when $d = 4$.

In Fig. 6.18 we see the partition potentials producing these fragment densities. As the separation, and thus the periodicity, is different in each case, we plot v_p vs a distance that is scaled based on the chosen separation of each system. In these v_p's there is a barrier between the fragments with a well and peak combination centered at the fragment potential. The features of these partition potentials remain at each separation, only the magnitude of the features of change with separation. The features in v_p are defined by the occupation number of the systems, not the separation between fragments.

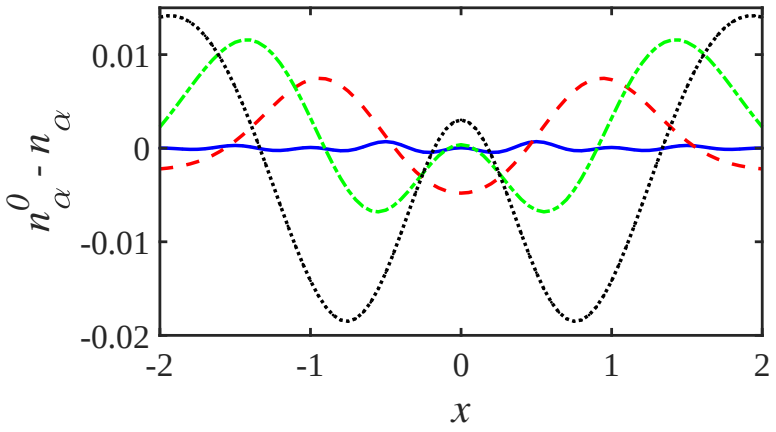

Figure 6.17. The difference between the fragment densities shown in Fig. 6.16 and the isolated density n^0_α for one fragment as we change the separation $d = 1$ (blue line), $d = 2$ (dashed red line), $d = 3$ (dash-dot green line), and $d = 4$ (dotted black line). The fragment densities are from a system of identical wells where $N_\alpha = 2$, $Z = 2$, $\beta = 1$.

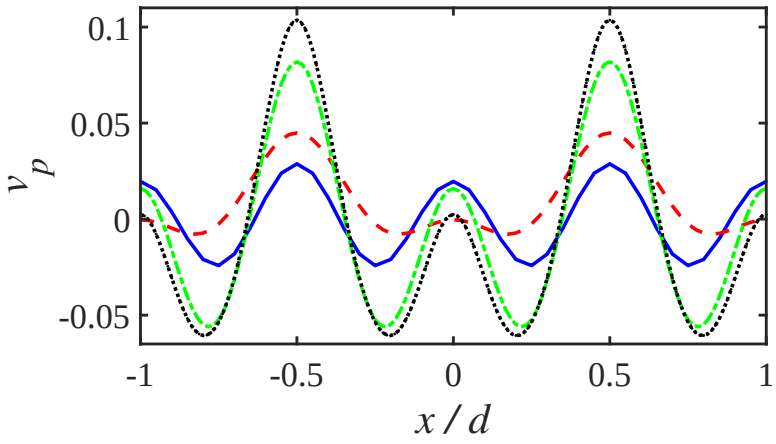

Figure 6.18. The partition potentials corresponding to the fragment densities shown in Fig. 6.16 where $N_\alpha = 2$ for different separations. We have scaled the x-axis to show how the features of v_p at the center of each fragment and in between the fragments compare for different values of d. For all of the values $d = 1$ (blue line), $d = 2$ (dashed red line), $d = 3$ (dash-dot green line), and $d = 4$ (dotted black line) we see a peak centered at each fragment, barriers in between the fragments, and wells between each of these features. The sizes of the features change, but the features themselves are dictated by the occupation number in this case not the separation.

Next, looking at the case of $N_\alpha = 0.5$ we see more noticeable changes in the fragment densities (Fig. 6.19) as we vary d than when the fragments were fully occupied. The difference when comparing the fragment densities to the isolated densities is

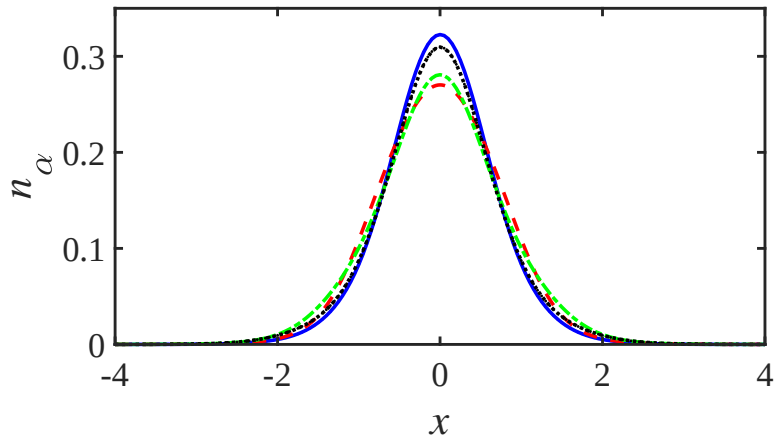

Figure 6.19. The fragment density n_α of one fragment as we increase the separation for a system of identical wells with $N_\alpha = 0.5$, $Z = 2$, $\beta = 1$. The separations $d = 1$ (blue line), $d = 2$ (dashed red line), $d = 3$ (dash-dot green line), and $d = 4$ (dotted black line).

shown in Fig. 6.20. Here we see in each case that the fragment density has decreased in magnitude at the peak and spread towards the neighboring fragment.

The partition potentials which produce the fragment densities in Fig. 6.19 are shown in Fig. 6.21. Between the fragments v_p has a well, now that the bound states are not fully occupied as in the $N_\alpha = 2$ case. At the center of the fragments there is a peak in v_p which causes the fragment densities to spread and increases the density overlap. As in the $N_\alpha = 2$ case, the features of v_p don't change with changing separations, only the magnitude of the values change.

Different Wells

Systems with nonidentical wells can be studied using the N_α optimizing method from Sec. 4.3. The fragment potentials for a periodic system with two different

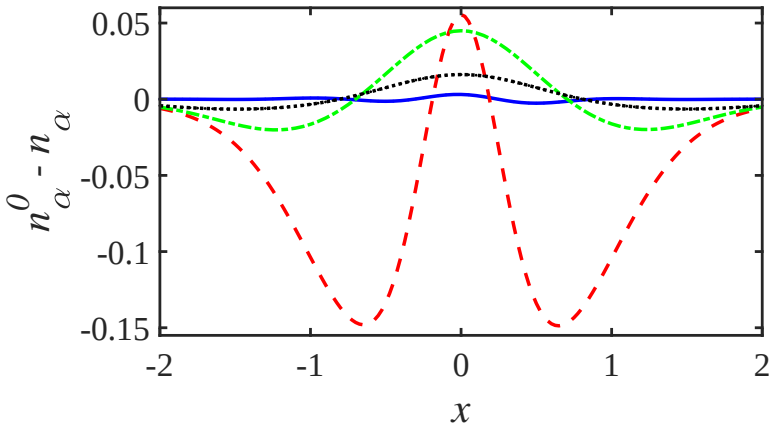

Figure 6.20. The difference between the fragment densities shown in Fig. 6.19 and the isolated density n^0_α for one fragment as we change the separation $d = 1$ (blue line), $d = 2$ (dashed red line), $d = 3$ (dash-dot green line), and $d = 4$ (dotted black line). The fragment densities are from a system of identical wells where $N_\alpha = 0.5$, $Z = 2$, $\beta = 1$.

Pöschl-Teller wells in the unit cell are shown in Fig. 6.22. We look at results for fragment well strengths $Z_1 = 3$ and $Z_2 = 3.5$ where $\beta_\alpha = 1$ with a separation $d = 4$.

As the total number of electrons in the unit cell is increased, the fragment occupations change in an alternating manner. In Fig. 6.23 we increase N through integer numbers until the bound states of the unit cell are fully occupied. When $N = 1$, the electron goes to the deeper well such that $N_1 = 0$ and $N_2 = 1$. As we increase to $N = 2$, the shallower wells gains the next electron while N_2 remains at one. Going up to $N = 3$, the fragment densities begin to have overlap and the fragment occupations do not go to integer values. The majority goes to the deeper well, but some is added to fragment 1 as well. At $N = 4$, the bound states of the unit cell are fully occupied and the fragments are forced back to integer occupation numbers $N_\alpha = 2$.

The partition potentials from these integer N are shown in Fig. 6.24. When $N = 1$ there is no occupation on fragment 1 and the v_p is only affecting n_2. Here v_p has a well on either side of v_2 and a barrier at the center of v_1. This helps spread the fragment density out from the isolated density while keeping it away from the center of fragment 1. Continuing to increase N, wells appear in v_p between the fragments.

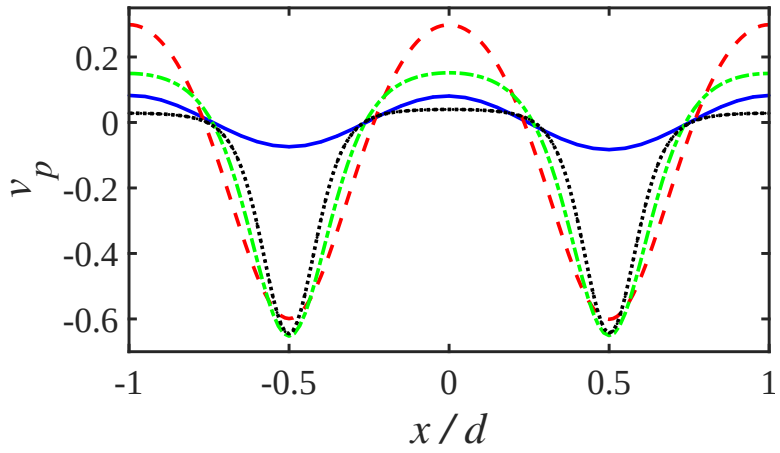

Figure 6.21. The partition potentials corresponding to the fragment densities shown in Fig. 6.19 where $N_\alpha = 0.5$ for different separations. We have scaled the x-axis to show how the features of v_p at the center of each fragment and in between the fragments compare for different values of d. For all of the values $d = 1$ (blue line), $d = 2$ (dashed red line), $d = 3$ (dash-dot green line), and $d = 4$ (dotted black line) we see a peak centered at each fragment and wells between each fragment. There is a change in the features of v_p from Fig. 6.18. Now that the bound states of the fragments are not filled the barriers between fragments become wells between fragments. In this case we also see that the sizes of the features change with separation but the features themselves are still dictated by the occupation number.

The wells are not centered between the fragments until we reach the fully occupied state at $N = 4$. Instead they are shifted away from the step in v_p. There is a step up in the partition potential towards the fragment which is gaining fewer electrons. As the occupation numbers increase and the densities overlap more, a well appears in v_p near the center of the fragment, which increases the density at the center and keeps it localized to its fragment.

The fragment occupations take turns increasing as we change N from one to four. They begin by remaining fixed while the other fragment goes up to the integer and then switching roles as we approach the next integer. When the fragment densities begin to overlap the fragment occupations do not remain completely frozen. In Fig. 6.25 we see how the fragment occupations change as we increase N. At each integer

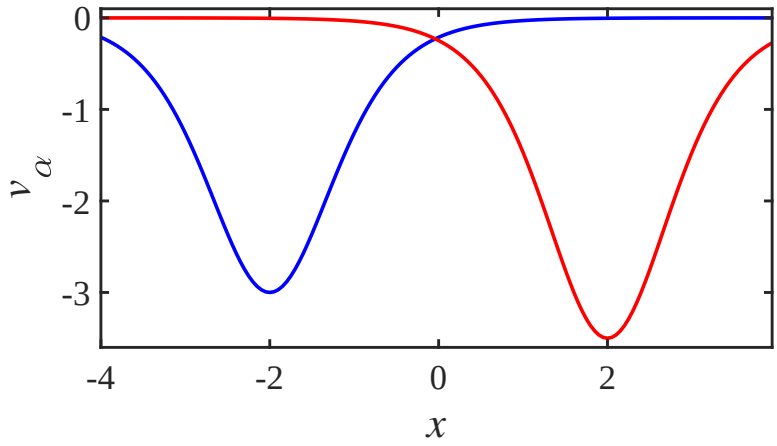

Figure 6.22. Fragment potentials in the unit cell of a system with unequal well strengths where $Z_1 = 3$ (blue line) and $Z_2 = 3.5$ (red line) at a separation $d = 4$.

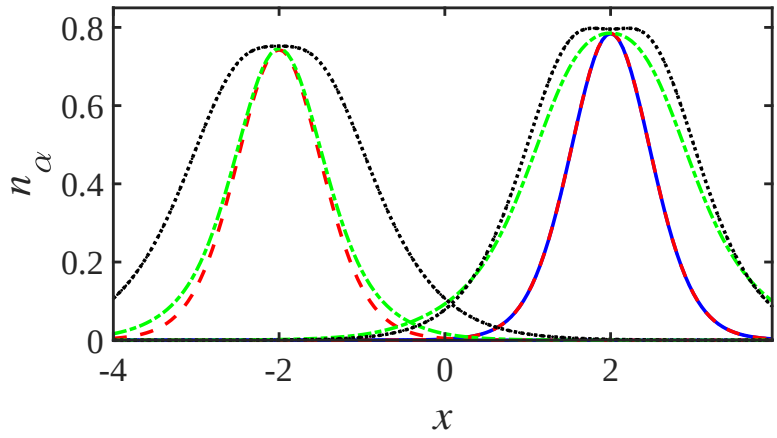

Figure 6.23. The fragment densities for a system where there are unequal well strengths $Z_1 = 3$ and $Z_2 = 3.5$ separated $d = 4$ at integer total system electron numbers $N = 1$ (blue line), $N = 2$ (dashed red line), $N = 3$ (dash-dot green line), and $N = 4$ (dotted black line).

value of N, the fragment which gains more occupation switches. The rate of change of each fragment occupation is discontinuous as each integer N and when each N_α first reaches an integer value. It would not be possible to see this behavior with other subsystem methods as they do not allow for fractional occupation numbers like P-DFT.

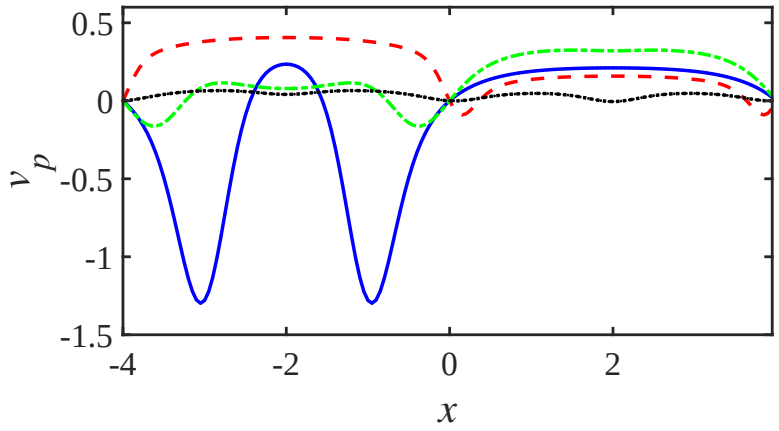

Figure 6.24. The partition potentials corresponding to the fragment potentials in Fig. 6.23 for a system with unequal well strengths $Z_1 = 3$ and $Z_2 = 3.5$ as we increase the total number of electrons in the system: $N = 1$ (blue line), $N = 2$ (dashed red line), $N = 3$ (dash-dot green line), and $N = 4$ (dotted black line).

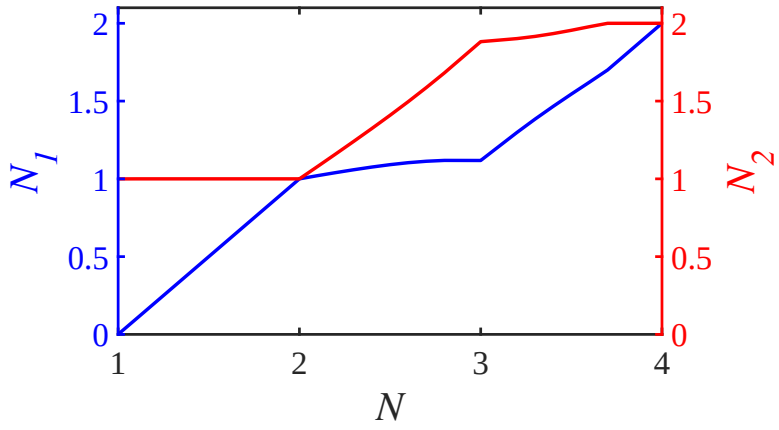

Figure 6.25. Fragment occupation numbers N_1 (blue line) and N_2 (red line) corresponding to the system in Fig. 6.22 where we have unequal well strengths $Z_1 = 3$ and $Z_2 = 3.5$. As we increase the number of electrons from $N = 1$ to $N = 4$ the fragment occupations increase at alternating rates which depend on the energy levels of the fragment wells and the amount of fragment density overlap.

7. SUMMARY

P-DFT is ideal for studying charge transfer as it allows fragments to have a non-integer occupation number and correctly treats this fractional charge by using ensembles to calculate system properties [18]. Due to the well-localized fragment densities produced by allowing for these fractional charges, P-DFT is also ideal for studying fragment interactions and the partition potential of each system has chemically meaningful properties.

We extended the scope of P-DFT to include (semi)infinite systems and studied the charge transfer of model systems relevant to metal and semiconductor surface interactions. A new method for doing P-DFT inversions was developed to address challenges arising in semi-infinite systems where one fragment is infinite and the other finite. The normal P-DFT constraints were not sufficient to correctly optimize the occupation number of the finite system, especially in those cases where the fragment chemical potentials do not equalize. Applying this new inversion technique to simple 1-D systems allowed us to find and study the *exact* partition potential and the behavior of the charge transfer in the system.

We presented results from these inversions of our metal-atom (semi-infinite) and periodic (infinite) system. By studying the fragment densities of the systems we demonstrated that when a fragment has an integer occupation number, the density response to small changes in μ or N occurs exclusively on the other fragment in the system (except for homonuclear potentials). In the metal-atom system, when the atom has an integer occupation number, the density response to infinitesimal changes in μ is located in the metallic region and only affects the surface Friedel oscillations. When the atom has a fractional charge, the density response is almost exclusively around the atom. The partition potentials from these systems, which modify the isolated fragment densities such that they recreate the interacting system density,

gave insights into the fragment interactions and how they change with separation and electron number. Key features of the partition potentials shown are also present in the exact KS potential. These features play similar roles in P-DFT and KS-DFT by modifying a non-interacting system such that it recreates the density of the interacting system.

From our inversions we have also demonstrated that the derivative discontinuity in the energy of an open system as a function of N smooths, not only for finite temperatures (as had been previously shown), but also at finite distances. Although this discontinuous behavior decreases, we have seen that it does not completely disappear. This smoothing of μ vs N had not been shown before for finite separations and would not have been possible with other DFT or subsystem DFT methods. P-DFT's well-localized fragment densities and possible non-integer occupation numbers are the key features which allowed us to demonstrate these charge transfer behaviors.

REFERENCES

[1] Walter Kohn and Lu Jeu Sham. Self-consistent equations including exchange and correlation effects. *Physical Review*, 140(4A):A1133, 1965.

[2] P. Hohenberg and W. Kohn. Inhomogeneous electron gas. *Physical Review*, 136:B864–B871, Nov 1964.

[3] Walter Kohn. Nobel lecture: Electronic structure of matterwave functions and density functionals. *Reviews of Modern Physics*, 71(5):1253, 1999.

[4] Aron J Cohen, Paula Mori-Sánchez, and Weitao Yang. Insights into current limitations of density functional theory. *Science*, 321(5890):792–794, 2008.

[5] Jonathan Nafziger and Adam Wasserman. Fragment-based treatment of delocalization and static correlation errors in density-functional theory. *The Journal of Chemical Physics*, 143(23), 2015.

[6] Llewellyn H Thomas. The calculation of atomic fields. In *Mathematical Proceedings of the Cambridge Philosophical Society*, volume 23, pages 542–548. Cambridge Univ Press, 1927.

[7] Enrico Fermi. Eine statistische methode zur bestimmung einiger eigenschaften des atoms und ihre anwendung auf die theorie des periodischen systems der elemente. *Zeitschrift für Physik*, 48(1-2):73–79, 1928.

[8] John P Perdew. Density-functional approximation for the correlation energy of the inhomogeneous electron gas. *Physical Review B*, 33(12):8822, 1986.

[9] John P Perdew, Kieron Burke, and Matthias Ernzerhof. Generalized gradient approximation made simple. *Physical review letters*, 77(18):3865, 1996.

[10] John P Perdew and Karla Schmidt. Jacob's ladder of density functional approximations for the exchange-correlation energy. In *AIP Conference Proceedings*, pages 1–20, 2001.

[11] New International Version. *Genesis*, 28:10–12.

[12] John P Perdew and Lucian A Constantin. Laplacian-level density functionals for the kinetic energy density and exchange-correlation energy. *Physical Review B*, 75(15):155109, 2007.

[13] Axel D Becke. Density-functional thermochemistry. iii. the role of exact exchange. *The Journal of Chemical Physics*, 98(7):5648–5652, 1993.

[14] Chengteh Lee, Weitao Yang, and Robert G Parr. Development of the colle-salvetti correlation-energy formula into a functional of the electron density. *Physical Review B*, 37(2):785, 1988.

[15] Kieron Burke. Perspective on density functional theory. *The Journal of Chemical Physics*, 136(15):150901, 2012.

[16] Paula Mori-Sánchez, Aron J Cohen, and Weitao Yang. Localization and delocalization errors in density functional theory and implications for band-gap prediction. *Physical review letters*, 100(14):146401, 2008.

[17] AJ Cohen, P Mori-Sánchez, and W Yang. Fractional spins and static correlation error in density functional theory. *The Journal of Chemical Physics*, 129(12):121104–121104, 2008.

[18] John P. Perdew, Robert G. Parr, Mel Levy, and Jose L. Balduz. Density-functional theory for fractional particle number: Derivative discontinuities of the energy. *Physical review letters*, 49:1691–1694, Dec 1982.

[19] Paula Mori-Sánchez, Aron J Cohen, and Weitao Yang. Discontinuous nature of the exchange-correlation functional in strongly correlated systems. *Physical review letters*, 102(6):066403, 2009.

[20] Martín A Mosquera and Adam Wasserman. Derivative discontinuities in density functional theory. *Molecular Physics*, 112(23):2997–3013, 2014.

[21] Adam Wasserman, Jonathan Nafziger, Kaili Jiang, Min-Cheol Kim, Eunji Sim, and Kieron Burke. The importance of being inconsistent. *Annual review of physical chemistry*, 68:555–581, 2017.

[22] John P Perdew. What do the kohn-sham orbital energies mean? how do atoms dissociate? In *Density Functional Methods in Physics*, pages 265–308. Springer, 1985.

[23] EJ Baerends, OV Gritsenko, and R Van Meer. The kohn–sham gap, the fundamental gap and the optical gap: the physical meaning of occupied and virtual kohn–sham orbital energies. *Physical Chemistry Chemical Physics*, 15(39):16408–16425, 2013.

[24] Aron J Cohen, Paula Mori-Sánchez, and Weitao Yang. Fractional charge perspective on the band gap in density-functional theory. *Physical Review B*, 77(11):115123, 2008.

[25] Martin A Mosquera and Adam Wasserman. Integer discontinuity of density functional theory. *Physical Review A*, 89(5):052506, 2014.

[26] Aurora Pribram-Jones, David A Gross, and Kieron Burke. Dft: A theory full of holes? *Annual review of physical chemistry*, 66:283–304, 2015.

[27] Michael G Medvedev, Ivan S Bushmarinov, Jianwei Sun, John P Perdew, and Konstantin A Lyssenko. Density functional theory is straying from the path toward the exact functional. *Science*, 355(6320):49–52, 2017.

[28] Peter Elliott, Kieron Burke, Morrel H. Cohen, and Adam Wasserman. Partition density-functional theory. *Physical Review A*, 82:024501, Aug 2010.

[29] Jonathan Nafziger and Adam Wasserman. Density-based partitioning methods for ground-state molecular calculations. *Journal of Physical Chemistry A*, 118(36):7623–7639, 2014.

[30] Peter Elliott, Morrel H Cohen, Adam Wasserman, and Kieron Burke. Density functional partition theory with fractional occupations. *Journal of chemical theory and computation*, 5(4):827–833, 2009.

[31] Martín A Mosquera, Daniel Jensen, and Adam Wasserman. Fragment-based time-dependent density functional theory. *Physical review letters*, 111(2):023001, 2013.

[32] Martín A Mosquera and Adam Wasserman. Current density partitioning in time-dependent current density functional theory. *The Journal of Chemical Physics*, 140(18):18A525, 2014.

[33] Martín A Mosquera and Adam Wasserman. Non-analytic spin-density functionals. In *Density Functionals*, pages 145–174. Springer, 2014.

[34] Martín A Mosquera and Adam Wasserman. Partition density functional theory and its extension to the spin-polarized case. *Molecular Physics*, 111(4):505–515, 2013.

[35] Morrel H Cohen and Adam Wasserman. On hardness and electronegativity equalization in chemical reactivity theory. *Journal of statistical physics*, 125(5-6):1121–1139, 2006.

[36] Morrel H Cohen, Adam Wasserman, and Kieron Burke. Partition theory: A very simple illustration. *The Journal of Physical Chemistry A*, 111(49):12447–12453, 2007.

[37] Morrel H Cohen, Adam Wasserman, Roberto Car, and Kieron Burke. Charge transfer in partition theory. *The Journal of Physical Chemistry A*, 113(10):2183–2192, 2009.

[38] Chen Huang, Michele Pavone, and Emily A Carter. Quantum mechanical embedding theory based on a unique embedding potential. *The Journal of Chemical Physics*, 134(15):154110, 2011.

[39] Christoph R Jacob and Johannes Neugebauer. Subsystem density-functional theory. *Wiley Interdisciplinary Reviews: Computational Molecular Science*, 4(4):325–362, 2014.

[40] Alisa Krishtal, Debalina Sinha, Alessandro Genova, and Michele Pavanello. Subsystem density-functional theory as an effective tool for modeling ground and excited states, their dynamics and many-body interactions. *Journal of Physics: Condensed Matter*, 27(18):183202, 2015.

[41] Tomasz A Wesolowski, Sapana Shedge, and Xiuwen Zhou. Frozen-density embedding strategy for multilevel simulations of electronic structure. *Chemical reviews*, 115(12):5891–5928, 2015.

[42] Pietro Cortona. Self-consistently determined properties of solids without band-structure calculations. *Physical Review B*, 44(16):8454, 1991.

[43] Tomasz Adam Wesolowski and Arieh Warshel. Frozen density functional approach for ab initio calculations of solvated molecules. *The Journal of Physical Chemistry*, 97(30):8050–8053, 1993.

[44] N Govind, YA Wang, AJR Da Silva, and EA Carter. Accurate ab initio energetics of extended systems via explicit correlation embedded in a density functional environment. *Chemical physics letters*, 295(1):129–134, 1998.

[45] Morrel H Cohen and Adam Wasserman. On the foundations of chemical reactivity theory. *The Journal of Physical Chemistry A*, 111(11):2229–2242, 2007.

[46] Chen Huang and Emily A Carter. Potential-functional embedding theory for molecules and materials. *The Journal of Chemical Physics*, 135(19):194104, 2011.

[47] Morrel H Cohen and Adam Wasserman. Revisiting n-continuous density-functional theory: Chemical reactivity and atoms in molecules. *Israel journal of chemistry*, 43(3-4):219–227, 2003.

[48] Jacek Rychlewski and Robert G Parr. The atom in a molecule: A wave function approach. *The Journal of Chemical Physics*, 84(3):1696–1703, 1986.

[49] Rougang Tang, Jonathan Nafziger, and Adam Wasserman. Fragment occupations in partition density functional theory. *Physical Chemistry Chemical Physics*, 14(21):7780–7786, 2012.

[50] Jonathan Nafziger, Qin Wu, and Adam Wasserman. Molecular binding energies from partition density functional theory. *The Journal of Chemical Physics*, 135(23):234101, 2011.

[51] Sara Gómez, Jonathan Nafziger, Albeiro Restrepo, and Adam Wasserman. Partition-dft on the water dimer. *The Journal of Chemical Physics*, 146(7):074106, 2017.

[52] Jonathan Nafziger. *Partition density functional theory.* PhD thesis, Purdue University, 2015.

[53] Jonathan Nafziger, Kaili Jiang, and Adam Wasserman. Accurate reference data for the nonadditive, noninteracting kinetic energy in covalent bonds. *Journal of chemical theory and computation*, 13(2):577–586, 2017.

[54] Kaili Jiang, Jonathan Nafziger, and Adam Wasserman. Constructing a non-additive non-interacting kinetic energy functional approximation for covalent bonds from exact conditions. *arXiv preprint arXiv:1808.02951*, 2018.

[55] Christoph R Jacob. Unambiguous optimization of effective potentials in finite basis sets. *The Journal of Chemical Physics*, 135(24):244102, 2011.

[56] John P Perdew and John R Smith. Can desorption be described by the local density formalism? *Surface science*, 141(1):L295–L303, 1984.

[57] Weitao Yang and Robert G Parr. Hardness, softness, and the fukui function in the electronic theory of metals and catalysis. *Proceedings of the National Academy of Sciences*, 82(20):6723–6726, 1985.

[58] Kenichi Fukui. Theory of orientation and stereoselection. In *Orientation and Stereoselection*, pages 1–85. Springer, 1970.

[59] Kenichi Fukui. Role of frontier orbitals in chemical reactions. *Science*, 218(4574):747–754, 1982.

[60] Kee-Joo Chang and Marvin L Cohen. Structural and electronic properties of the high-pressure hexagonal phases of si. *Physical Review B*, 30(9):5376, 1984.

[61] N Nilius, Maria V Ganduglia-Pirovano, Veronika Brázdová, Maria Kulawik, Joachim Sauer, and H-J Freund. Counting electrons transferred through a thin alumina film into au chains. *Physical review letters*, 100(9):096802, 2008.

[62] Yaroslava Lykhach, Sergey M Kozlov, Tomáš Skála, Andrii Tovt, Vitalii Stetsovych, Nataliya Tsud, Filip Dvořák, Viktor Johánek, Armin Neitzel, Josef Mysliveček, et al. Counting electrons on supported nanoparticles. *Nature materials*, 15(3):284, 2016.

[63] David A Egger, Zhen-Fei Liu, Jeffrey B Neaton, and Leeor Kronik. Reliable energy level alignment at physisorbed molecule–metal interfaces from density functional theory. *Nano letters*, 15(4):2448–2455, 2015.

[64] F Flores, J Ortega, and H Vazquez. Modelling energy level alignment at organic interfaces and density functional theory. *Physical Chemistry Chemical Physics*, 11(39):8658–8675, 2009.

[65] Zhen-Fei Liu, David A Egger, Sivan Refaely-Abramson, Leeor Kronik, and Jeffrey B Neaton. Energy level alignment at molecule-metal interfaces from an optimally tuned range-separated hybrid functional. *The Journal of Chemical Physics*, 146(9):092326, 2017.

[66] Matthew B. Goldey, Nicholas P. Brawand, Mrton Vrs, and Giulia Galli. Charge transport in nanostructured materials: Implementation and verification of constrained density functional theory. *Journal of Chemical Theory and Computation*, 13(6):2581–2590, 2017.

[67] Benjamin G Janesko. Density functional theory beyond the generalized gradient approximation for surface chemistry. In *Density Functionals*, pages 25–51. Springer, 2014.

[68] Michele Pavanello, Troy Van Voorhis, Lucas Visscher, and Johannes Neugebauer. An accurate and linear-scaling method for calculating charge-transfer excitation energies and diabatic couplings. *The Journal of chemical physics*, 138(5):054101, 2013.

[69] Pablo Ramos and Michele Pavanello. Quantifying environmental effects on the decay of hole transfer couplings in biosystems. *Journal of chemical theory and computation*, 10(6):2546–2556, 2014.

[70] Alisa Solovyeva, Michele Pavanello, and Johannes Neugebauer. Describing long-range charge-separation processes with subsystem density-functional theory. *The Journal of Chemical Physics*, 140(16):164103, 2014.

[71] Alessandro Genova, Davide Ceresoli, and Michele Pavanello. Periodic subsystem density-functional theory. *Journal of Chemical Physics*, 141(17), 2014.

[72] Alessandro Genova, Davide Ceresoli, Alisa Krishtal, Oliviero Andreussi, Robert A DiStasio Jr, and Michele Pavanello. eqe: An open-source density functional embedding theory code for the condensed phase. *International Journal of Quantum Chemistry*, 117(16):e25401, 2017.

[73] Yongqiang Xue, Supriyo Datta, and Mark A Ratner. Charge transfer and band lineup in molecular electronic devices: A chemical and numerical interpretation. *The Journal of Chemical Physics*, 115(9):4292–4299, 2001.

[74] Kenji Toyoda, Yosuke Nakano, Ikutaro Hamada, Kyuho Lee, Susumu Yanagisawa, and Yoshitada Morikawa. First-principles study of the pentacene/cu (111) interface: Adsorption states and vacuum level shifts. *Journal of Electron Spectroscopy and Related Phenomena*, 174(1):78–84, 2009.

[75] L. D. (Lev Davidovich) Landau. *Quantum mechanics : non-relativistic theory*. Landau, L. D. (Lev Davidovich), 1908-1968. Teoreticheskaia fizika (Izd. 3-e). English ; v. 3. Butterworth-Heinemann, 3rd edition revised and enlarged edition, 1977.

[76] E. Prodan. Nearsightedness of electronic matter in one dimension. *Physical Review B*, 73:085108, Feb 2006.

[77] A Benítez and CR Proetto. Kohn-sham potential for a strongly correlated finite system with fractional occupancy. *Physical Review A*, 94(5):052506, 2016.

[78] N Helbig, IV Tokatly, and Angel Rubio. Exact kohn–sham potential of strongly correlated finite systems. *The Journal of Chemical Physics*, 131(22):224105, 2009.

[79] Matthew JP Hodgson, Eli Kraisler, Axel Schild, and Eberhard KU Gross. How interatomic steps in the exact kohn–sham potential relate to derivative discontinuities of the energy. *The Journal of Physical Chemistry Letters*, 8(24):5974–5980, 2017.

[80] Paolo Giannozzi, Stefano Baroni, Nicola Bonini, Matteo Calandra, Roberto Car, Carlo Cavazzoni, Davide Ceresoli, Guido L Chiarotti, Matteo Cococcioni, Ismaila Dabo, et al. Quantum espresso: a modular and open-source software project for quantum simulations of materials. *Journal of Physics: Condensed matter*, 21(39):395502, 2009.

[81] Alessandro Genova and Michele Pavanello. Exploiting the locality of periodic subsystem density-functional theory: efficient sampling of the brillouin zone. *Journal of Physics: Condensed Matter*, 27(49):495501, 2015.

[82] Kuang Yu, Florian Libisch, and Emily A Carter. Implementation of density functional embedding theory within the projector-augmented-wave method and applications to semiconductor defect states. *The Journal of Chemical Physics*, 143(10):102806, 2015.

[83] Ruslan Kevorkyants, Xiqiao Wang, David M Close, and Michele Pavanello. Calculating hyperfine couplings in large ionic crystals containing hundreds of qm atoms: subsystem dft is the key. *The Journal of Physical Chemistry B*, 117(45):13967–13974, 2013.

[84] M. Stone and P. M. Goldbart. *Mathematics for Physics*. Cambridge University Press, 2009.

A. ENSEMBLES FOR FRACTIONAL CHARGES

In 1982 it was shown by Perdew, Parr, Levy, and Balduz (PPLB) [18] that the Hohenberg-Kohn theorem could be extended to densities which integrate to non-integer electron numbers. Using an ensemble definition for the density, energy, and other physical properties of a system they showed that DFT could be used for systems with fractional particle number, a key element in P-DFT.

The Hohenberg-Kohn (HK) theorem showed that there is a functional $E_v[n(\mathbf{r})]$ such that minimization with respect to variations of $n(\mathbf{r})$ under the constraint $\int d\mathbf{r} n(\mathbf{r}) = N$, yields the ground-state density $n(\mathbf{r})$ and energy E [2]. By introducing a Lagrange multiplier μ,

$$\delta\Big\{E_v[n] - \mu \int d\mathbf{r} n(\mathbf{r})\Big\} = 0 \tag{A.1}$$

the number conserving variations of $n(\mathbf{r})$ may be replaced by arbitrary ones. The Euler-Lagrange equation for $n(\mathbf{r})$ is then

$$\frac{\delta E_v[n]}{\delta n(\mathbf{r})} = \mu \tag{A.2}$$

and thus

$$\mu = \frac{\partial E}{\partial N} \tag{A.3}$$

From Eq. A.3 this Lagrange multiplier has been identified as the chemical potential.

Fractional electron number N may arise as a time average in an open system. This system cannot be described by a pure state, but must be described by an ensemble Γ or statistical mixture of states. The ensemble is defined using a set of pure states and their probabilities. With the ensembles, HK theorem can be used with trial densities $n(\mathbf{r})$ which integrate to $N = p + w$ electrons where p is an integer and $0 \leq w \leq 1$. A

constrained search over these ensembles can be used to minimize the energy with the universal variational functional

$$F[n] = \min_{\Gamma \to n} \langle \hat{T} + \hat{V}_{ee} \rangle_\Gamma \tag{A.4}$$

where $\hat{T}$ is the kinetic energy operator and $\hat{V}_{ee}$ is the electron-electron repulsion energy operator. This variational functional searches over all Γ that are mixtures of a p electron pure state and a $p+1$ electron pure state, which yield $n(\mathbf{r})$ and minimizes $\langle \hat{T} + \hat{V}_{ee} \rangle$. The probabilities for these states must be $1-w$ and w, since $(1-w)p + w(p+1) = p + w$. The density is then $n(\mathbf{r}) = (1-w)n_p(\mathbf{r}) + w n_{p+1}(\mathbf{r})$. A variational principle exists such that minimizing $E_v[n] \equiv F[n] + \int d\mathbf{r} n(\mathbf{r}) v(\mathbf{r})$, with respect to number conserving variations of $n(\mathbf{r})$, yields the lowest average energy that can be achieved by $p + w$ electrons in a mixture of the allowed type.

$$E = (1-w)E_p + wE_{p+1} \tag{A.5}$$

where E_p and E_{p+1} are the ground-state energies for p and $p+1$ electrons in the external potential $v(\mathbf{r})$. If the constrained search of Eq. A.4 is extended over all statistical mixtures yielding $n(\mathbf{r})$, the minimum of $E_v[n]$ over all $n(\mathbf{r})$ integrating to $p + w$ electrons is still Eq. A.5 (for ordinary electronic systems).

Eq. A.5 tells us that the curve of E versus N is a series of straight-line segments and is a continuous curve, but its derivative $\mu = \frac{\partial E}{\partial N}$ has possible discontinuities at integer values of N as is shown in the cartoon in Fig. A.1. It follows that at zero temperature, an atom (of nuclear charge Z) in equilibrium with a distant reservoir will be neutral for any chemical potential in the range $-I < \mu < -A$, where $I = E_{Z-1} - E_Z$ is the first ionization potential and $A = E_Z - E_{Z+1}$ is the electron affinity. However at finite temperatures this behavior should smooth so that $\frac{\partial E}{\partial N}$ is a more continuous function. It has been supposed, but not previously seen, that these discontinuities become rounded at finite separations as well [22]. This study of an atom in equilibrium with a reservoir is analogous to our system of an atom interacting with a metal surface in Sec. 5.

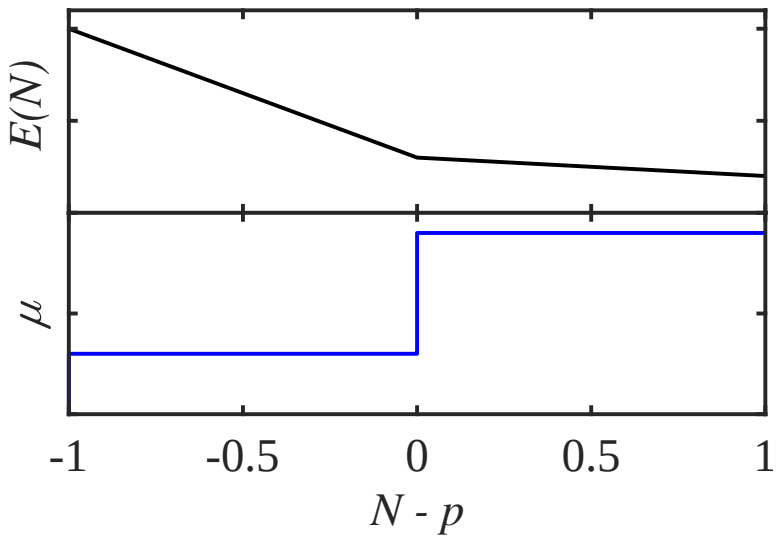

Figure A.1. A simple cartoon illustrating the behavior of the energy and chemical potential of an open system as a function of particle number N where p is the integer part of the number of electrons in the chosen system.

B. DENSITY USING GREEN'S FUNCTIONS

Inspired by a paper from Prodan on the nearsightedness of electronic matter in one dimension [76], we define the density of our system as:

$$n(x) = \frac{1}{2\pi i} \int_{C_\mu} G_E(x, \xi) dE \tag{B.1}$$

where C_μ is a contour in the complex energy plane containing all of the occupied states (an example of this contour is shown in Fig. 5.10). $G_E(x, \xi)$ is the Green's function using the following representation:

$$G_E(x, \xi) = \frac{\psi_L(x_<)\psi_R(x_>)}{W(\psi_R, \psi_L)} \tag{B.2}$$

where $x_< = min(x, \xi)$ and $x_> = max(x, \xi)$; $\psi_L(x)$ and $\psi_R(x)$ are solutions to the Schrödinger equation at energy E, satisfying the boundary conditions to the left and right, and $W(\psi_R, \psi_L)$ is the Wronskian of the two solutions.

To show this is true, we first define the Schrödinger equation,

$$\Big[-\frac{d^2}{dx^2} + v(x) \Big] \psi(x) = E\psi(x). \tag{B.3}$$

Our Green's function is then, $G_E(x, \xi) = (E - H)^{-1}_{x,\xi}$, with the property:

$$(E - H)_x G_E(x, \xi) = \delta(x - \xi). \tag{B.4}$$

In Eq. B.4, G must be continuous at $x = \xi$, thus we may write

$$G(x, \xi) = \begin{cases} A\psi_L(x)\psi_R(\xi) & x < \xi \\ A\psi_L(\xi)\psi_R(x) & x > \xi \end{cases} \tag{B.5}$$

or more compactly

$$G(x, \xi) = A\psi_L(x_<)\psi_R(x_>). \tag{B.6}$$

Using the same definitions of $\psi_{L(R)}(x)$ and $x_{<(>)}$ as in Eq. B.2. By integrating Eq. B.4 around ξ from $\xi - \epsilon$ to $\xi + \epsilon$ we find the jump condition,

$$G'(\xi - \epsilon, \xi) - G'(\xi + \epsilon, \xi) = 1. \tag{B.7}$$

With Eq. B.6 the condition becomes

$$A(\psi_R(\xi)\psi'_L(\xi) - \psi'_R(\xi)\psi_L(\xi)) = 1 \tag{B.8}$$

and we see that the constant A, is one over the Wronskian $W(\psi_R, \psi_L; \xi)$ and thus the Green's function takes the form of Eq. B.2. Using the eigenfunction expansion of the Green's function [84]

$$G_E(x, \xi) = \sum_n \frac{\psi_n(x)\psi_n^*(\xi)}{\varepsilon_n - E} \tag{B.9}$$

the residue of the Green's function at ε_k is

$$Res(G_E(x, \xi), \varepsilon_k) = \psi_k(x)\psi_k^*(\xi). \tag{B.10}$$

We then see that the density, $n(x) = \sum_{\epsilon_i \leq \mu} |\psi_i|^2$, can be written as:

$$n(x) = \sum_{k=1}^{n} Res(G_E, \varepsilon_k) \tag{B.11}$$

where k is over all occupied states with energy less than or equal to μ. The residue theorem for a positively oriented closed curve is

$$\frac{1}{2\pi i} \oint_C f(z)dz = \sum_k Res(f, a_k) \tag{B.12}$$

where $Res(f, a_k)$ is the residue of the function $f(z)$ at the point a_k and k extends over all points a_k which are enclosed inside the contour C_μ. Combining Eqs. B.12 & B.11 we arrive at Eq. B.1.

VITA

KELSIE NIFFENEGGER

EDUCATION

Purdue University West Lafayette, IN

Ph.D, Physics Expected December 2018

Thesis: Partition Density Functional Theory for Semi-Infinite and Periodic Systems

Auburn University Auburn, AL

B.S., Physics May 2012

Dean's Medalist in Physics, Sigma Pi Sigma Honors Society

EXPERIENCE

Purdue University West Lafayette, IN

Graduate Research Assistant May 2013 – Present

Advised by: Dr. Adam Wasserman

· Studied the electronic structure of metal-atom interfaces and periodic systems to expand the scope of Partition Density Functional Theory (P-DFT).

· Developed inversion codes to generate exact results of model systems towards constructing accurate approximations for P-DFT.

Advised by: Dr. Francis Robicheaux

· Constructed quantum mechanics simulations of rotating ion rings towards the study of space-time crystals.

Graduate Teaching Assistant May 2012 – August 2018

Multiple teaching and management roles for PHYS 172 Modern Mechanics, which is taken by over 2,500 students annually:

Lab Coordinator

· Led weekly training meetings and created instructional notes for 20–30 undergraduate and graduate teaching assistants per semester which standardized the in-class experience of students.

· Revised lab manuals, VPython codes, and experiments such that the presentation of the material is clear and straightforward.

· Utilized student and teaching assistant feedback to modify course content and structure.

Lecturer

· Taught complex concepts to classes of 20–120 students in an accessible and engaging manner through analogy, examples, and demonstrations.

Course Coordinator

· Oversaw integration of course components, organized online course material, and managed teaching assistants.

Lab Teaching Assistant

· Introduced and supervised lab activities, assessed student knowledge, debugged students' codes, and clarified physics concepts.

· Personally taught over 1,300 students with an average overall evaluation of 4.7/5.0.

Auburn University Auburn, AL

Undergraduate Research Assistant September 2009 – May 2012

Advised by: Dr. Francis Robicheaux

· Developed molecular dynamics simulations analyzing electron behavior in ultracold plasmas, Rydberg atoms, and during ionization of hydrogen atoms in strong magnetic fields.

· Taught numerical methods and C/C++ to new undergraduate researchers.

University of South Florida Tampa, FL

Undergraduate Research Assistant May 2011 – August 2011

Advised by: Dr. Vasily Zhakhovsky

· Simulated surface responses of gold films irradiated by femtosecond laser pulses using molecular dynamics and finite element analysis.

PUBLICATIONS

· F Robicheaux and K Niffenegger. Quantum simulations of a freely rotating ring of ultracold and identical bosonic ions. Physical Review A, 91(6):063618, 2015.

· K Niffenegger, PH Donnan, F Robicheaux. Microwave Effects Relevant to Antimatter Traps. Auburn University Journal of Undergraduate Scholarship, 2:42-47, 2013.

· PH Donnan, K Niffenegger, T Topcu, and F Robicheaux. Calculation of state selective field ionization of hydrogen atoms in a strong magnetic field. Journal of Physics B: Atomic, Molecular, and Optical Physics, 44(18):184003, 2011.

· K Niffenegger, KA Gilmore, and F Robicheaux. Early time properties of ultracold neutral plasmas. Journal of Physics B: Atomic, Molecular, and Optical Physics, 44(14):145701, 2011.

PRESENTATIONS

· Formation of Nanostructures at Gold Surfaces Exposed to Femtosecond Laser Pulses

  - Talk at the 2012 American Physical Society March Meeting

· Partition Theory for Semi-Infinite and Periodic Systems

  - Talk at the 2016 American Physical Society March Meeting
  - Poster at the 46th Midwest Theoretical Chemistry Conference

· Partition Density-Functional Theory for Semi-Infinite and Periodic Systems

  - Talk for the Purdue Physics Graduate Student Seminar Series, 2016.

· Fragment Density Functionals

  - Invited talk at Purdue University Department of Chemistry's weekly Physical Chemistry Seminar, 2018.

ORGANIZATIONS

Purdue University Department of Physics and Astronomy

Graduate Student Mentor

· Supplied first year graduate students with information about course choices, research advisers, and how to succeed in their transition to graduate school.

Purdue Physics Graduate Student Association

Teaching and Professional Development Officer, Member

· Acted as liaison between graduate students and the department head.

· Collected graduate student opinions through departmental surveys and advocated for their interests in regards to faculty teaching assignments, teaching assistant positions, and adviser accountability.

Purdue Women In Physics

Member

· Organize and/or participate in monthly lunch meetings between students, post-docs, and faculty in the department to learn about and discuss how to thrive as a woman in STEM.

Lafayette Regional Science and Engineering Fair

Judge

· Listen as 5th – 12th grade students explain their science fair projects to assess their overall performance. Engage with them by asking questions, offering critiques, and commending their accomplishments in order to nurture their enthusiasm for science.

Auburn University Society of Physics Students

President, Vice President

· Negotiated with the department head to get space and resources for undergraduate physics majors.

· Revitalized the chapter by organizing regular meetings, social events, and fundraisers.

· Identified opportunities for students to attend regional conferences and coordinated with the department to plan trip logistics.

HONORS AND AWARDS

Akeley-Mandler Award for Teaching Excellence 2017

Awarded by: Purdue University Department of Physics and Astronomy

Graduate Teaching Award 2015

Awarded by: Purdue University Teaching Academy

Outstanding Teaching Assistant 2014

Awarded by: American Association of Physics Teachers